

Towards *in silico* Organogenesis: A Data-based Computational Model for Limb Bud Patterning

A dissertation submitted to the
ETH Zurich

for the degree of
Doctor of Science

presented by

Philipp Daniel Germann

Master of Science in Physics, Universität Bern

born 6 May 1985

from Adelboden BE

accepted on recommendation of
Prof. Dr. D. Iber, examiner
Prof. Dr. R. Zeller, co-examiner
Prof. Dr. F. Naef, co-examiner

2014

Summary

Limb bud development served for decades as a model system for organogenesis, producing countless insights into molecular and cellular processes and inspiring important mathematical models. The main signaling components in the developing limb bud and their regulatory interactions have been defined, but an integrated understanding of this complex signaling network is still lacking.

We have developed a spatio-temporal computational model of the regulatory network that coordinates signaling between the apical ectodermal ridge (AER) and the zone of polarizing activity (ZPA) at a level of genetic detail that has not been reached before. The model is well constrained given the large amount of available data, and it reproduces all experiments that are relevant to the network. While constructed with static data, the model provides a dynamic view on the regulatory processes that govern limb bud development and allows us to explore the dynamic regulatory interactions that enable transient *Shh* expression. Further regulatory functionality emerges from these network interactions. Thus the desensitization to SHH that is also experimentally observed, is due to depletion of its transcription factor GLI3 in our model. Ectopic desensitization due to a SHH source leads to auto-regulation of SHH, that is also observed experimentally as down-regulation of *Shh* expression in the presence of a SHH bead. Following clues of the full model, we isolated structural properties in lower-dimensional calculations, that add further robustness towards SHH signaling. Finally, we apply our SHH-module to limb development in cattle to demonstrate that the lack of up-regulation of its receptor *Ptch1* within the mesenchyme is sufficient to explain the loss of asymmetry in other SHH-target genes.

The model is a further step towards *in silico* genetics of the limb and can now be used as a resource to study the underlying regulatory mechanisms and to highlight gaps in our understanding that need to be addressed in further experiments.

Zusammenfassung

Gliedmassenentwicklung hat während Jahrzehnten als Modellsystem für Organogenese unzählige Einblicke in molekulare und zelluläre Prozesse ermöglicht und wichtige mathematische Modelle inspiriert. Die wichtigsten Signal-Zentren in der sich entwickelnden Extremitätenknospe und die regulatorischen Interaktionen dazwischen wurden charakterisiert, aber ein integrales Verständnis dieses komplexen Signal-Netzwerks steht noch aus.

Wir haben ein räumliches und zeitliches, mathematisches Modell des regulatorischen Netzwerks, das die Signale zwischen der apikalen ektodermalen Randleiste (AER) und der Zone der polarisierenden Aktivität (ZPA) koordiniert, in einem bisher unerreichten genetischen Detailgrad entwickelt. Das Modell ist durch die vielen experimentellen Daten gut eingeschränkt und reproduziert alle für das Netzwerk relevanten Experimente. Obwohl mit statischen Daten konstruiert bietet das Modell eine dynamische Sicht der regulatorischen Prozesse, die Extremitätenknospenentwicklung orchestrieren und erlaubt uns die dynamischen regulatorischen Interaktionen, die transiente *Shh* Expression ermöglichen, zu untersuchen. Weitere regulatorische Funktionalitäten ergeben sich aus diesem Interaktionsnetzwerk. So rührt in unserem Modell die Desensibilisierung gegen SHH, die auch in Experimenten beobachtet wird, von dem Verbrauch des Transkriptionsfaktors GLI3 her. Ektopische Desensibilisierung durch eine SHH Quelle führt zur Selbstregulation von SHH, die experimentell als Verminderung von *Shh* Expression in der Gegenwart eines SHH getränkten Kügelchens beobachtet wird. Hinweisen aus dem kompletten Modell folgend isolieren wir in nieder-dimensionalen Berechnungen strukturelle Eigenschaften, die zusätzliche Robustheit gegen SHH Signalaktivität bieten. Schliesslich wenden wir unser SHH-Modul auf die Entwicklung von Kuhbeinen an und zeigen, dass die fehlende Hochregulation des Rezeptors *Ptch1* im Mesenchym ausreicht, um den beobachteten Verlust der Asymmetrie in anderen SHH-Ziel-Genen zu erklären.

Das Modell ist ein weiterer Schritt in Richtung *in silico* Genetik der Extremitäten und ist ein Mittel zum Studium der unterliegenden regulatorischen Mechanismen und um Lücken in unserem Wissen, die experimentell betrachtet werden müssen, hervor zu heben.

Contents

Foreword	6
I. Introduction	8
1. How do digits emerge? – Mathematical Models of Limb Development	9
1.1. Introduction	9
1.2. The French Flag Model	10
1.3. Turing Pattern	12
1.4. Data-based Mechanistic Models of Pattern Formation in the Limb	15
1.5. Long Bone Development	18
1.6. Conclusion	22
II. Methods	23
2. Simulating Organogenesis in COMSOL	24
2.1. Introduction: Mechanistic Models for Organogenesis	24
2.2. Advances: Optimizing COMSOL Models	26
2.3. Challenges: Large Deformations	28
2.4. Conclusions & Outlook: Studying Growth in 3D	29
III. Results	30
3. A Model for Anterior-Posterior Limb Bud Patterning	31
3.1. Introduction	31
3.2. Mathematical Framework	33
3.3. Mutual Inducing Interactions Between AER-FGFs and BMPs Initiate the Limb Bud Signalling Network	35
3.4. SHH Dynamics	41
3.5. The Regulation of <i>Grem1</i>	46
3.6. Mathematical Formulation	50
4. Self-regulated Dynamics Emerge from the Core Regulatory Network	58
4.1. Spatio-temporal Dynamics of the Regulatory Interactions in the Develop- ing Limb Bud	58

4.2. Dynamics of <i>Shh</i> Expression Emerge From the Network Interactions . . .	60
4.3. The Gremlin Gap Terminates the Production of Shh	62
5. Robustness to SHH Signaling	64
5.1. Depletion of Full-length GLI3 Provides a Mechanism for Desensitization to SHH	64
5.2. The Auto-inhibition of <i>Shh</i> Results from Desensitization	65
5.3. Robustness to <i>Shh</i> Expression Levels	66
6. The Bovine Limb Buds Response to SHH	69
6.1. Bovine Limb Development	69
6.2. Modeling the Bovine SHH-Pathway	70
6.3. Discussion	74
IV. Discussion	76
7. Conclusions	77
7.1. Achievements and Predictions	77
7.2. Open Questions and Outlook	80
7.3. Perspective: towards <i>in silico</i> genetics	82
7.4. Conclusion	83
Acknowledgments	84
Bibliography	85
Curriculum Vitae	107

Foreword

Shortly after the fertilized egg turned into an elongated embryo, four limb buds start bulging out of its flanks. These flattened sacs of ectoderm filled with undifferentiated mesenchymal cells elongate until they are roughly as long as their width. Then the distal part enlarges, giving rise to the hand plate. Around these stages the genetic pattern is laid down and some cells start to condensate and differentiate into structures which will give rise to bones. Then the cells in between the digits undergo apoptosis and further elongation is driven by the directional growth of long bones.

The limb has a long and fruitful history as model system for organogenesis. As limb buds grow outside of the embryo they can be micro-surgically manipulated. In such experiments the specialized ectoderm over the distal limb bud (Saunders, 1948) – termed the apical ectodermal ridge (AER) – and the mesenchyme from the posterior margin (Saunders and Gasseling, 1968) – termed the zone of polarizing activity (ZPA) – were identified as main signaling centers essential for growth, number and identity of the skeletal elements within the limb. Subsequent experiments demonstrated that these two signaling centers are not independent (Todt and Fallon, 1987). With the advent of cloning fibroblast growth factors (FGFs) were identified as the morphogens secreted by the AER (Niswander et al., 1993) and Sonic hedgehog (SHH) as the morphogen secreted by the ZPA (Riddle et al., 1993).

That limbs are not essential for survival then facilitated genetic experiments (mainly performed in mice) that untangled the regulation underlying the interaction of the limb organizers. Bone morphogenic proteins (BMPs) induced by FGF were identified as a connection between the AER and the ZPA (Pizette and Niswander, 1999), modulated by the BMP-antagonist GREMLIN1 (Khokha et al., 2003), which in turn is regulated by BMP-, FGF- and SHH-signaling (Verheyden and Sun, 2008; Bastida et al., 2009; Bénazet et al., 2009). That these involved morphogens are important throughout development and are connected to disease (Wakefield and Hill, 2013; Turner and Grose, 2010; Jiang and Hui, 2008) kept the field prosperous. Regeneration in salamander (Guimond et al., 2010; Satoh and Makanae, 2014) and fish (Nachtrab et al., 2013) add to the medical interest. Recently, the limb gained additional attention as a model system for evolutionary development as genetic studies in more species are becoming possible (Dahn et al., 2007; Hockman et al., 2008; Cretekos et al., 2008; Cooper et al., 2013; Woltering et al., 2014).

Based on this vast literature (Zeller et al., 2009) we believe that the limb is also a suitable model system for *in silico* genetics, that permit the simulation of perturbations at the edge and beyond the reach of conventional genetics (Iber and Zeller, 2012). As a next step in this endeavor, we present in this thesis the construction of a computational model for this feedback-loop between the AER and the ZPA, at a level of detail that has not been reached before, and analyze the underlying dynamics and emerging behaviors.

In chapter 1 we introduce the question of how digits emerge and broadly review computational models of limb patterning and long bone formation. Then, in chapter 2, we motivate our mechanistic approach based on coupled reaction-diffusion equations and provide technical details on our implementation in the COMSOL Multiphysics finite element software package. In chapter 3 we construct the core regulatory network by extensively reviewing experiments, implementing these findings in our framework and demonstrating how the resulting model reproduces the data. In the remainder of this thesis we then analyze the underlying mechanisms. Thus, in chapter 4 we show how the self-regulation of *Shh* expression arises and explore the role of GREM1 in this context; in chapter 5 we show how the emerging desensitization to SHH leads to auto-regulation of *Shh* and robustness to SHH; and in chapter 6 we apply our SHH-module to bovine limb bud development. Finally, we conclude in chapter 7 with an outlook and a discussion of the contributions of this thesis.

Part I.

Introduction

1. How do digits emerge? – Mathematical Models of Limb Development

This chapter is adapted from **Iber, D. and Germann, P.** (2014). How do digits emerge? – Mathematical Models of Limb Development. *Birth Defects Research. Part C, Embryo Today: Reviews* **102**, 1-12. ISSN 1542-9768.

Abstract

The mechanism that controls digit formation has long intrigued developmental and theoretical biologists, and many different models and mechanisms have been proposed. Here we review models of limb development with a specific focus on digit and long bone formation. Decades of experiments have revealed the basic signaling circuits that control limb development, and recent advances in imaging and molecular technologies provide us with unprecedented spatial detail and a broader view on the regulatory networks. Computational approaches are important to integrate the available information into a consistent framework that will allow us to achieve a deeper level of understanding and that will help with the future planning and interpretation of complex experiments, paving the way to *in silico* genetics. Previous models of development had to be focused on very few, simple regulatory interactions. Algorithmic developments and increasing computing power now enable the generation and validation of increasingly realistic models that can be used to test old theories and uncover new mechanisms.

1.1. Introduction

Limb development has long served as a model system for organogenesis before methods became available that facilitated the analysis of the development of vital organs (Zeller et al., 2009). As a result, an unmatched level of molecular detail has been defined, which makes the limb a well-suited system to develop detailed mathematical modeling approaches (Iber and Zeller, 2012). The first computational models of limb development were concerned with the growth of the limb bud and suggested that growth had to be anisotropic to yield the observed embryonic limb shapes (Ede and Law, 1969). Recent 3D imaging of the limb in combination with an earlier Navier-Stokes based growth model (Dillon and Othmer, 1999) indeed supports the notion of anisotropic growth in the limb (Boehm et al., 2010).

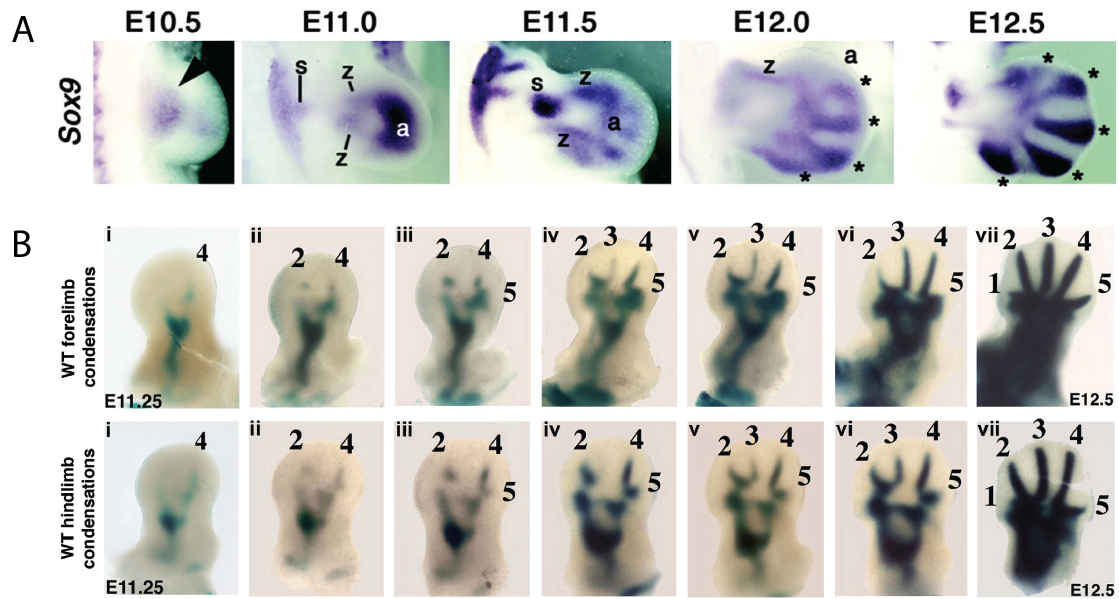


Figure 1.1.: Digit Emergence during Limb Development. (A) Nascent digit condensations become first visible around embryonic day (E) 11.5 and express *Sox9* (Kawakami et al., 2005). (B) The digits appear neither simultaneously nor in strict posterior to anterior sequence (or vice-versa) (Zhu et al., 2008).

Most modeling attention has focused on the emergence of digits during limb development (Maini and Solursh, 1991). Nascent digit condensations become first visible around embryonic day (E) 11.5 and express *Sox9* (figure 1.1A, Kawakami et al., 2005). Interestingly, the digits appear neither simultaneously nor in a strict posterior to anterior sequence (or vice-versa) (figure 1.1B; Zhu et al., 2008). The mechanism that controls digit formation has long intrigued developmental and theoretical biologists, and in this review we will focus on proposed mechanisms and models, starting with the earliest approaches (French Flag model and Turing mechanism) and extending it to more recent approaches that take the detailed regulatory interactions and the physiological, growing limb bud geometry in the developing limb bud into account. Finally, we discuss models for the formation of long bones, once the digit condensations have been defined.

1.2. The French Flag Model

Grafting experiments in chicken embryos showed that a small piece of tissue from the posterior part of the limb bud, the so-called zone of polarizing activity (ZPA), would induce a second, mirror-symmetric set of digits when grafted to the anterior side of a recipient limb bud (Saunders and Gasseling, 1968), as reviewed in (Tabin, 1991). Wolpert proposed that the ZPA was the source of a diffusible morphogen, and that a diffusion-based gradient along the anterior-posterior (AP) limb axis would induce the different

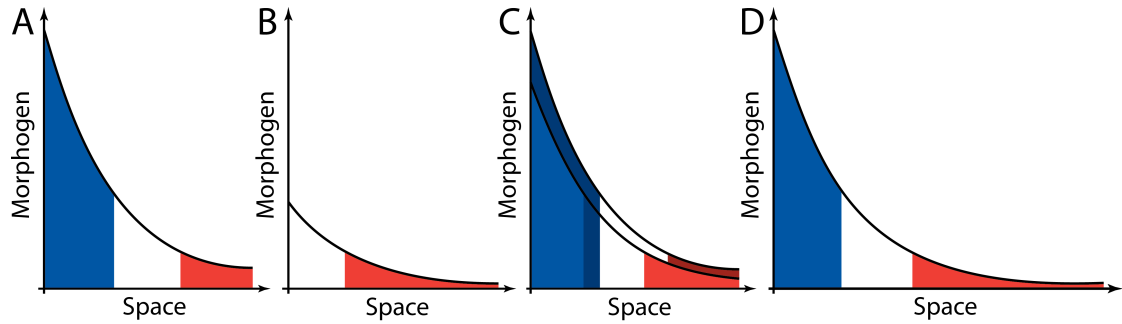


Figure 1.2.: The French Flag Model. (A) A threshold-based differentiation mechanism. A morphogen diffuses from the left into the domain, and the cells differentiate according to two fixed thresholds into three cell types, illustrated by the colours of the French flag. (B) A lower morphogen concentration would result in less digits (or digit types) in the French Flag model as the high threshold concentration would not be breached. (C) The impact of changes in the morphogen source. Already very small changes in the morphogen source would shift the differentiation fronts. (D) The impact of domain size. The limb buds of different species differ in size, and the pattern would not scale relative to the size of the limb domain if based on a simple French Flag mechanism, i.e. blue and white regions are of normal size, while the red region is extended.

digit identities (Wolpert, 1969). According to this so-called French Flag model cells would respond differently above and below certain concentration thresholds along the gradient (figure 1.2A; Wolpert, 1969). The French flag model was supported by further experiments that showed that smaller grafts (producing presumably less morphogen) induced only partial duplications (Tickle, 1981; figure 1.2B). About 25 years later the proposed morphogen-type signal was identified as Sonic Hedgehog (SHH) (Riddle et al., 1993). In fact, genetic and molecular analysis established that SHH fulfilled several of the criteria of a true morphogen. Thus inactivation caused the loss of all, but the most anterior digit (thumb) (Chiang et al., 1996; Kraus et al., 2001), and the forced expression of *Shh* in fibroblasts converted these into cells with polarizing activity such that their implantation into the anterior limb bud induced formation of a second, mirror-symmetric set of digits in a concentration-dependent fashion (Riddle et al., 1993; Yang et al., 1997).

Later experiments showed that it was important to distinguish between mechanisms that would induce the emergence of digits and those that would specify the digit type. Mouse limb buds lacking both *Shh* and the downstream mediator *Gli3* have a polydactylous phenotype with up to ten digits (Litingtung et al., 2002; te Welscher et al., 2002b), such that SHH signaling is clearly not necessary for digits to emerge. The digits, however, all looked the same, such that SHH appears to be necessary to specify the digit type. Furthermore, digits appear neither simultaneously nor in strict posterior to anterior sequence (or vice-versa) (figure 1.1B; Zhu et al., 2008). Thus, the formation of digits cannot be explained by a simple spatial SHH morphogen concentration gradient acting across the limb field. As regards to digit specification, there is evidence that long-range

SHH signaling contributes to patterning of the middle and anterior digits 3 and 2, but specification of the most posterior digits 4 and 5 has been suggested to depend on the length of exposure of progenitors to SHH signaling (Harfe et al., 2004).

However, there are also limitations to a simple SHH-based model for digit specification, including the robustness of the process. The expression of *Shh* has been shown to fluctuate during limb bud development (Amano et al., 2009), and neither removal of one copy of *Shh* (Chiang et al., 1996; Bénazet et al., 2009), nor posterior implants of *Shh* expressing cells alter the digit pattern (Riddle et al., 1993). Theoretical considerations suggest that for a single morphogen-threshold-based mechanism even small changes in concentrations at the source would shift the position at which the pattern would emerge (figure 1.2C; Lander et al., 2009). In addition to noise at the source, there will also be variation in ligand transport, degradation, and receptor binding (Bollenbach et al., 2008). While spatial and temporal averaging of ligand concentrations can enhance the precision of a morphogen read-out (Gregor et al., 2007), and feedbacks may exist to buffer changes in the SHH concentration, a more sophisticated regulatory network must be invoked to explain robust pattern formation in the limb. In fact, experiments show that while the expression of *Shh* is reduced to 65-70% of its normal value, the expression of SHH- and BMP-dependent genes (*Gli1* and *Msx2* respectively) is normal in *Shh* heterozygous mice (Bénazet et al., 2009).

There is the added problem of size. Chicken limb buds are significantly larger than mouse limb buds at early stages, but the patterning mechanisms appear overall highly conserved between species, as also demonstrated by cross-species grafts (Tickle et al., 1976; Tabin, 1991). As illustrated in figure 1.2D, any pattern arising due to threshold values set by a simple linear or exponential diffusion gradient would not scale with the size of the domain. In particular, the blue and white stripes of the French flag in the larger domain would be equal to the ones of the smaller domain, while the red stripe would expand (i.e no scaling). The problem was previously recognized for the Bicoid gradient in differently sized *Drosophila* embryos (Gregor et al., 2007), as well as in many other developmental systems (Ben-Zvi et al., 2008; Umulis et al., 2010). While several mechanisms have been proposed to deal with the problem of correct scaling (Ben-Zvi et al., 2008; Umulis et al., 2010; Ben-Zvi et al., 2011; Lauschke et al., 2013), these have remained controversial or would not apply to the limb.

1.3. Turing Pattern

In his seminal essay in 1952, long before the sequence and structure of the underlying gene products became known, Turing proposed that "chemical substances, called morphogens, reacting together and diffusing through a tissue, are adequate to account for the main phenomena of morphogenesis" (Turing, 1952). Alan Turing showed that two components, which diffuse at different speeds and regulate each other in a specific manner, can give rise to a wide range of different patterns. The details of Turing's theory have fascinated generations of biologists and they have repeatedly been reviewed (Kondo and Miura, 2011); Murray's classical textbook on Mathematical Biology gives details on the

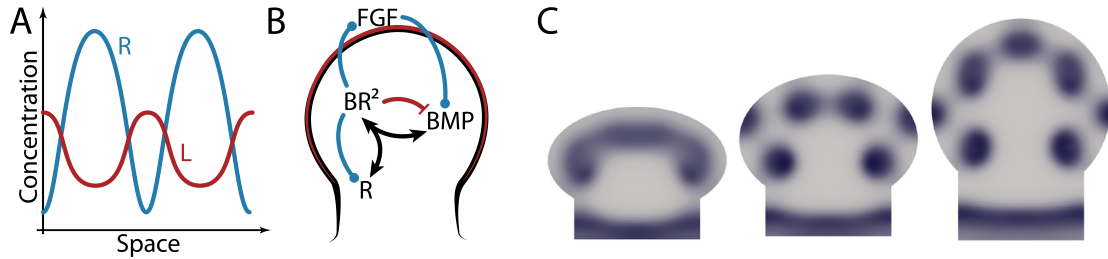


Figure 1.3.: Turing Pattern as a Mechanism for Digit Patterning. (A) Interactions between receptors (R) and ligand (L) can give rise to Schnakenberg kinetics that result in Turing patterns. To result in Turing patterns, ligands need to diffuse faster than receptors, receptors and ligands need to bind cooperatively, and receptor-ligand binding must up-regulate the receptor density on the membrane. An important property of Turing patterns is their dependency on domain size. If the size of the patterning domain is sufficiently increased or decreased further patterns appear or disappear respectively. (B, C) Digit patterning in a ligand-receptor based Turing model based on BMP, BMP receptor, that is modulated by AER-FGFs. (B) The regulatory network proposed in Badugu et al., 2012. AER-FGFs are produced in the AER, marked in red, and regulate BMP expression in the AER and mesenchyme. The dimer BMP, B, and its receptor, R, form a complex composed of one BMP dimer and two receptors, BR₂. (C) The BMP-receptor, BR₂, first forms the characteristic donut shape that then breaks into digit condensations as the limb bud is growing out; simulations were carried out on a domain that grows at the measured speed.

mathematical aspects (Murray, 2003). The Turing mechanism is based on a diffusion-driven instability and is sufficiently flexible to reproduce virtually any pattern as long as the reactions and parameters are appropriately adjusted (Murray, 2003; Kondo and Miura, 2011). An important property of the so-called Turing patterns is their dependency on domain size. If the size of the patterning domain is sufficiently increased or decreased further patterns appear or disappear respectively (figure 1.3A). A biological example where such size dependency is observed is the marine angelfish *Pomacanthus* (Kondo and Asai, 1995). The coat of baby fish has few stripes, but more stripes form as the fish grow.

The Turing model was first applied to limb digit patterning in 1979 (Newman and Frisch, 1979), and many aspects of bone patterning in the limb have since been shown to be explicable with a Turing mechanism (Newman and Bhat, 2007). In particular, given their flexibility, Turing models could be shown to reproduce the wide range of different digit patterns on the various limb geometries of different species (Zhu et al., 2010). Miura and colleagues further showed that the supernumerary digits in the Doublefoot mutant mice (Crick et al., 2003) could be explained with the size dependency of Turing patterns (Miura et al., 2006). Newman and colleagues also showed that the different number of condensations in stylopod, zeugopod, and autopod in anterior-posterior direction could, in principle, result from the lengthening of the limb bud in proximal-distal direction; this

effect requires the early fixation of proximal elements (Hentschel et al., 2004).

An increasing body of experimental results supports a Turing mechanism in the limb (Sheth et al., 2012). However, the molecular components of the Turing mechanism have remained elusive. Regulatory reactions, that would give rise to Turing patterns, were first defined twenty years after the first publication of the Turing mechanism (Gierer and Meinhardt, 1972). These included an activator-inhibitor mechanism and a so-called substrate-depletion mechanism. The activator-inhibitor mechanism has been frequently applied to reproduce patterns in biology because it provided an attractive regulatory framework that could be implemented by many negative feedback interactions in biological systems. One example is provided by the WNT-DKK negative feedback, which has been proposed to control hair follicle spacing (Sick et al., 2006). For the limb, a number of different negative feedbacks have been proposed, mainly based on TGF- β signaling and either fibronectin deposition in the extracellular matrix (ECM) or TGF- β antagonists (Zhu et al., 2010). However, to date there is no genetic evidence in support of any of these proposed Turing components. It has also been noted, that, the interaction with the ECM can result in self-emerging patterning. Thus by secreting enzymes, cells can digest the ECM and consecutively move closer. Such a traction-based mechanism then allows self-organized patterning (Oster et al., 1985). Similar to classical Turing pattern, haptotaxis can drive instabilities that can lead to the emergence of aggregation patterns, even in the absence of cell motility, i.e. without random movements of cells (Oster et al., 1983).

Part of the difficulty in proposing molecular components for Turing mechanisms is that one of the components (here the antagonist) has to diffuse much faster than the other (here the activator), which is difficult when both forms are diffusing. Transient differences in diffusion speeds as may result from differential interactions with the extracellular matrix have recently been suggested to result in Turing patterns (Muller et al., 2012). It will have to be seen whether such transient differences are indeed sufficient to give rise to robust symmetry breaks and patterning in biology. We have recently shown that different diffusion speeds as well as the other Turing conditions can easily be obtained with ligand-receptor pairs (Badugu et al., 2012; Cellière et al., 2012; Menshykau et al., 2012; Menshykau and Iber, 2013). Thus if ligands and receptors interact cooperatively and trigger the emergence of more receptor on the membrane (by enhancing expression or by enhancing receptor recycling to the membrane), these pairs give rise to Schnakenberg Turing kinetics (Schnakenberg, 1979), which are well known to give rise to Turing patterns (Gierer and Meinhardt, 1972). This opens up the possibility that Turing patterns result from a single morphogen. We further showed that a model based on the BMP-receptor interaction would reproduce the digit patterning that is observed in wildtype and various mutants, both on static and growing domains, if we combined it with FGF signaling from the apical ectodermal ridge (figure 1.3B, C; Badugu et al., 2012). Interestingly, in *Smad4* mutants, *Sox9* is expressed in its characteristic horseshoe pattern in the autopod, but does not break up into digit condensations (Bénazet et al., 2012). SMAD4 is a CO-SMAD and thus a key transducer of canonical BMP signals.

In spite of the great similarity of simulated and real patterns, it remains to be established whether Turing-type mechanisms rather than alternative mechanisms underlie

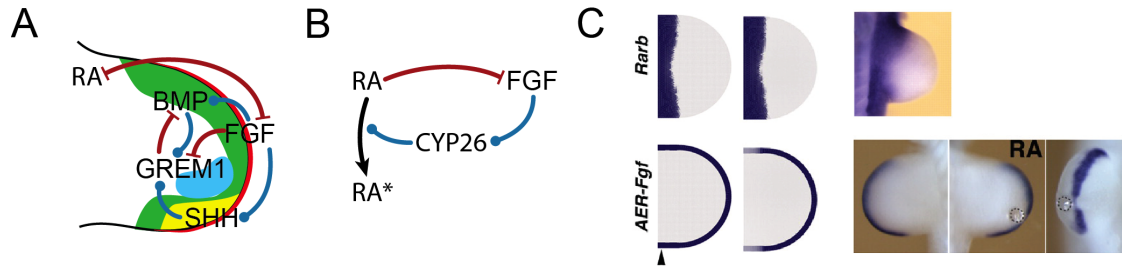


Figure 1.4.: Data-based Models of Pattern Formation in the Limb. (A) The regulatory network including the most important molecular players, i.e. RA, BMP (expressed in the green domain), FGF secreted from the AER (red line), SHH secreted from the ZPA (yellow) and GREM1 (expression domain marked in purple). (B) The regulatory sub-network that controls the PD axis. AER-FGFs induce expression of the enzyme *Cyp26b1*, which promotes the turn-over of RA. RA, in turns, represses expression of AER-Fgfs. (C) Patterning the PD axis. Simulation of the RA-AER-FGF network with (1st column) and without (2nd column) the negative regulation of AER-Fgf expression by RA (red arrow in panel B). Both simulations reproduce the observed restriction of *Rarb* expression (1st row) to the proximal side of the limb bud (3rd column). However, only in case of the negative impact of RA on AER-FGF (2nd column) can the distal restriction AER-Fgf expression be reproduced (2nd row). As predicted by the model, RA-loaded beads indeed down-regulate AER-Fgf expression (3rd column) (Probst et al., 2011).

their establishment (Hofer and Maini, 1996). In fact, in several cases, Turing-type mechanisms have been wrongly assigned to patterning processes such as e.g. the mechanism by which the stripy expression pattern of pair-rule genes emerge during *Drosophila* development (Akam, 1989). These failures reveal the importance of a careful and comprehensive analysis of the underlying molecular interactions before proposing a Turing mechanism.

1.4. Data-based Mechanistic Models of Pattern Formation in the Limb

Experimental and genetic manipulation of vertebrate limb bud development over the last two decades has identified likely most key players controlling its growth and patterning, and has resulted in the definition of the core-regulatory network (figure 1.4A). The regulatory network in the limb is complex and is further complicated by the spatially and temporally restricted expression of many of the components. To define the mechanism of digit patterning, it will be important to test and improve proposed mechanisms in a computational framework that is consistent with all solidly established experimental data.

Previous efforts to organize the vast knowledge about regulatory interactions in the limb typically resulted in a modular view, i.e. in the focus on small sub-networks. The sub-networks in the various publications of different mutant phenotypes are not always

consistent with each other. An integrated analysis is possible only with the help of computational methods. Such more complex models are still best built by starting with a simple module that is then extended to include further factors that replace phenomenological descriptions in the model. In each step it is important to validate the model carefully with experimental data.

One way to organize the regulatory network into modules is to consider the control of the different axes separately and to only link these in a later step. Mouse forelimbs grow out from the flank and become visible around embryonic day (E) 9.25. As the limb bud grows and develops, asymmetries emerge along the proximal-distal (shoulder to fingertips), anterior-posterior (thumb to pinky), and dorso-ventral axes. The axes appear to be set up at different times and by different mechanisms. The proximal-distal (PD) axis develops as the limb bud expands distally as a result of the interaction between the apical ectodermal ridge (AER) and the underlying mesenchyme. The asymmetry in the anterior-posterior (AP) direction, on the other hand, is present already in the lateral plate mesenchyme as shown by graft experiments (Tabin, 1991). The dorso-ventral (DV) axis is established later and is defined by the ectoderm (MacCabe et al., 1974).

Limb bud outgrowth from the flank is initiated by a regulatory network of retinoic acid (RA), WNTs, and Fibroblastic Growth Factors (FGFs). Prior to limb initiation, *Fgf10* is expressed in a wide region in the trunk without any specific restriction to the presumptive limb areas. Around E8, RA induces the expression of *Wnt-2b* (Mercader et al., 2006), and WNT2B subsequently restricts the expression of *Fgf10* to the presumptive forelimb region; WNT8C plays a similar role for the hindlimb region (Kawakami et al., 2001). The inductive activities of both WNT2B and WNT8C are mediated by beta-catenin. Once limb initiation is underway, and after *Fgf10* expression has been restricted, FGF10 signals to the overlying ectoderm to induce expression of *Wnt-3a*, which eventually will become restricted to the AER. WNT3A then signals through beta-catenin to activate *Fgf8* expression. To complete the loop, FGF8 signals back to the mesenchyme of the nascent limb bud, where it contributes to maintain expression of *Fgf10*.

FGF8, together with the other FGFs that are expressed in the AER, control the distal part of the limb bud, while retinoic acid (RA) controls the proximal part of the limb bud (figure 1.4B; Mercader et al., 2000; Cooper et al., 2011; Roselló-Díez et al., 2011). What leads to the separation of the two signaling centers? Genetic analysis in the mouse showed that FGF8 reduces the RA concentration by enhancing the expression of the RA metabolizing enzyme *Cyp26b1* in the distal mesenchyme (Probst et al., 2011). Mathematical simulations predicted that RA would in turn limit AER-FGF activity. Experimental analysis indeed confirmed that ectopic RA activity restricts *Fgf4* and to a lesser extent *Fgf8* expression in the AER (figure 1.4C; Probst et al., 2011). This revealed a mutually antagonistic interaction of RA with AER-FGFs. In line with this, earlier experiments had shown that low doses of an RA implant increase the length of the AER, while higher doses decrease the length of the ridge (Tickle et al., 1982; Summerbell, 1983). On the other hand, it has been noted that there is no proximal expansion in AER-*Fgf8* expression in conditional mutants of an RA producing enzyme (Cunningham et al., 2011). However, the same group also showed that RA is necessary for the initiation of forelimbs as otherwise ectopic *Fgf8* expression prevents forelimb initiation

(Zhao et al., 2009; Cunningham et al., 2013). In the model, the antagonism between RA and FGF8 would be present already at the time of initiation, and the extension of the *Fgf8* domain could later well be maintained by RA-independent mechanisms. *Fgf8* expression is initiated upon limb but outgrowth in spite of the inhibitory role of RA, and the simulations predict that receptor binding limits diffusion of RA from the flank initially, once RA signaling enhances the expression of RA receptors, as indeed observed in experiments (Noji et al., 1991; Tabin, 1991). According to the model, receptor saturation eventually permits RA to diffuse further distally and to form a gradient that could regulate aspects of proximal-distal limb bud development (figure 1.4C) and that could define the proximal part (stylopod \rightarrow humerus) of the proximal-distal axis as suggested by two recent studies (Cooper et al., 2011; Roselló-Díez et al., 2011) and challenged by the Duester group (Zhao et al., 2009; Cunningham et al., 2013).

AER-FGFs initiate and maintain *Shh* expression, a key regulator of patterning along the anterior-posterior (AP) axis. SHH, in turn, enhances AER-*Fgf* expression via its impact on the expression of *Gremlin-1* (*Grem1*), an antagonist of BMPs (Bénazet and Zeller, 2009; Probst et al., 2011). The inclusion of such a simple positive feedback between AER-FGF and SHH in the mathematical model for the RA-AER-FGF interaction allowed us to reproduce the impact of a *Shh* knock-out on the patterning of the proximal-distal axis (Probst et al., 2011). The feedback between AER-FGFs and SHH thus integrates the development of the PD axis with that of the AP axis.

For a long time, it was unclear how *Shh* expression could be triggered by AER-FGFs in spite of a high BMP concentration, which has been shown to suppress *Shh* expression also in the presence of a high FGF concentration (Bastida et al., 2009). The conundrum was resolved by a combination of mathematical modelling and experimentation, which revealed that the BMP-dependent up-regulation of the BMP antagonist *Grem1* occurs fast (2h) (Bénazet et al., 2009). The resulting reduction in BMP activity enables up-regulation of *Shh* expression via AER-FGF signaling, which in turn enhances *Grem1* expression further. This robust and self-regulatory feedback signaling system propagates limb bud outgrowth distally and coordinates AP and PD limb bud axes development.

The initial simulation of the regulatory network of AER-FGF, SHH, BMP and GREM1 were only carried out over developmental time, but not on the spatial domain of the limb bud, and thus did not take the spatial differences along the different axes into account Bénazet et al., 2009. The inclusion of the spatial domain is, however, important because it permits us to further test the consistency of proposed regulatory networks (figure 1.4A, B) by comparing the spatio-temporal expression profiles of the network components to data from wild-type and mutant mice (figure 1.4C). Such image-based comparisons can also be used to determine suitable parameter values for the model (Menshykau et al., 2013). Simulating such a rather complex network not only over time, but also over space on realistic 2D or 3D growing or static limb bud domains is numerically challenging, but feasible (Germann et al., 2011; Badugu et al., 2012; Menshykau and Iber, 2012; Iber et al., 2013). In developing the computational model, a number of inconsistencies in the verbal model are typically detected and resolved. Gaps in the understanding are highlighted that can be addressed in further experiments. A validated model finally allows the investigation of questions that are difficult to address by experiments alone. This

concerns, in particular, functionalities that emerge indirectly from multiple regulatory interactions.

Going forward, the signaling models should be solved on realistic, growing domains to reveal how the self-organized regulation of the interaction network results in the emergence of digit condensations during limb bud outgrowth. Based on our previous model, the core network controlling the emergence of digit condensations comprises AER-FGFs and BMP (figure 1.3B; Badugu et al., 2012), with SHH gradients from the ZPA likely determining digit identity. The BMP-receptor interaction can result in Turing pattern that mark the digit condensations, and AER-FGFs are necessary to move the Turing spots away from the boundary into the limb domain and to modulate the Turing patterns to obtain the correct wildtype and mutant digit patterns in the model (Badugu et al., 2012).

1.5. Long Bone Development

To form digits, the digit condensations need to develop into the distinct long bones of the phalanges, separated by joints. The appearance of joints depends on the BMP antagonist NOGGIN, but long bones (without joints) still form in the absence of *Noggin* (Brunet et al., 1998). The first step in the formation of long bones is the formation of cartilage. The *Sox9*-expressing mesenchymal cells aggregate in mesenchymal condensations and subsequently develop into long bones by endochondral ossification (figure 1.5A; Kronenberg, 2003; Provot and Schipani, 2005; Wuelling and Vortkamp, 2011). As part of the process the digit condensations develop a highly organized spatial structure, the growth plate. In the developing growth plate, periarticular chondrocytes proliferate, differentiate into columnar chondrocytes, and then further differentiate into postmitotic hypertrophic chondrocytes (figure 1.5A). Growth is a consequence of both proliferation and differentiation into larger hypertrophic cells. The volume increase upon differentiation into hypertrophic chondrocytes happens in three phases (Cooper et al., 2013). The first phase is characterized by true hypertrophy, i.e. a proportionate increase in dry mass production and fluid uptake. The enlargement in the second phase is the result of cell swelling and the dramatic dilution of cell dry mass. In the final third phase, cells increase in size by increasing both dry mass and fluid volume proportionally. Cell differentiation into hypertrophic chondrocytes, and at later stages apoptosis of hypertrophic chondrocytes and replacement by invading osteoblasts all start in the centre of the domain (Wuelling and Vortkamp, 2010, 2011). Accordingly, hypertrophic chondrocytes (and later osteoblasts) accumulate at the centre of the domain, while proliferating (and resting) chondrocytes are found at the ends of the bone domain.

The study of mouse mutants has led to the identification of the core signaling proteins that control the growth and differentiation pattern during bone development by endochondral ossification (figure 1.5B). A key signaling factor is Parathyroid hormone-related protein (PTHrP) (Lanske et al., 1996; Vortkamp et al., 1996). PTHrP increases the pool of mitotically active chondrocytes by preventing their differentiation into hypertrophic chondrocytes (Karaplis et al., 1994; Weir et al., 1996), but, unlike Hedgehog

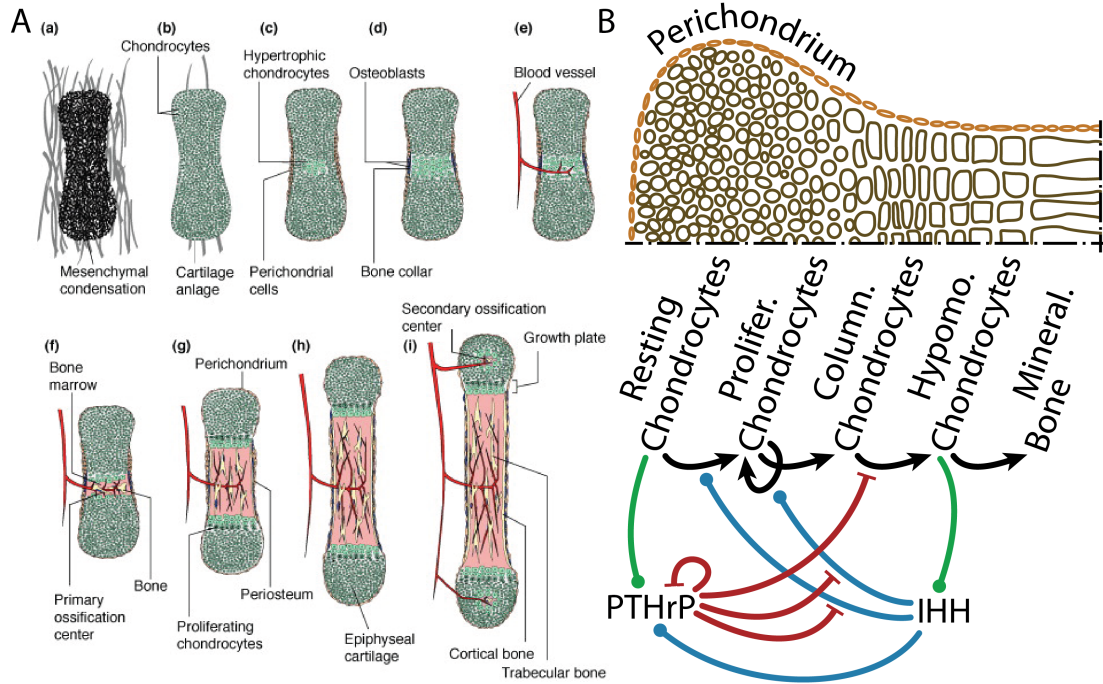


Figure 1.5.: The control of Long Bone Formation. (A) Endochondral bone development from mesenchymal condensation stage to formation of mature growth plate. (a, b) Chondrocytes differentiate within mesenchymal condensations to form cartilage anlagen of future bones. (c, d) Coincident with the appearance of the perichondrial bone collar, chondrocytes in the central anlage hypertrophy followed by invasion of vascular and osteoblastic cells from the collar (e) and formation of the primary ossification center (f). This process expands toward the ends of the bone, eventually forming mature growth plates (h). Secondary ossification centers later form in the epiphyseal cartilage (i). With permission, from Horton and Degnin, 2009. (B) A cartoon of the cell types, the differentiation paths, and the regulatory network controlling long bone formation by endochondral ossification. For details see text.

signaling, PTHrP does not enhance their proliferation rate (Karp et al., 2000). *Pthrp* is expressed and secreted by resting periarticular chondrocytes that reside at the ends of the domain (Karp et al., 2000), where differentiation is therefore blocked; hypertrophic chondrocytes thus emerge only at the centre of the domain. PTH/PTHrP-R signaling down-regulates the expression of its own receptor, *Pth/Pthrp-r* (Kawane et al., 2003). *Pth/Pthrp* receptor (*Pth/Pthrp-r*) is therefore expressed in maturing chondrocytes and in the perichondrium/periosteum, i.e. in a zone adjacent to the post-mitotic prehypertrophic chondrocytes (St-Jacques et al., 1999; Hilton et al., 2005).

A second important regulator of endochondral ossification is Indian Hedgehog (IHH) (Vortkamp et al., 1996; Kobayashi et al., 2005). IHH signaling via its receptor PTCH1 induces the expression of *Pthrp* (Vortkamp et al., 1996; St-Jacques et al., 1999; Karp

et al., 2000; Hilton et al., 2005; Kobayashi et al., 2005), as well as the expression of its own receptor, *Ptch1* (St-Jacques et al., 1999), and stimulates proliferation of chondrocytes (figure 1.5B; Karp et al., 2000). *Ptch1* is expressed most strongly in a zone adjacent to the post-mitotic pre-hypertrophic chondrocytes where also *Pth/Pthrp-r* is expressed (Hilton et al., 2005). In the *Ihh* null mouse no expression of *Ptch1* and *Pthrp* is observed in the developing bone, *Pth/Pthrp-r* is misexpressed, the chondrocyte proliferation rate is lower, and only very few hypertrophic chondrocytes emerge in the center of the domain (St-Jacques et al., 1999). IHH signals also independently of PTHrP. Thus IHH acts on periarticular chondrocytes to stimulate their differentiation, thereby regulating the columnar cell mass (Kobayashi et al., 2005), and further promotes chondrocyte hypertrophy (Mak et al., 2008). PTH/PTHrP-R signaling down-regulates the action of IHH (Kobayashi et al., 2005). High levels of *Ihh* mRNA are detected in cartilage from as early as E11.5 (Bitgood and McMahon, 1995). Expression is highest in chondrocytes in the growth regions of developing bones, but a lower level of expression persists into the hypertrophic zone (Bitgood and McMahon, 1995). On maturation, expression becomes progressively restricted to post-mitotic pre-hypertrophic chondrocytes adjacent to the *Pth/Pthrp-r*-expressing proliferative zones (Bitgood and McMahon, 1995; Vortkamp et al., 1996).

While the core regulatory network, comprising PTHrP, IHH, and its receptor PTCH1, has been defined, it has remained unclear how the patterns and the spatio-temporal control of the process emerge from these interactions. A number of mathematical models have been developed to explain the distribution of the signaling proteins IHH and PTHrP and their impact on bone growth and development (Brouwers et al., 2006; van Donkelaar and Huiskes, 2007; Isaksson et al., 2008; Garzon-Alvarado et al., 2009; Bougherara et al., 2010; Garzon-Alvarado et al., 2010). Garzon-Alvarado and colleagues suggest that regulatory interactions between IHH and PTHrP result in Schnakenberg-like reaction kinetics (Garzon-Alvarado et al., 2009), which can give rise to Turing pattern (Gierer and Meinhardt, 1972). In particular, they postulate that the rate of PTHrP production and IHH removal are both proportional to the concentration of PTHrP squared times the IHH concentration ($[PTHrP]^2 [IHH]$). While IHH indeed enhances *Pthrp* expression (Karsenty et al., 2009), PTHrP signaling negatively impacts on its own expression (Kobayashi et al., 2005), which contradicts a key assumption of the model. Moreover, there is no experimental evidence that PTHrP would enhance IHH turn-over; PTHrP rather blocks *Ihh* production by preventing hypertrophic differentiation (Vortkamp et al., 1996) and down-regulates the action of IHH (Kobayashi et al., 2005). The reaction kinetics in the model are thus unlikely to reflect the physiological situation.

We had previously shown that the interaction of the Hedgehog protein with its receptor PTCH1 can result in a Schnakenberg-type Turing mechanism and that this mechanism can explain the observed patterning dynamics during lung branching morphogenesis (Menshykau et al., 2012). Unlike in the lung where an increasing number of branches appear as the structure is growing out, the number of patterns during endochondral ossification, however, does not increase (except for the late emergence of the secondary ossification center in each end (epiphysis) of the long bones). Moreover, as a result of cell differentiation during bone development the production rates of proteins changes contin-

uously. This is a challenge in any kind of Turing mechanism as Turing patterns typically arise only within a very small parameter range, the Turing space. We nonetheless found that a model that couples the IHH-PTCH1-based Schnakenberg-type Turing mechanism with the underlying tissue dynamics could still generate the observed patterns on a growing and differentiating tissue domain, i.e. the emergence of hypertrophic chondrocytes and *Ihh* expression in the centre of the domain, the predominance of proliferating chondrocytes towards the sides of the domain, and the emergence of a differentiation zone towards the centre of the domain (Tanaka and Iber, 2013). The inclusion of PTHrP was important to achieve robust patterning when coupling patterning and growth.

In spite of the good match of simulations and embryonic patterning dynamics, the model has two important limitations. For one, patterning only works for growth speeds that are similar to those observed in the mouse, while higher growth speeds as they may be present in jerboa (Cooper et al., 2013) would be difficult to accommodate. Moreover, while the model reproduced most mutant phenotypes it failed to explain the normal early patterning that is observed in the *Ihh*^{-/-};*Gli3*^{-/-} double knock-out (Hilton et al., 2005). Both in the wild-type and in the double knock-out *Pthrp* expression is restricted to the ends of the domain (Hilton et al., 2005). It thus seems that the main role of IHH signaling is to suppress the repressor action of the transcription factor GLI3 (Hilton et al., 2005), and that in the absence of IHH/GLI3 signaling there is an alternative patterning process that restricts *Pthrp* expression to the sides and thereby restricts the emergence of hypertrophic chondrocytes to the centre.

One possible mechanism, by which *Pthrp* expression may be restricted to the ends of the domain, are factors that are secreted by the joints. Various ligands from the TGF- β family are all present in the joints and SMAD3-dependent signaling has previously been shown to stimulate *Pthrp* expression (Pateder et al., 2000, 2001). In line with this, BMP receptor BMPR-IA (ALK3) signaling induces *Ihh* and *Pthrp* expression, and expression of a constitutive active form results in pattern reversal, similar to that observed when *Pthrp* is over-expressed (Zou et al., 1997). Similarly, constitutive active ALK2 in the developing chick limb bud induces *Ihh* and *Pthrp* expression and delays the formation of hypertrophic chondrocytes (Zhang et al., 2003). BMP-4 and GDF-5 bind to activin receptor-like kinase 3 (ALK-3) and/or ALK-6 (also termed BMP type IA and type IB receptors, respectively), whereas BMP-6 and BMP-7 preferentially bind to ALK-2 (Aoki et al., 2001). In the E14.5 limbs only *Alk-3/Bmpr1a* is found to be expressed in columnar proliferating and early hypertrophic chondrocytes, while the expression of all other BMP receptors is restricted to the perichondrium and bone (Minina et al., 2005). BMPs/GDF-5 in the joints may thus induce *Pthrp* expression in the perichondrium and *Ihh* expression in the pre-hypertrophic chondrocytes. BMP ligands signal through various receptors, but all canonical BMP signaling requires the CO-SMAD SMAD4. Early *Prx1-Cre*-mediated conditional inactivation of *Smad4* in the limb bud mesenchyme results in defects upstream of endochondral ossification and lack of collagen type II synthesis, a marker of proliferating maturing chondrocytes (Bénazet et al., 2012); in the *Prx1-Cre*-mediated mutant *Smad4* transcripts are absent already at E9.5 (Bénazet et al., 2012). Later conditional removal of *Smad4* with *Hoxa13-Cre* still permits *Sox9* expression in the digit ray primordia, but, interestingly, no cartilage or ossification is observed in the autopod

(Bénazet et al., 2012). TGF- β ligands, on the other hand, are no good candidates to stimulate *Pthrp* expression as conditional removal of the TGF β -type-II receptor (*T β RII*) in the limb enhances (rather than reduces) *Pthrp* expression (Spagnoli et al., 2007; Longobardi et al., 2012).

In summary, expression of *Pthrp* during endochondral ossification may be regulated by both BMP and IHH signaling. Both signaling pathways can be described by Schnakenberg-like reaction kinetics (Badugu et al., 2012; Menshykau et al., 2012), which can give rise to Turing pattern (Gierer and Meinhardt, 1972). Once *Pthrp* expression has been restricted to the outer parts of the condensations, the emergence of hypertrophic chondrocytes naturally becomes restricted to the center of the condensations, resulting in the characteristic pattern that is observed during endochondral ossification.

1.6. Conclusion

Biological functionality is largely controlled by sophisticated networks of interacting proteins. Much is known about the interactions that control organ growth and patterning, but until very recently, this information was largely presented in verbal models and cartoons. Due to the inherent complexity, experiments, in general, only validate small modules but not larger, integrated models. With the help of computational models it has recently become possible to integrate the available data in larger frameworks that begin to provide insights into apparently counterintuitive experimental data sets, detect inconsistencies in models and datasets, and have predictive power for new informative experiments. Such an integrative approach relies on careful experimental validation of all key elements of these models and simulations. Following their experimental validation, these models can be used for *in silico* genetics, i.e. their predictive power allows simulations of mutant states and the resulting phenotypes in situations when experimental generation and analysis of e.g. compound mutant embryos would be difficult or very time consuming. This will allow better focusing of research on the relevant genetic experiments and avoid the generation of uninformative mutant embryos. On the other hand, match and/or discrepancies between *in silico* and real genetics will reveal and/or improve the validity of the current mechanistic model. We illustrated this approach by the on-going development of *in silico* simulations of limb bud and digit development. Numerical solutions of these patterning processes are challenging, but will become progressively more feasible with advances in algorithms and computing power.

Part II.
Methods

2. Simulating Organogenesis in COMSOL

This chapter has been published as **Germann, P., Menshykau, D., Tanaka, S. and Iber, D.** (2011). Simulating Organogenesis in COMSOL. *Excerpt from the Proceedings of the COMSOL Conference 2011 in Stuttgart*. It gives a self-contained overview over our approach – i.e. employing reaction-diffusion equations to simulate organogenesis – and detailed information on the way we implement our models in the COMSOL Multiphysics finite element methods package.

Abstract

Organogenesis is a tightly regulated process that has been studied experimentally for decades. Computational models can help to integrate available knowledge and to better understand the underlying regulatory logic. We are currently studying mechanistic models for the development of limbs, lungs, kidneys, and bone. We have tested a number of alternative methods to solve our spatio-temporal differential equation models of reaction-diffusion type on growing domains of realistic shape, among them finite elements in COMSOL Multiphysics. Given the large number of variables (up to fifteen), the sharp domain boundaries, the travelling wave character of some solutions, and the stiffness of the reactions we are facing numerous numerical challenges. To test new ideas efficiently we have developed a strategy to optimize simulation times in COMSOL. We hope this information is helpful in reproducing our simulations or studying similar systems, but it is not essential to understand the results presented in the following chapters.

2.1. Introduction: Mechanistic Models for Organogenesis

Organogenesis is the process by which stem cells develop into organs in animals. In several systems important genes have been identified and the regulatory logic has been analyzed extensively over the last decades. The discovered regulatory networks are too complex to be understood intuitively and many questions remain open.

Organogenesis is a tightly regulated process, e.g. the lungs of two genetically identical embryos branch the same way (Metzger et al., 2008). This allows for deterministic modelling, which has been applied for decades to describe pattern formation in developmental biology (Kondo and Miura, 2011). Following this approach we were able to predict novel genetic regulations in the limb bud (Probst et al., 2011) and suggest a mechanism for lung branch mode selection (Menshykau et al., 2012) based on models implemented in

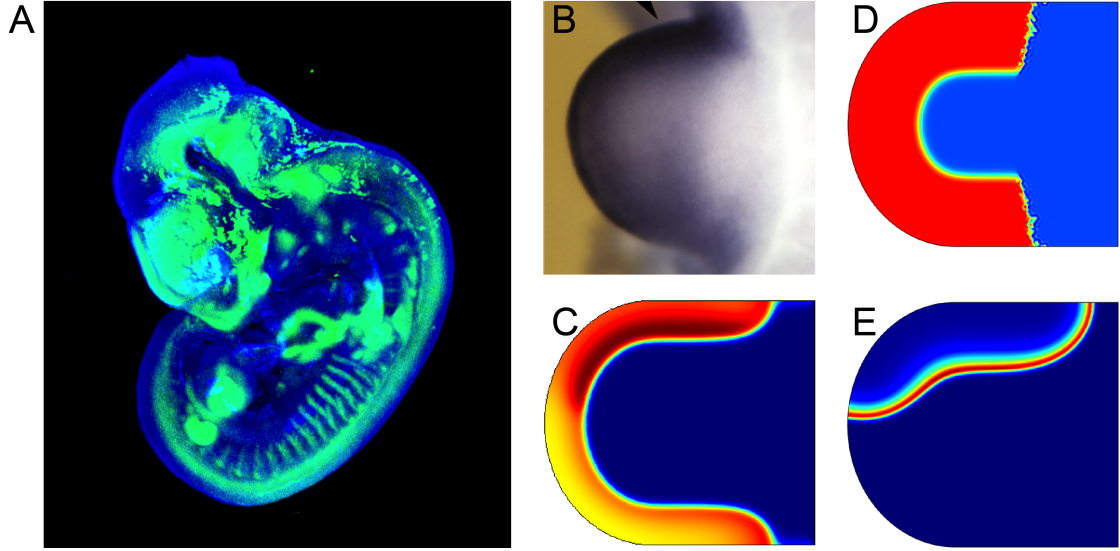


Figure 2.1.: Modelling gene expression patterns in the mouse limb bud. (A) Optical Projection Tomography (OPT) provides 3D information on gene expression patterns in the mouse limb bud (image courtesy of Frédéric Laurent and Emanuele Pignatti). (B) Classical in situ staining provides a 2D projection of the expression data. The image is a reproduction of *Bmp4* expression data from Figure 6B in Galli et al. (2010). (C) The experimental data can then be compared to the predicted spatial distributions of expression rates. (D, E) For some variables our model produces sharp domain boundaries (D) and traveling waves (E).

COMSOL Multiphysics, which has previously been shown to solve similar problems with a known analytic solution accurately (Thümmeler and Weddemann, 2007).

Our models are formulated as systems of reaction-diffusion equations of the form

$$\dot{X}_i + \nabla(u \cdot X_i) = D_i \nabla^2 X_i + R_i$$

where u denotes the velocity of the domain and R_i the reactions, which couple the equations for the different species X_i . D_i is the diffusion constant and ∇ the Nabla operator. The velocity might be imposed or based on concentrations of proteins, which change properties of the cells, like division rate or adhesion.

Our models typically involve three to fifteen species and typical reactions describe decay $R_X = -\delta \cdot X$ and complex formation

$$\begin{aligned} R_X &= -k^+ \cdot m \cdot X^m \cdot Y^n + k^- \cdot m \cdot X_m Y_m \\ R_Y &= -k^+ \cdot n \cdot X^m \cdot Y^n + k^- \cdot n \cdot X_m Y_m \\ R_{X_m Y_n} &= k^+ \cdot X^m \cdot Y^n - k^- \cdot X_m Y_m \end{aligned}$$

where $X_m X_n$ stands for the complex made of m X and n Y molecules. The reaction terms can contain also other non-linear functions like enzymatic activation σ and inhibition

$\bar{\sigma} = 1 - \sigma$, where σ is modelled analogous to Hill kinetics

$$\sigma = X^n / (X^n + K^n).$$

The threshold K is the concentration at which the activation reaches half its strength and the exponent n depends on the cooperativity of the regulating interactions. For example

$$R_X = \rho \cdot \sigma(Y)$$

describes a production term for a protein X induced by another protein Y.

2.2. Advances: Optimizing COMSOL Models

The non-linearities and different timescales in the reaction and diffusion terms produce traveling wave and sharp edges in the solutions, potentially rendering the models hard to solve numerically. In addition these equations have to be coupled to equations from continuum mechanics describing growth. Since very little is known about the parameter values and even the interactions are far from carved in stone we need efficient tools to explore multiple possibilities and together with the COMSOL support we have developed a strategy to optimize models in COMSOL.

Even before tuning solver settings singularities can be reduced by smoothening sharp corners with the fillet node and by using the inbuilt smooth step function, e.g. in initial conditions or spatially restricted reactions.

Some logarithmic derivatives in our models are very large in isolated points. The values of the different concentrations vary over several orders of magnitude and mask this stiffness. This leads the solver to take too large timesteps resulting in divergences in complex formations. Hence the next step is to produce a complete solution at any cost in order to identify the variables causing these spikes using a ‘sledge-hammer method’. This might include limiting the timesteps to very small values, updating the Jacobian at each iteration, tolerating only very small relative and absolute errors and using a very fine mesh. The linear solver MUMPS was found to be the most stable in our tests.

After scaling the variables in COMSOLs solver configurations node against the maximal values obtained we can relax the solver settings back to automatic time stepping and automatic dampening (updating the Jacobian). These optimized simulations also run on a very coarse mesh, but not in all cases fast and accurate, c.f. figure 2.2 A to D. The linear solver PARDISO turned out to be the fastest.

Using this strategy we were able to reduce computing times from initial 35 hours to 25 minutes in the limb bud model depicted in figures 2.1 and 2.2.

The oscillations around the sharp edges persist, but converge upon refining the mesh. Using COMSOLs consistent stabilization feature available in the chemical species transport module prevents these oscillations, but prolongs calculation times and might impact the resulting patterns.

Furthermore variables can be grouped and different solver settings applied sequentially to these groups using COMSOLs segregated solver feature. Random segregation in two

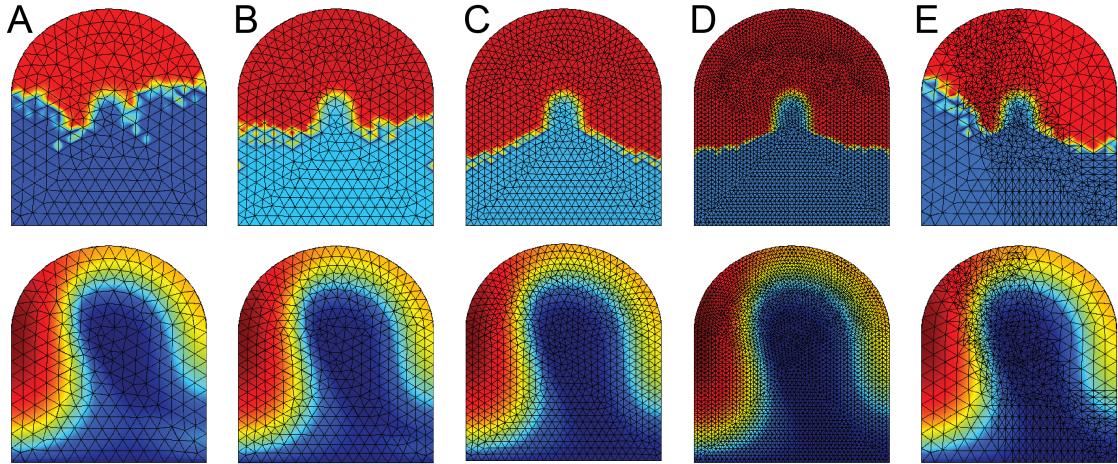


Figure 2.2.: Limb bud patterning: the impact of meshing on two of fifteen species. The first column (A) shows 528 elements and (B) 865 elements, both simulations take roughly half an hour on four cores. The calculation in (C) with 1749 elements runs 20% faster and (D) with 5847 elements takes three and a half hours. In the last column (E) artificial asymmetry from adaptive remeshing is shown on a calculation with roughly 1700 elements. The mesh is remeshed according to the gradient of the traveling wave of complex formation introduced in figure 2.1 (E).

or three groups quadruplicated the computing time; on the other hand segregating variables based on biological considerations (e.g. co-regulation of patterning events such as proximal-distal and anterior-posterior axis formation) allowed us to reduce the computing time below nine minutes. Interestingly isolating the variables that together caused spikes in our initial model allowed us to reduce the computing time even further from 25 minutes to five minutes.

COMSOL was reported to provide significant speed-up for a problem with 1.3 million degrees of freedom¹. We also ran our limb bud model in parallel on a single node (i.e. no MPI), but the speed-up turned out to be poor. While our limb bud model may have been too small for efficient parallelization, further tests with larger models in three dimensions did not yield any improvements (figure 2.3). The data was collected using PARDISO, but the other linear solvers did not perform better.

We also benchmarked adaptive remeshing since our test model exhibits localized features, like the traveling waves and sharp edges. However it did not accelerate the calculations further and adaptive remeshing can introduce artificial asymmetries as shown in figure 2.2E, since for instance the effective diffusion depends on the discretization.

¹http://www.comsol.com/shared/downloads/partners/Comsol_datasheet_Final_Web.pdf

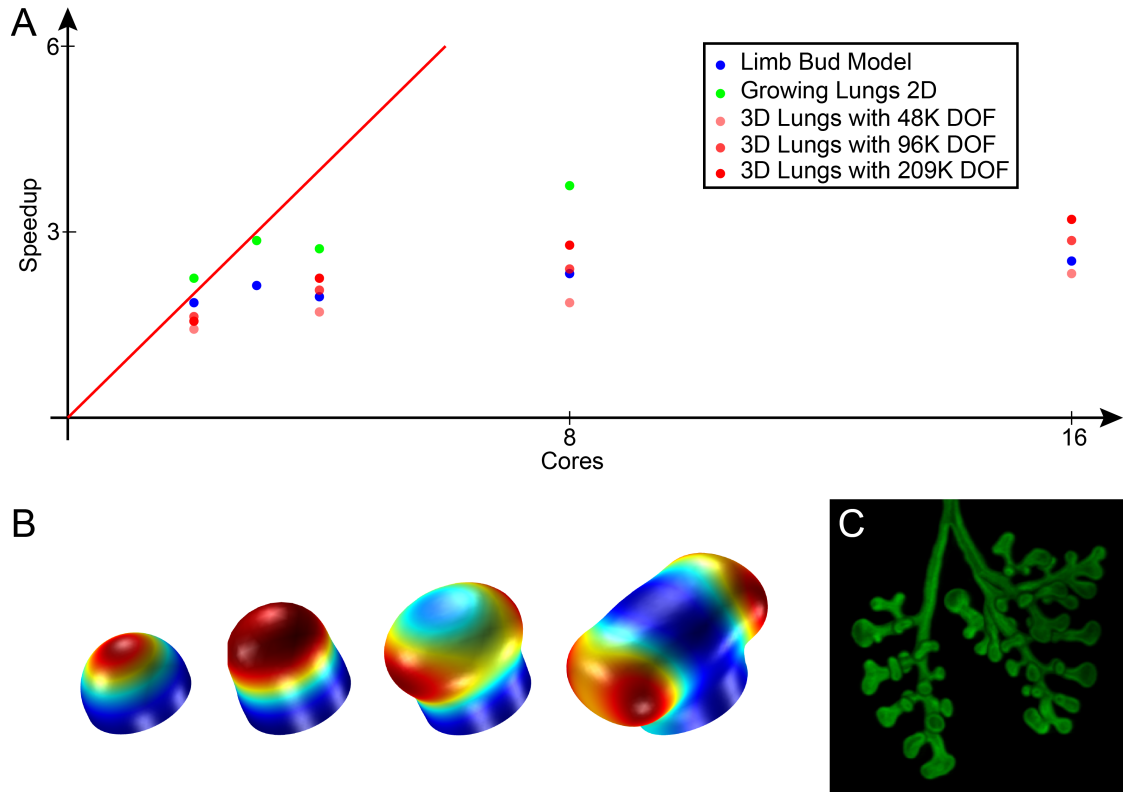


Figure 2.3.: (A) Speed-up of different models upon parallelization (strong scaling). The red line shows the theoretically maximal possible linear speed-up and the dots are ratios of computing time at a certain number of cores divided by computing time using a single core. (B) The 3D lung branching model referred to in A. Its shape arises from displacements along the surface normal at velocities proportional to the morphogen concentration shown on the surface. (C) Three dimensional imaging data of the lung epithelium in a developing mouse embryo.

2.3. Challenges: Large Deformations

To describe deforming domains due to growth we applied the ALE moving mesh module. Since the meshes of the subdomains adjacent to the moving boundary get distorted and stretched or squeezed, the mesh quality quickly worsens. The recent COMSOL version 4.2 features automatic remeshing to overcome this, cf. figure 2.4A. The principle is simple: a measure for quality is calculated regularly for each mesh element. Whenever this mesh quality falls below a predefined barrier, the entire domain is remeshed. In spite of not yet fully exhausting the possibilities we give a short summary of the experiences collected so far.

For uniform models with smooth deformations automatic remeshing usually worked well, but when more sophisticated meshing settings, e.g. different properties for subdo-

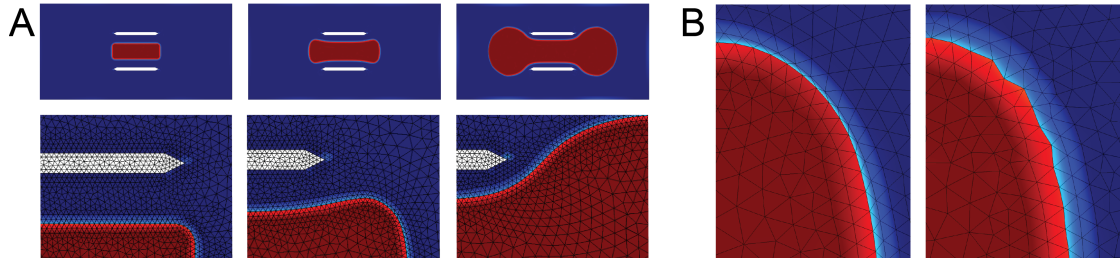


Figure 2.4.: The new remeshing feature illustrated with a model for long bone growth (A). It consists of a fluid governed by the Navier-Stokes equations, with a mass source as plotted, between two walls, simulated using the creeping flow node. The mesh quality was kept above 0.4 with 42 remeshing steps. On the right side a comparison between Laplacian and Winslow smoothing is given (B).

mains, are needed they might no longer be appropriate due to large deformations and the mesher may no longer be able to create a mesh with the desired quality leading to abortion.

Setting the shape order to linear reduces the number and delays the appearance of inverted elements and Laplacian smoothing worked best for avoiding inverted elements, cf. figure 2.4B.

The meshing and fine resolution of the moving boundary are crucial for successfully running the bone model depicted in figure 2.4 with large deformations.

When a highly resolved moving boundary moves too close to a low-resolution external boundary during a simulation restricting element growth can save the meshing algorithm from failing. Solver settings similar to those described as ‘sledge hammer method’ in the previous section allowed simulations to run further. Enforcing frequent remeshing by demanding high mesh quality further supported this.

2.4. Conclusions & Outlook: Studying Growth in 3D

COMSOLs powerful interface and vast features allow us to implement new ideas quickly and to test them efficiently. Based on benchmarks with Discontinuous Galerkin Methods implemented in DUNE-FEM (Dedner et al., 2010) we expect that our computing times are in a reasonable range.

With the recent automatic remeshing feature of COMSOL it becomes technically feasible to run our models on realistically growing domains. This requires us to couple the gene regulatory networks to fluid or solid- state equations, which creates additional numerical difficulties. Preliminary simulations of the limb bud model shown in figures 2.1 and 2.2 in three dimensions required several days to run. In spite of important advances in our computational workflow there are still large challenges ahead.

Part III.

Results

3. A Model for Anterior-Posterior Limb Bud Patterning

This chapter is adapted from a draft submitted to *Development* as **Germann, P. and Iber, D.** A Data-based Computational Model for the Epithelial-Mesenchymal SHH/BMP/GREM1/FGF Feedback Loop in Limb Bud Development.

3.1. Introduction

Vertebrate limb development has been studied for decades and much is known about the regulatory interactions that control limb bud patterning and growth (Iber and Zeller, 2012; Zeller et al., 2009). However, given the complexity of the regulatory interactions (figure 3.1A) it has become impossible to analyze the network and emerging dynamics by verbal reasoning alone.

A large number of theoretical models of limb development have been proposed (Zhang et al., 2013), but these mainly focused on the growth dynamics of limb buds Boehm et al. (2010); Ede and Law (1969); Marcon et al. (2011); Morishita and Iwasa (2008a, 2009); Popławski et al. (2007) or on digit patterning (Miura, 2013; Newman and Frisch, 1979; Wolpert, 1969). Some models simulated interactions between the main signaling centres without much genetic detail (Dillon and Othmer, 1999; Dillon et al., 2003; Morishita and Iwasa, 2008b) or without consideration of the spatial inhomogeneity in the limb bud (Bénazet et al., 2009). We have previously proposed mechanistic, spatio-temporal models for signaling interactions that control proximal-distal limb axis development (Probst et al., 2011) and for those that may specify digit condensations (Badugu et al., 2012). In the present analysis we focus on the so-called epithelial-mesenchymal (e-m) feedback loop between the apical ectodermal ridge (AER) and the zone of polarizing activity (ZPA) that orchestrate anterior-posterior limb axis formation and interlink it with the control of the proximal-distal axis patterning.

We carefully develop a spatio-temporal model based on reaction-diffusion equations that comprehensively describes and reproduces a large number of functional studies carried out in wildtype (wt) and several mutant limb buds. The model is based mainly on data gathered by analyzing limb development in mouse embryos, but some studies using chicken limb buds are also incorporated where no mouse data is available. By deriving a model that is consistent with the available genetic data from analyzing mouse limb buds we are able to define the core regulatory network. Our simulations show that it is now possible to integrate experimental data on complex regulatory networks into a computational framework that provides a much deeper mechanistic understanding and a dynamic view on the spatio-temporal regulatory interactions. The simulations also reveal

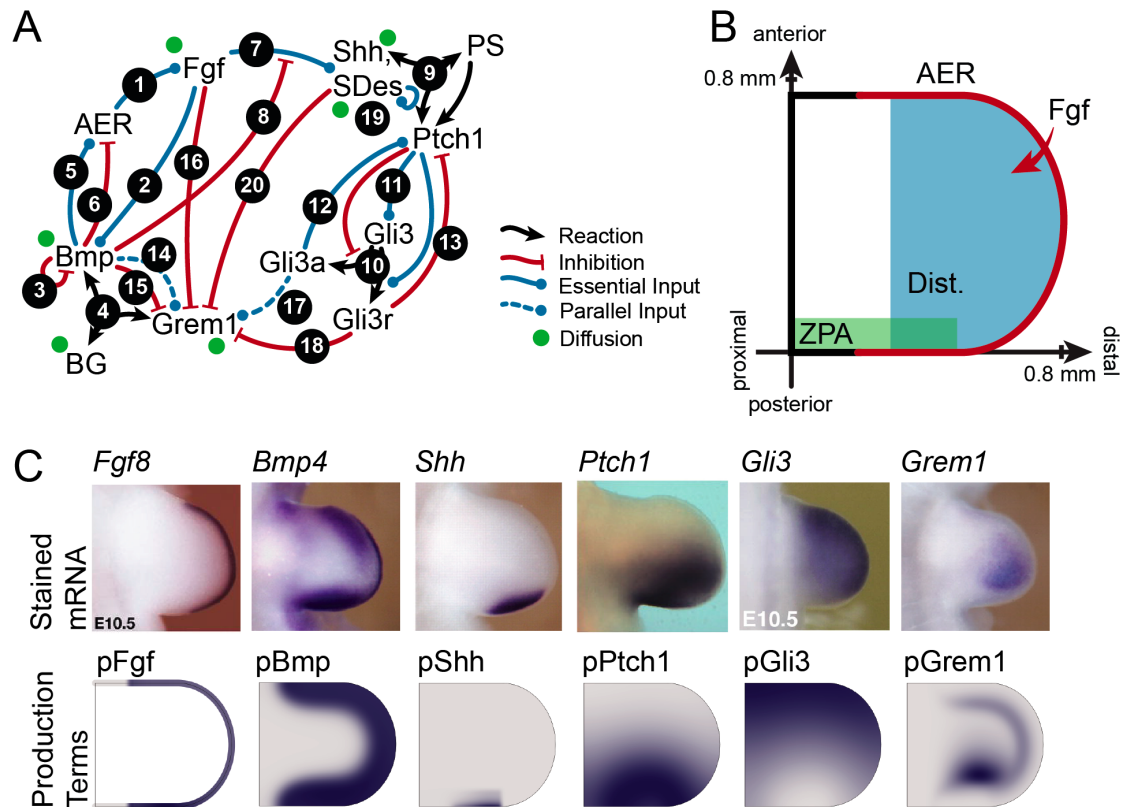


Figure 3.1.: A model for limb development. (A) The simulated network. Here Fgf represents all AER-secreted FGFs, and Bmp all mesenchymal BMPs. Blue arrows indicate activating regulatory interactions (dashed lines indicate parallel, independent inputs), red arrows indicate inhibitory interactions, black arrows indicate biochemical reactions. Numbers indicate the different reactions. For details see text. (B) The simulated domain. The green area indicates the permissive region for Shh production (ZPA), the blue area the permissive area for Grem1 production, and the red area the permissive region for Fgf production (AER). (C) Comparison of mRNA ISH at E10.5 with predicted production terms in our simulation (Bénazet et al., 2009, 2012; Li et al., 2006; López-Ríos et al., 2012).

gaps in the understanding and stress the importance of data derived from quantitative or time-series experiments. We expect that our model will be a valuable resource to the field.

The key diffusible, extracellular signaling proteins that control patterning of the anterior-posterior axis during limb development are Bone Morphogenetic proteins (BMPs), their antagonist GREMLIN-1 (GREM1), Fibroblastic Growth Factors (FGFs), and SHH (figure 3.1A). We sought to create a parsimonious model, and we therefore do not distinguish between the different *Bmps*, which are expressed in the mesenchyme (*Bmp2*, *Bmp4*, *Bmp7*), and only consider one single BMP component in the model. Similarly, we do not

distinguish between the different *Fgfs* (*Fgf4*, *Fgf8*, *Fgf9*, *Fgf17*) that are expressed in the AER (depicted as red line in figure 3.1B), and only consider a single AER-FGF component in the model. The mesenchymal FGF10 mainly maintains the AER via WNT3 (Barrow et al., 2003; Danopoulos et al., 2013), and since this process will not be modelled explicitly we do not include FGF10 in the model. SHH plays an important role in the patterning of the anterior-posterior (AP) axis (Riddle et al., 1993), and previous work in *Drosophila* has shown that the Hh-dependent signaling network results in a wave-like dynamic signaling pattern (Nahmad and Stathopoulos, 2009). We therefore include a larger level of detail about SHH-dependent signaling, i.e. the SHH receptor PTCH1, and the intracellular transcription factor GLI3, which can be proteolytically processed into two forms, GLI3A and GLI3R.

Mouse forelimbs grow out from the flank and become visible around embryonic day (E) 9. Expression of *Shh* is restricted to the posterior part of the limb bud, to the so-called zone of polarizing activity (ZPA), and becomes first visible around E9.75 and is lost in the forelimb by E12.25 (Echelard et al., 1993; Riddle et al., 1993; Towers and Tickle, 2009). We will simulate patterning of the AP axis between E9 and E12. In that time, the limb buds grow linearly to a length of about 2mm in proximal-distal (PD) and 1mm in AP direction (Badugu et al., 2012). To keep the model as simple as possible, growth will not be included in the current model, and we will solve our model on a static 2D domain that idealizes the E10.5 limb bud shape (0.75 mm in PD and 0.75 mm in AP direction, figure 3.1B).

We constructed the network to reproduce all published limb phenotypes of the available mutants, and obtained the network in figure 3.1A as the one to be consistent with all published information. The model construction is described in the following. We follow a modular approach in that we did not strive for simplified equations, but for modules of interacting proteins that can be easily extended or exchanged. We tested the model extensively by comparing model predictions to experimental data (figure 3.1C). As can be seen in figure 3.1C the spatial distribution of the production terms in the model reproduces the wt expression patterns of the core signaling factors very well.

3.2. Mathematical Framework

Our model is formulated as a set of coupled reaction-diffusion equations of the form

$$\dot{X} = D_X \Delta X + R_X.$$

In this equation, X represents the concentration of a component (e.g. BMP), \dot{X} denotes the change of X over time, D_X the diffusion constant of X , and Δ the Laplace operator of the diffusion term. R_X is the reaction term of component X and describes the relevant regulatory interactions shown in figure 3.1A. The set of equations is given in the Supplementary Material.

Before discussing the experimental evidence in detail that led us to the network in figure 3.1A and the reaction terms, R_X , that describe it, we will first briefly explain the general building blocks. We will consider four reaction types: production, degradation,

processing, and complex formation. The reaction terms are modulated by regulatory terms that will be introduced below. We assume that the rate of degradation is proportional to the concentration of component X (linear degradation, i.e. $R_X = -\delta_X \cdot X$). Similarly processing of molecules is modelled as linear turnover (i.e. a reaction term of the form $\tau = k_X = -k_Y = k \cdot Y$ for turnover of Y into X). The formation of a complex $[X^m Y^n]$ consisting of m molecules of species X and n molecules of species Y can be described by the reaction term

$$\chi_{X^m Y^n} = R_{X^m Y^n} = -R_X/m = -R_Y/n = k^+ X^m \cdot Y^n - k^- [X^m Y^n],$$

where k^+ is the rate of complex formation and k^- the rate of dissolution. In each reaction m molecules of X and n molecules of Y are involved.

All reaction rates can be modulated by regulatory interactions. These will be captured by second order Hill kinetics. We distinguish activation $\sigma(A)$ by activator A and inhibition $\bar{\sigma}(I)$ by inhibitor I, i.e.

$$\begin{aligned}\sigma(A) &= A^2/(A^2 + K^2) \\ \bar{\sigma}(I) &= K^2/(I^2 + K^2).\end{aligned}$$

The threshold K is the Hill constant, which is specific for each of the regulatory interactions considered.

We constructed the model in a step-wise manner based on the published experimental evidence. At each stage we set the parameter values by comparing simulation results with experimental observations in wt and mutant limb buds and revisited the equations if needed. We describe the process after introducing the resulting model in detail.

The parameter values are summarized in section 3.6. In total, the model comprises 58 parameters, including production (12), decay (13), reaction rates (4), Hill constants (17), diffusion coefficients (6), and length scales (6). The length and time scale of the process are well established, as are the (sometimes wide) physiological ranges for the diffusion, decay, and reaction rates (table 3.2). Strikingly, we recovered the order of magnitude of the measured GLI3 half-life (Harfe et al., 2004; Wen et al., 2010) by optimizing the model only to reproduce the measured gene expression patterns. The protein concentrations are largely unknown, as are the protein expression rates and Hill constants. The protein expression rates and the response thresholds (Hill constants) are directly related, and in a non-dimensional version of the model we would retain only one of these as free parameter; this parameter is determined by the experimentally observed spatio-temporal regulatory pattern. We nonetheless chose to work with the dimensional counterpart because the parameter values can be more easily compared to the physiological situation and non-dimensionalization would have removed only 14 of the 58 parameters.

Striving for a simple, parsimonious model that explains the experimental observations we identified the most important key players and left out detailed molecular interactions about particular signaling cascades and protein synthesis. Thus, protein production is modelled as a 1-step process, i.e. we do not resolve potential differences between mRNA levels and protein formation, due to post-transcriptional regulation or similar. The omission of mRNA and intermediate signaling steps – like BMP and FGF receptors

and signaling cascades – affects the timing of processes and the shape of gradients. Thus, for some of the proteins (e.g. BMP) we have to use longer half-lives than have been measured to compensate for the lack of delays in the omitted signaling cascades, and some gradients (e.g. FGF) are mainly shaped by degradation and diffusion as we do not consider sequestration by receptors in our model.

Experimental analysis has been largely focused on the transcript level in the developing limb bud. Thus, mRNA in situ hybridization (ISH) analysis reveals the qualitative, spatial mRNA distributions in the limb buds, and quantitative PCR (qPCR) data reveal the relative transcript levels in particular stages and/or parts of limb buds. Therefore, we compare the effective (i.e. the spatio-temporally regulated) production rates to the experimentally reported transcript distributions as shown in figure 3.1C. ISH images from published studies are shown in parallel to the simulated production terms for the key regulators of limb development that we consider in the present study. The simulated production domains are, in general, very similar to the observed expression domains and emerge directly from the regulatory interactions. There are three exceptions: the restriction of *Shh* expression to the zone of polarizing activity (ZPA), the restriction of ectodermal *Fgf*-expression to the apical ectodermal ridge (AER), and the restriction of *Grem1* expression to the distal part of the limb bud do not emerge from the regulatory interactions, and therefore had to be imposed by using smoothed heavy-side functions, θ , that limit the expression to the broad zones shown in figure 3.1B (maximal limit of the ZPA shaded in green, distal restriction shaded in blue, AER corresponds to the red part of the boundary). Importantly, these restrictions mainly prevent production of these three variables in the other parts of the limb domain. Within these restricted areas the regulatory interactions further restrict the production zones to give rise to the characteristic shape of the production patterns (figure 3.1C, lower panels) that match the experimental expression domains rather well (figure 3.1C, upper panels).

In the following we describe how we developed the signaling network for our simulations based on published experimental data. For clarity we use *XYZ* to indicate genes and transcripts and *XYZ* for the corresponding protein. In addition we use *Xyz* to indicate the variable in our computational model, and *pXyz* for the protein production rate in our model, which we compare to the experimentally measured transcript distributions.

3.3. Mutual Inducing Interactions Between AER-FGFs and BMPs Initiate the Limb Bud Signalling Network

The AER limb bud signaling center secretes AER-FGFs (interaction 1)

The apical ectodermal ridge, AER, is crucial for outgrowth of the limb bud (Saunders, 1948). The AER secretes FGF4, FGF8, FGF9 and FGF17 (interaction 1) and genetic inactivation of several AER-*Fgfs* truncates limb bud development (Lu et al., 2006; Mariani et al., 2008). In chicken flanks, implantation of beads soaked in FGF4/8 and grafts of *Fgf8* expressing cells induce ectopic limbs (Crossley et al., 1996; Ohuchi et al., 1997). *Fgf8* is expressed first and throughout the AER and its inactivation in the AER results

in loss of skeletal elements (Lewandoski et al., 2000).

We describe the activity of all AER-FGFs in one variable Fgf , which is secreted from the distal boundary (figure 3.1B, red line) proportionally to the levels of the variable AER representing width and thickness of the AER. The secretion is included in the model as flux boundary condition for Fgf , i.e.

$$\vec{n} \cdot \nabla Fgf = \rho_{Fgf} \cdot AER$$

where \vec{n} is the unit vector normal to the boundary, ρ_{AER} the production rate and the equation for variable AER is an equation on the boundary and not throughout the domain.

BMP Dynamics (interactions 2-6)

While several different *Bmps* are expressed in the limb bud, we will keep the model simple and only use one variable Bmp that represents all signaling by mesenchymal BMPs. The simulated Bmp production pattern is most comparable to mouse *Bmp4* transcript distribution. We focused on the *Bmp4* expression pattern in our simulation, because *Bmp4* is widest expressed (Hogan, 1996) and the phenotype of *Bmp4*^{-/-} mutants is most severe (Bandyopadhyay et al., 2006; Selever et al., 2004).

The AER-FGFs induce mesenchymal *Bmps* (interaction 2) The AER-FGFs enhance the expression of *Bmp2*, *Bmp4* and *Bmp7* in the underlying mesenchyme (interaction 2). Thus *Shh-Cre*-mediated inactivation of *Fgfr1/2* in mesenchymal cells expressing *Shh* causes loss of *Bmp4* expression in these cells (Verheyden et al., 2005; Verheyden and Sun, 2008; figure 3.2A).

BMPs down-regulate their own expression (interaction 3) BMP2 beads have been shown to down-regulate and beads soaked with the BMP antagonist NOGGIN up-regulate expression of *Bmp2*, *Bmp4* and *Bmp7* in chicken limb buds (Bastida et al., 2009; figure 3.2B).

In summary, as Fgf activates and Bmp inhibits Bmp production we obtain as Bmp production term in our model

$$pBmp = \rho_{Bmp} \cdot \sigma(Fgf) \cdot \bar{\sigma}(Bmp) + Bmp_0 \cdot \delta_{Bmp} \quad (3.1)$$

where we added a small constitutive production rate $Bmp_0 \cdot \delta_{Bmp}$ to initiate Bmp at a low steady state level Bmp_0 (see below).

Ectodermal BMPs & SHH-dependent *Bmp* expression *Bmps* are also expressed in the AER (Choi et al., 2012; Maatouk et al., 2009). SHH beads and virally expressed *Shh* induce expression of *Bmp2* and *Bmp7* in the vicinity of the chicken AER (Laufer et al., 1994; Nissim et al., 2006; Yang et al., 1997) and *Bmp2* has been identified as GLI-target in the mouse (Vokes et al., 2008). The expression of AER-secreted FGFs is also enhanced by SHH signaling (Aoto et al., 2002). Since the phenotypes of mutants with

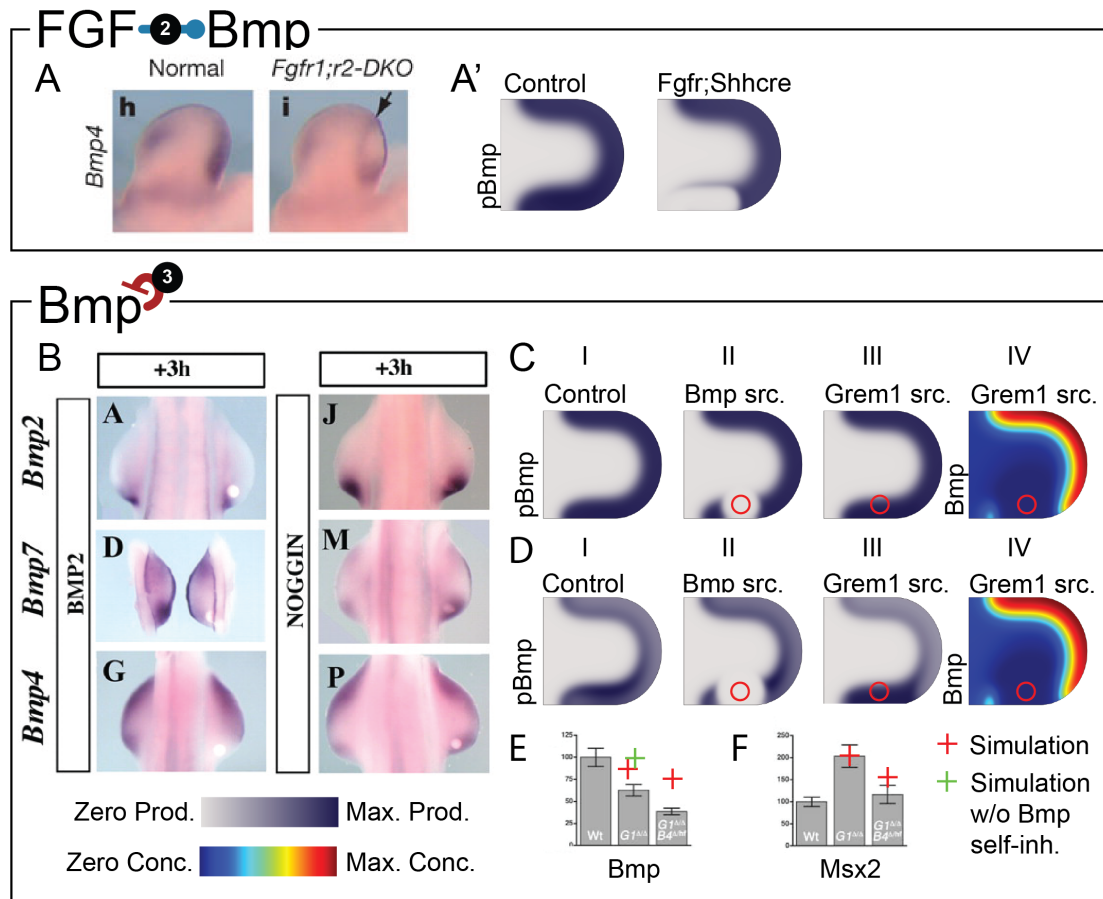


Figure 3.2.: Regulation of Bmp production. (A, A') Fgf induces Bmp production. (A) Data: Upon inactivation of *Fgfr1* and *Fgfr2* by *Shh-Cre* expression of *Bmp4* is lost in the ZPA by E10.75 (Verheyden et al., 2005). (A') Simulation: Lack of Fgf regulatory impact in the region covered by Sonic Descendants (SDes) results in lack of Bmp production in the posterior. (B-E) Bmp is self-inhibiting. (B) Data: BMP-loaded beads down-regulate, while beads loaded with BMP antagonist NOGGIN up-regulate expression of mesenchymal *Bmps* (Bastida et al., 2009). (C) Simulation: (I) Bmp production. (II) Local Bmp sources reduce Bmp production. (III) A local *Grem1* source increases Bmp production only mildly, (IV) even though the concentration of free Bmp is strongly reduced. (D) Simulation: Stronger self-inhibition of Bmp yields a more pronounced effect of local *Grem1* sources on BMP production (III), but result in stronger Bmp production towards the centre (I). (E) Data and Simulation: *Bmp4* is down-regulated in mutants lacking its antagonist *Grem1* ($G1\Delta/\Delta$) as shown in the bar plots. An additional genetic reduction of *Bmp4* expression leads to further down-regulation of *Bmp4* expression ($G1\Delta/\Delta$, $B4\Delta/hf$). The red + signs indicate the predicted effects from the model. The green + sign denotes the results from a model without Bmp self-inhibition. (F) Data and Simulation: The BMP target gene *Msx2* is up-regulated in *Grem1* mutants. The additional genetic reduction of *Bmp4* rescues the phenotype (Bénazet et al., 2009). The + signs indicate the predicted values from the model.

inactivated *Bmp2* or *Bmp7* in the mesenchyme (Bandyopadhyay et al., 2006) or *Smo* in the AER (Bouldin et al., 2010) are mild we neglect the SHH-dependent regulation of Bmp production and an influx of Bmp from the AER boundary in this parsimonious model.

GREM1 antagonizes BMP by sequestration (interaction 4) GREM1 antagonizes BMP (Hsu et al., 1998) by forming an inactive BMP-GREM1 complex. Bmp and Grem1 thus reversibly form an inactive complex (interaction 4), which we denote BG in our model. According to the law of mass action the complex formation and dissolution is described as

$$\chi_{BG} = k^+ \cdot \text{Bmp} \cdot \text{Grem1} - k^- \cdot \text{BG}.$$

To validate our model of Bmp production, we checked that the simulations indeed reproduce the experiments on which we base our equations. The effects of *Shh-Cre*-mediated inactivation of *Fgfr1/2* (Verheyden and Sun, 2008; Verheyden et al., 2005) can be simulated by inhibiting all Fgf signals in those parts of the limb bud mesenchyme that produce or that have produced Shh. Much as observed by genetic analysis (figure 3.2A), Bmp is no longer produced in the region of the mesenchyme where all Fgf signaling is blocked (figure 3.2A').

The effect of protein-loaded beads can be simulated by adding a Gaussian shaped protein source (indicated as red circles in figure 3.2C,D) to the reaction term of the respective variable, i.e.

$$R_{Source} = \rho_{Source} \cdot \theta(t - t_0) \cdot e^{-((x-x_0)^2 + (y-y_0)^2)/r^2},$$

Here θ indicates a Heaviside function and we use $r = 0.05\text{mm}$. As observed experimentally (figure 3.2B), a local Bmp source reduces Bmp production, pBmp, in our simulation (figure 3.2C II). NOGGIN and GREM1 both interfere with BMP signaling by sequestering the ligands in inactive complexes (Hsu et al., 1998; Zimmerman et al., 1996). Therefore we simulate the effects of BMP antagonist loaded beads in our model by addition of a local Grem1 source. Such a Grem1 source augments the Bmp production only very little in our model (figure 3.2C III), despite the strong local reduction in the amount of free Bmp around the source (figure 3.2C IV). This suggests that the impact of Bmp self-inhibition is too weak in our model. A seven-fold lower Bmp self-inhibition threshold (figure 3.2D) would indeed increase the inhibitory effect of a Grem1 source (figure 3.2D III). However, it would also yield stronger Bmp production towards the centre of the limb bud (figure 3.2D, panel I), which is not observed in experiments (figure 3.2A). In addition, higher Bmp self-inhibition would impair the down-regulation of Fgf and Shh in the absence of Grem1 as described below. At least in the context of our model, Bmp self-inhibition can at most play a minor role. It should be noted that to distinguish plots of concentrations from plots of production rates, we plot the values of the variables in our simulations in a rainbow colour code (figure 3.2C,D, panels IV); production rates are plotted in a colour code similar to ISH images (figure 3.2C,D, panels I-III).

To quantitatively validate our model we compared the total production rates with expression rates of *Bmp4* (figure 3.2D) and BMP target *Msx2* (figure 3.2E) quantified by

qPCR in wild-type, *Grem1*^{-/-} and *Grem1*^{-/-};*Bmp4*^{-/hf} mutants (Bénazet et al., 2009). Total production rates are obtained by integrating over the entire domain. In the absence of *Grem1* our model predicts a 15% reduction of *Bmp* production (figure 3.2E, red arrow) while qPCR measurements suggest a 30% reduction. Without *Bmp* self-inhibition (interaction 3) we observe only a 5% reduction (figure 3.2E, green arrow). Much as in the case of the bead experiments (figure 3.2B-D) this suggests that the auto-inhibitory effect of *Bmp* on its own production is too weak in the model; higher levels of self-inhibition could, however, not be accommodated in the model without negatively affecting other patterns. The additional reduction of *Bmp* expression in *Grem1*^{-/-};*Bmp4*^{-/hf} mutants leads to a further strong reduction in *Bmp* expression in the qPCR data (figure 3.2E). When we reduce the *Bmp* production rate by 25% in the *Grem1*-deficient simulations, also our model predicts a further reduction in the *Bmp* production, however only to about 75% (instead of 40%) of the total wild-type *Bmp* production; stronger reductions in *Bmp* production would prevent us from capturing other transcript read-outs (see below). The expression of the BMP target gene *Msx2* is strongly up-regulated in *Grem1*^{-/-}, and this up regulation can be compensated by reducing also *Bmp* expression in *Grem1*^{-/-};*Bmp4*^{-/hf} mutants (figure 3.2F; Bénazet et al., 2009). When we make *Msx2* production dependent on *Bmp* signaling then the model reproduces the qPCR results (figure 3.2F, red arrows). The quantitative differences between model and qPCR experiments show the limits of capturing the behaviour of such complex dynamics with a relative simple model – and also demonstrate that the model is sufficiently constrained by the amount of available data, that, in spite of the large number of parameters, the model predictions cannot be adjusted arbitrarily. At the same time, the fact that all behaviours are captured qualitatively, supports the general wiring of the network interactions.

Mesenchymal BMPs regulate the AER (interactions 5, 6) FGF and BMP signaling are part of a positive feedback loop by which FGF signaling enhances *Bmp* expression (interaction 2) and BMP signaling in turn is needed for AER formation during the onset of limb bud development (interaction 5). Subsequently, BMPs exert a negative effect on AER-FGF secretion (interaction 6). The impact of BMPs on the AER has been demonstrated using *Bmp2* expressing cells, which induce *Fgf4* in the anterior chicken AER (Duprez et al., 1996). Inactivation of BMP receptor *Bmpr1a* during AER formation (Ahn et al., 2001; Pajni-Underwood et al., 2007) or inactivation of *Bmp4* in the mesenchyme (Bénazet et al., 2009; figure 3.3A) disrupts AER-FGF signaling. In contrast, inactivation of *Bmps* in the AER results in an elongated and expanded AER (Choi et al., 2012; Maatouk et al., 2009). Similarly, inactivation of mesenchymal *Bmps* at later stages leads to an expansion of the AER (Bandyopadhyay et al., 2006; Bénazet et al., 2009; Pajni-Underwood et al., 2007; figure 3.3B) and over-expression of *Noggin* in the AER prolongs AER-FGF signaling (Wang et al., 2004). In *Grem1* deficient limb buds AER-*Fgf8* expression is reduced (figure 3.3C), a phenotypic effect that is partially restored by inactivating one *Bmp4* allele (figure 3.3D; Bénazet et al., 2009).

Retinoic acid has been suggested to restrict the expression of AER-*Fgfs* to the distal part of the limb bud (Probst et al., 2011). However, as the patterning of the proximal-

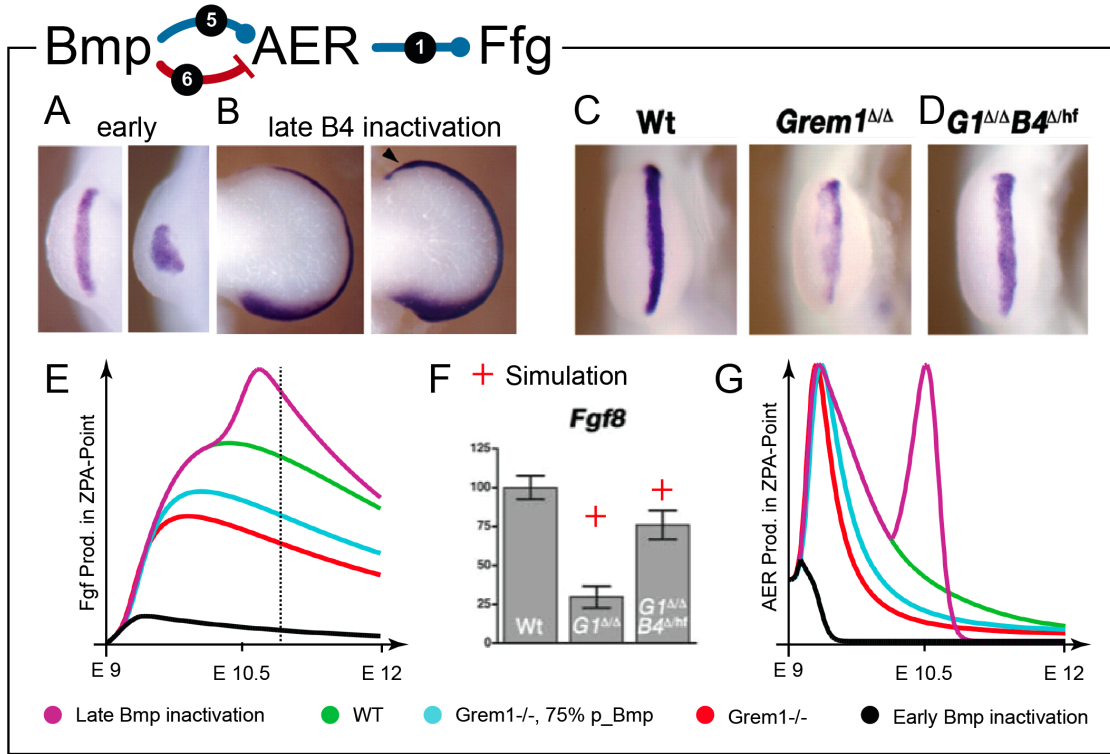


Figure 3.3.: Regulation of the AER. (A) Early inactivation of mesenchymal *Bmp4* expression at E8.75 disrupts AER formation by E10.25 (B) Later inactivation at E9.25 results in extended *Fgf8* and *Shh* expression at E11.75. (C) Mutants lacking BMP antagonist *Grem1* show less *Fgf8* expression, (D) which can be partially restored by deleting one *Bmp4* copy. (E) Predicted Fgf production in a single point of the ZPA for the situations shown in (A-D). (F) Comparison of the predicted total Fgf production marked with + signs to *Fgf8* expression quantified by qPCR for the mutants shown in (C, D). (G) The direct input from Bmp signaling on AER formation allows for different timings in mutants, but peaks always reach the same maximal value. The data in this figure was reproduced from B n zet et al. (2009).

distal axis is not the primary subject of this model we restrict the Fgf production domain with an smoothed heavy-side function θ_{AER} to the distal part of the boundary marked in red in figure 3.1B.

In summary, mesenchymal BMP is needed for AER formation (interaction 5) during onset of limb bud development, while subsequently it limits the extent of the AER (interaction 6). Therefore we implement in our equations that low Bmp levels induce, while high Bmp levels inhibit AER formation on the boundary restricted by θ_{AER} , i.e

$$p_{\text{AER}} = \rho_{\text{AER}} \cdot \sigma(\text{Bmp}) \cdot \bar{\sigma}(\text{Bmp}) \cdot \theta_{\text{AER}}.$$

We initiate the positive feedback between Fgf and Bmp in our model by starting our

simulations with a low Bmp concentration, $Bmp_0 = K_{\text{AER}}^{\text{Bmp}}/5$, which is achieved by the small constitutive production rate in equation (3.1) that we mentioned earlier; this may represent the effect of FGF10 via WNT3 on *Bmp* and *Fgf* expression in the AER (Barrow et al., 2003). We do not explicitly include the feedback loop between mesenchymal FGF10 and the AER-FGFs that initiates and maintains expression of AER-*Fgf* (Ohuchi et al., 1997; Sekine et al., 1999).

The resulting model reproduces the published experimental data on BMP functions as shown in figure 3.3E. In this figure, we plot the simulated effective production rate of *Fgf* at a single point in the AER for wt and the mutant limb buds discussed above. Thus, when we turn off the production of Bmp at an early stage, *Fgf* production brakes down (figure 3.3E, black curve). In contrast, when we turn off production of Bmp at a later stage, *Fgf* production is increased (figure 3.3E, purple curve) in comparison to the wt (figure 3.3E, green curve). Similarly, the reduced expression of *Fgf* in a simulation lacking *Grem1* (figure 3.3E, red curve) can be partially restored by lowering the Bmp production rate to 75% (figure 3.3E, cyan curve). A similar qualitative correspondence is also observed between qPCR and model results (figure 3.3F), though the quantitative effects of the *Grem1*^{-/-} and *Grem1*^{-/-};*Bmp4*^{-/hf} on *Fgf8* transcript levels are stronger in the embryo than in the simulations (figure 3.3F, red arrows). Here the qPCR data, which provide a quantitative measure of the changes in the total transcript level, were compared to the integral over the entire AER.

We note that the inclusion of the additional equation for the AER as an intermediate step between Bmp signaling and *Fgf* production has two important effects in the model. For one it provides the crucial delay that allows us to reproduce the observed change in the regulatory impact of BMP on *Fgf* expression, from an early supporting to an inhibiting role. Secondly, it allows us to capture the different maximal levels in *Fgf* expression as observed in several mutants, including *Grem1*^{-/-} (figure 3.3C-F). If Bmp acted directly on *Fgf* production, then the model would only reproduce the different timings, as is the case for the AER production rate that directly depends on Bmp signaling (Figure 3.3G, all curves except for early Bmp inactivation reach the same maximal value).

3.4. SHH Dynamics

AER-FGFs induce *Shh* expression (interaction 7) FGF signaling enhances *Shh* expression (interaction 7). In particular, implanting FGF4-loaded beads restores *Shh* expression, which is lost upon removal of the posterior AER in chicken limb buds (Laufer et al., 1994). FGF-loaded beads and *Fgf*-expressing cells induce *Shh* expression in chicken limb buds (Bastida et al., 2009; Ohuchi et al., 1997; Yang and Niswander, 1995; figure 3.4A). In addition, inactivation of FGF receptors in the limb bud mesenchyme reduces *Shh* expression (Revest et al., 2001; Verheyden et al., 2005; figure 3.4B).

Mesenchymal BMP signaling inhibits *Shh* expression (interaction 8) While AER-FGFs enhance *Shh* expression, BMPs inhibit it (interaction 8). Thus *Grem1* knockouts show less *Shh* expression, which can be partially restored by reducing *Bmp4* expression

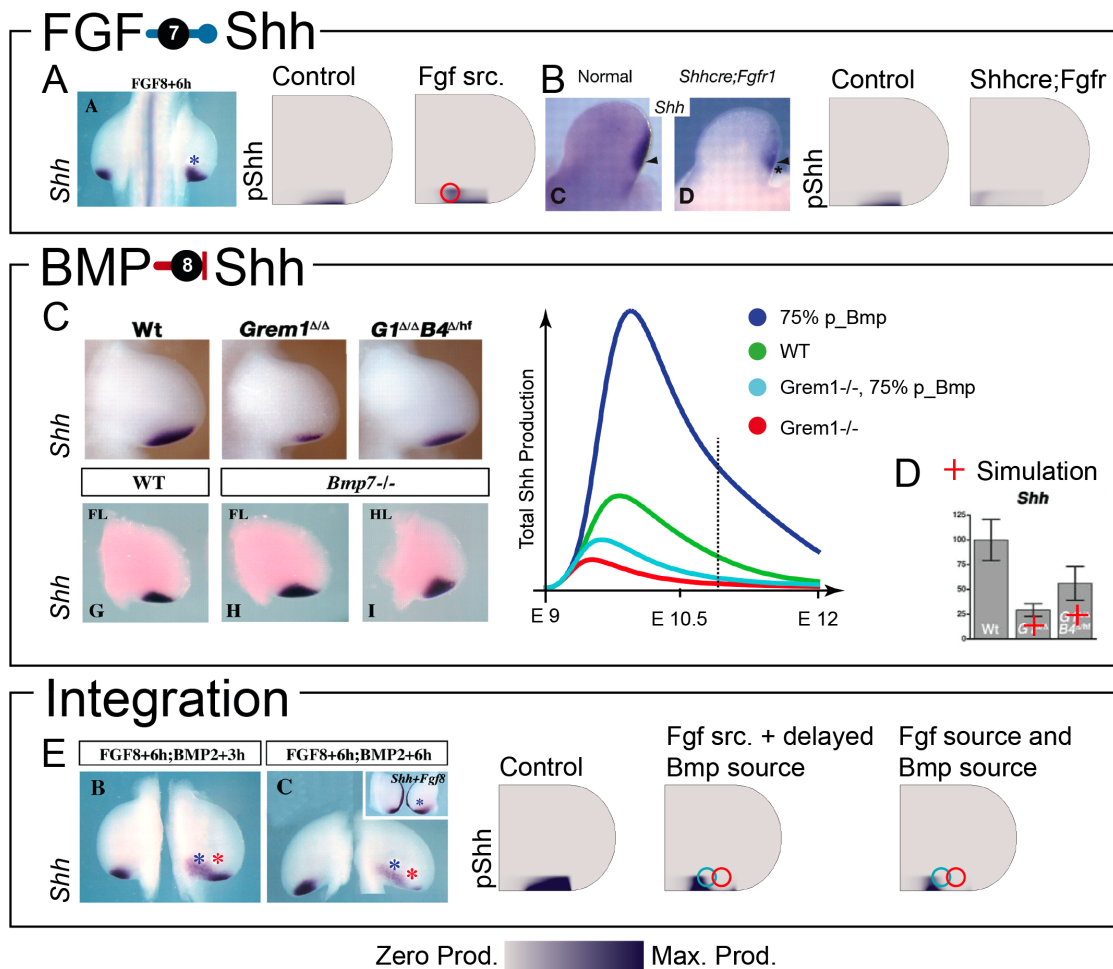


Figure 3.4.: Regulation of *Shh* production. (A, B) FGF signaling induces *Shh*. (A) FGF8 beads induce ectopic *Shh* expression, both in limb cultures (Bastida et al., 2009) and in the simulation. (B) In the absence of FGFR1, *Shh* expression is reduced by E10.75 (Verheyden et al., 2005). The same is observed in simulations; we plot the weak production of Shh hundred times stronger to make it visible. (C) BMP signaling inhibits *Shh* expression. *Grem1* KO mutants with presumably more BMP express less *Shh* which can be partially restored by genetically reducing *Bmp4* expression (Bénazet et al., 2009). In *Bmp7* KO mutants *Shh* expression is up-regulated (Bastida et al., 2009). We simulate the *Bmp* knockouts by reducing the production rate of Bmp to 75% of the wt production rate. Total Shh production represents the integral over the whole domain. (D) BMP beads (red) down-regulate *Shh* expression even in the presence of an additional FGF8 bead (blue) (Bastida et al., 2009). Similarly, in the simulations Bmp inhibits Shh production also in the presence of an additional Fgf source. In the simulated panels the upper limit of the scale has been set below the maximum value of Shh production to enhance visibility of the effect.

(figure 3.4C,D; Bénazet et al., 2009). On the other hand NOGGIN-loaded beads and grafts (Bastida et al., 2009; Zúñiga et al., 1999) up-regulate *Shh* expression and *Shh* is also up-regulated and prolonged in various *Bmp* knockouts (figure 3.4C; Bandyopadhyay et al., 2006; Bastida et al., 2009). This negative effect of BMPs on *Shh* could also be indirect via FGF, but BMP2-loaded beads reduce *Shh* expression, even in the presence of an additional FGF8 source in chicken limb buds (figure 3.4E; Bastida et al., 2009).

Restriction of the Shh producing ZPA A number of transcription factors have been shown to be involved in the restriction of *Shh* expression to the posterior mesenchyme (Capellini et al., 2006; Charité et al., 2000; Galli et al., 2010; Kmita et al., 2005; Knezevic et al., 1997; Lettice et al., 2012; Mao et al., 2009; Nissim et al., 2007; Tarchini et al., 2006; Zhang et al., 2009, 2010; Kozhemyakina et al., 2014). However, little is known to suggest how these transcription factors fit in our regulatory network (figure 3.1A), and we can therefore not include these. We therefore impose a restriction of the production domain of Shh to the posterior in our model, using the function θ_{ZPA} . As Fgf enhances and Bmp limits Shh expression we then have

$$pShh = \rho_{Shh} \cdot \sigma(Fgf) \cdot \bar{\sigma}(Bmp) \cdot \theta_{ZPA}$$

as production term for Shh. θ_{ZPA} is the product of two step functions at $x \leq 0.1$ and $y \leq 0.1$ with a smooth transition zone of 0.05mm (figure 3.1B, green shaded area). Within the posterior domain, the regulatory interactions further restrict Shh expression, and the simulated expression domain of Shh is rather small and diffuse (figure 3.4A). Decreasing the Fgf threshold for Shh activation would expand the domain anteriorly, but would render it even more diffuse. Moreover, a lower threshold would alter both the timing of the initiation and termination of Shh production. Therefore, we are limited in how far we can lower the Fgf response threshold in our model.

The small size of the simulated Shh producing domain makes it more difficult to visually assess the impacts of genetic alterations. We therefore present the Shh production in the ZPA as a graph rather than as a spatial production term (figure 3.4C). The graph reports the total Shh production in the ZPA, i.e. the integral of pShh over the whole domain. An experimental equivalent of such an integral would be the transcript levels measured by qPCR. As can be seen, the simulations reproduce the effects of the genetic alterations in that reduction of Bmp production enhances Shh production (figure 3.4C, blue line; Bastida et al., 2009), while inactivation of *Grem1* reduces Shh production (figure 3.4C, red line; Bénazet et al., 2009). The restoration of Shh expression in *Grem1*^{-/-};*Bmp4*⁻/hf mutant limb buds is also reproduced in the simulation (figure 3.4C, cyan line), though not exactly to the same extent as in the qPCR measurements (figure 3.4D; Bénazet et al., 2009). Due to the double negative impact of Bmp on Shh in our model, i.e. directly and via the AER, changes in Bmp affect Shh more strongly than Fgf in the model, while the effect is similar in *Grem1* and *Bmp*;*Grem1* compound mutant embryos. We choose the relevant parameters such that we underestimate the effect on Fgf (figure 3.3F) and overestimate the effect on Shh (figure 3.4D). Finally, much as in the experiments an extra posterior Bmp source down-regulates Shh expression even in the presence of an additional Fgf source (figure 3.4E; Bastida et al., 2009).

SHH binds to its receptor PTCH1 (interaction 9) SHH forms a multimer (Goetz et al., 2006) and can therefore be expected to bind more than one PTCH1 receptor at a time. To keep the model simple we only consider one type of multimeric interaction, i.e. a bivalent interaction (interaction 9). Using the law of mass action we have for this reversible binding reaction

$$\chi_{\text{PPS}} = k_{\text{PPS}}^+ \cdot \text{Shh} \cdot \text{Ptch1}^2 - k_{\text{PPS}}^- \cdot \text{PPS}$$

Some of the bound receptor will be internalized. The ligand Shh will be degraded, while the receptor Ptch1 can recycle back to the membrane at rate δ_{PPSrec} .

GLI transcription factors transduce SHH signaling (interactions 10, 11) SHH signals through its receptor PTCH1 and the transcription factors GLI1, GLI2 and GLI3 (figure 3.5A). GLI1 contains only the activator domain and is itself a GLI-target (Dai et al., 1999; Vokes et al., 2008), while GLI2 and GLI3 exist in activator and repressor form (Sasaki et al., 1999). Mice lacking *Gli1* appear normal, *Gli2*^{-/-} mutants develop normal limbs, *Gli3*^{-/-} mutants have polydactyly and *Gli* double knockouts show different degrees of malformation (Park et al., 2000). The fact that in *Gli1*^{-/-};*Gli2*^{-/-} double knockout mutants, asymmetric gene expression is still observed in the limb bud (Park et al., 2000) implies that GLI3 alone can mediate SHH signaling in the developing limb bud. Moreover, *Shh*^{-/-};*Gli3*^{-/-} double knockout mutants show a phenotype very similar to *Gli3*^{-/-} mutants (Litingtung et al., 2002; te Welscher et al., 2002b), while mice that lack the GLI3 activator are similar to *Shh* null mice (Cao et al., 2013). Taken together, the data suggests that SHH signaling in the limb bud is mainly transduced by GLI3. For simplicity, we will therefore only consider GLI3 (but not GLI1 and GLI2) in our model. We note, however, that, due to redundancy with GLI1 and GLI2, asymmetric expression of SHH target genes is, also still observed in *Gli3* knockouts (Buescher and Ruether, 1998).

SHH signals by sequestering its receptor PTCH1, thereby preventing PTCH1 from inhibiting SMO (Murone et al., 1999). The transcription factor GLI3 is then no longer cleaved into GLI3R but instead modified to the activator form GLI3A (Hui and Angers, 2011). In the absence of SHH most full length GLI3 is cleaved to its repressor form GLI3R (interaction 10; Wang et al., 2000). Since SMO is an essential, but only an intermediate player in SHH signaling transduction, that is not known to integrate further inputs from other regulatory components in our model, we do not consider SMO explicitly in the model. We model cleavage of full-length Gli3 to the repressor form Gli3r as an irreversible reaction, activated by unbound Ptch1, i.e.

$$\tau_{\text{Gli3r}} = k_{\text{Gli3r}} \cdot \text{Gli3} \cdot \sigma(\text{Ptch1}),$$

and similarly the modification of Gli3 to the activator form Gli3a as an irreversible reaction inhibited by free Ptch1

$$\tau_{\text{Gli3a}} = k_{\text{Gli3a}} \cdot \text{Gli3} \cdot \bar{\sigma}(\text{Ptch1}).$$

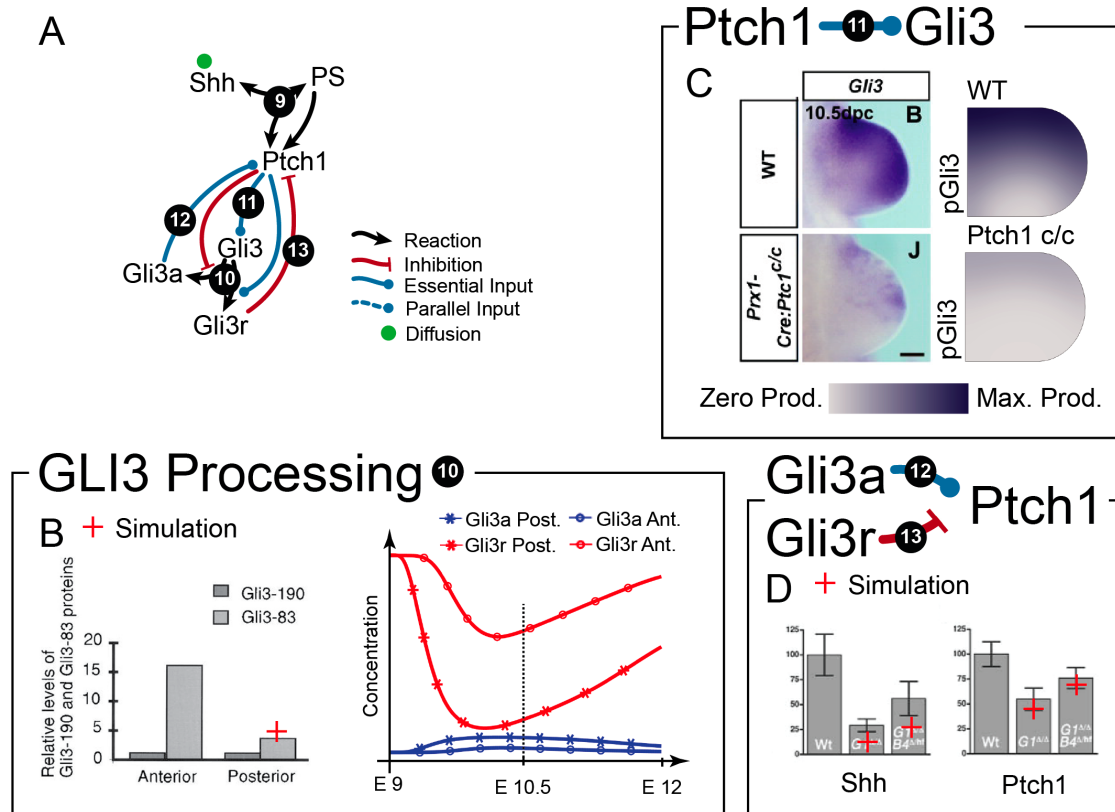


Figure 3.5.: Shh-dependent signaling. (A) The Shh-regulated subnetwork. (B) GLI3 processing. GLI3 proteins are more abundant anteriorly. The GLI3R repressor form (Gli3-83) is more prominent in the anterior part of the limb; the GLI3-190 form is about equally distributed (Wang et al., 2000). The red + sign indicates the predicted effect from the model. The vertical line at E10.5 indicates the time-point in the simulations. (C) Expression of *Gli3* is lost in *Prx1-Cre;Ptch1* mutants, where *Ptch1* is inactivated in the mesenchyme (Butterfield et al., 2009). To make the asymmetry in the remaining pattern visible in the simulations a 2-fold enhanced production rate is plotted in the *Ptch1* mutant. (D) *Shh* and *Ptch1* are down-regulated in mutants lacking its antagonist *Grem1*. Genetically reducing *Bmp4* expression partially restores the expression levels (Bénazet et al., 2009). The red + signs indicate the predicted effects from the model.

The model reproduces the measured distributions of GLI3 and its processed forms (figure 3.5B; Wang et al., 2000).

How *Gli3* expression is controlled has not yet been defined on the molecular level. Before *Shh* expression is activated, *Gli3* expression is progressively restricted to the anterior part of the limb bud, potentially due to mutual repression between GLI3 and HAND2 (Galli et al., 2010; te Welscher et al., 2002a). In addition, over-expression of *Shh* down-regulates *Gli3* expression in the anterior chicken limb bud (Marigo et al., 1996b). *Gli3* expression is not substantially altered in *Gli3* deficient limb buds, but

Gli3 is expressed throughout *Shh* deficient limb buds after the initial stages (Galli et al., 2010; Hill et al., 2009; López-Ríos et al., 2012). Moreover, *Gli3* expression is lowered in limb buds lacking mesenchymal *Ptch1* (figure 3.5C; Butterfield et al., 2009), suggesting that the regulation of *Gli3* expression also depends on PTCH1 (interaction 11). As the underlying regulatory mechanism remains elusive we make Gli3 production positively dependent on the concentration of free Ptch1 for the purpose of modelling, i.e.

$$p\text{Gli3} = \rho_{\text{Gli3}} \cdot \sigma(\text{Ptch1}).$$

With this regulatory interaction included, the model reproduces the *Gli3* expression pattern in wt and *Prx1-Cre;Ptch1* limb buds (figure 3.5C).

Ptch1 is a HH target gene (interactions 12, 13) Finally, *Ptch1* is an established transcription target of SHH signaling in mice (Vokes et al., 2008). We model this as enhancement of Ptch1 production by Gli3a (interaction 12) and repression by Gli3r (interaction 13), i.e.

$$p\text{Ptch1} = \rho_{\text{Ptch1}} \cdot \sigma(\text{Gli3a}) \cdot \bar{\sigma}(\text{Gli3r}).$$

The model predicts similar changes in total Ptch1 production as measured by qPCR of total *Ptch1* transcripts in *Grem1*^{-/-} and *Grem1*^{-/-};*Bmp4*^{-/hf} mutants (figure 3.5D; Bénazet et al., 2009). The model predicts somewhat stronger reductions in Shh production in *Grem1*^{-/-} and *Grem1*^{-/-};*Bmp4*^{-/hf} mutants than observed in the qPCR transcript measurements, but the overall behaviour is captured correctly (figure 3.5D).

3.5. The Regulation of Grem1

GREM1 closes the feedback loop between the AER and the ZPA by integrating signals from all pathways considered in our model, namely BMP, FGF and SHH.

BMPs regulate Grem1 (interactions 14, 15) Implantation of BMP-loaded beads into mouse limb buds up-regulates *Grem1* expression (interaction 14; Bénazet et al., 2009; figure 3.6A). In chicken limb buds, beads soaked in low concentrations of BMP up-regulate *Grem1* expression (Bénazet et al., 2009; Capdevila et al., 1999; Nissim et al., 2006; figure 3.6B), while beads soaked in high BMP concentrations (figure 3.6B) or the BMP antagonist NOGGIN (Capdevila et al., 1999; Nissim et al., 2006) down-regulate *Grem1* expression (interaction 15).

AER-FGFs inhibit Grem1 (interaction 16) Inactivation of AER-*Fgf8* (figure 3.6C) and conditional inactivation of FGF receptors in the mesenchyme results in *Grem1* being expressed closer to the distal AER (interaction 16; figure 3.6 D,E; Verheyden and Sun, 2008; Verheyden et al., 2005). It has previously been suggested that BMPs from the AER may be required to promote ectopic *Grem1*, leading to higher *Grem1* in the distal portion of the *Fgfr*-inactivated domain (Verheyden and Sun, 2008; Verheyden et al., 2005). However, we find that Bmp misregulation (figure 3.2A) is sufficient to reproduce

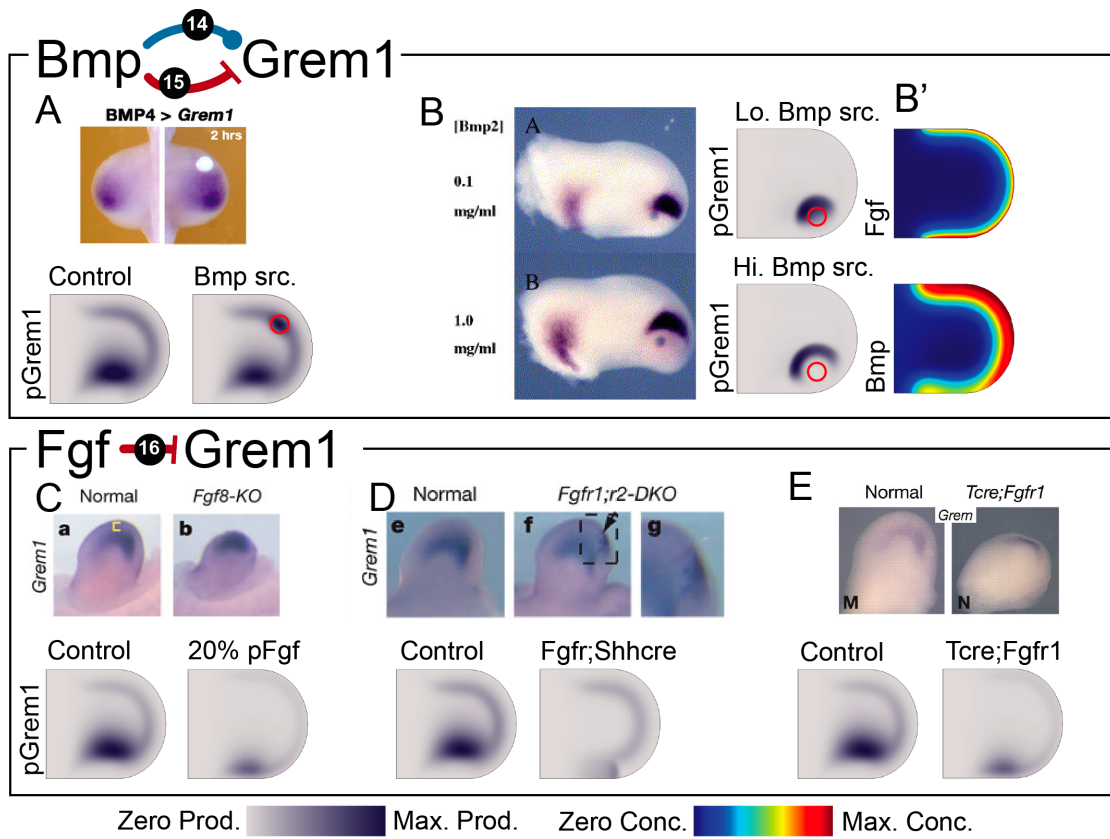


Figure 3.6.: Regulation of *Grem1* by Bmp and Fgf signaling. (A, B) BMP regulates *Grem1*. (A) BMP2 beads up-regulate *Grem1* in mice (top; Bénazet et al., 2009) and in the simulations (bottom). (B) Low BMP2 concentrations induce and high BMP2 concentrations repress *Grem1* in chicken (left; Nissim et al., 2006) and simulations (right). (B') The predicted Fgf and Bmp concentrations are both highest at the AER, and their inhibitory regulations are thus redundant. (C-E) FGF secreted from the AER inhibits *Grem1* expression. (C) *Fgf8* mutants express *Grem1* closer to the AER (top; Verheyden and Sun, 2008). The *Fgf8* mutant was simulated by reducing the Fgf production rate to 20% (bottom). (D) In *Shh-Cre;Fgfr1;2* double knockouts *Grem1* is expressed below the AER by E10.75 (top; Verheyden and Sun, 2008). The conditional inactivation of FGF receptors by *Shh-Cre* was simulated as strong inhibition of all Fgf signaling in Sonic descendants (bottom). We observe more Gli3r in these mutants, and accordingly we have to plot the (much weaker) pGrem on a different scale to make the simulated pattern visible. (E) *Grem1* is expressed closer to the AER upon inactivation of *Fgfr1* in the mesenchyme (top; Verheyden et al., 2005). We simulate this mutant by increasing all Fgf thresholds five-fold (bottom).

the distalization, as the model still reproduces distalization even though we did not include AER-BMPs in our model.

The simulations predict that both Bmp and Fgf concentrations are highest at the distal boundary, i.e. below the AER (figure 3.6B'), and thus that the inhibition of Grem1 production by Bmp is redundant to its inhibition by Fgf. The expanded *Grem1* expression in *Fgf8* deficient and FGF receptor mutant limb buds are thus also obtained in simulations without the negative impact of Bmp on Grem1 production. In fact, we need the negative impact of Bmp on Grem1 production only to reproduce the halo around beads loaded with high Bmp concentration in chicken limb buds (figure 3.6B). While it is in principle also possible that the inhibition of Grem1 by Fgf is indirect via Bmp signaling, we note that we were not able to reproduce the experimental data equally well when we removed the inhibition of Grem1 by Fgf.

SHH induces Grem1 (interactions 17, 18) SHH beads induce *Grem1* in mouse (figure 3.7A), but protein synthesis is required (Bénazet et al., 2009; Nissim et al., 2006). *Grem1* is indeed a direct transcriptional target of GLI in mice limb buds (Vokes et al., 2008; Zúñiga et al., 2012). We implement this regulatory interaction by including a positive impact of Gli3a (interaction 17) and a negative impact of Gli3r (interaction 18) on Grem1 production.

Crosstalk between SHH and BMP dependent Grem1 regulation (interactions 14, 15, 17, 18) In mouse limb buds, *Grem1* remains expressed at lower levels in both, *Shh* and *Smad4* deficient limb buds, but is lost from double mutant limb buds (figure 3.7B; Bénazet et al., 2012; Galli et al., 2010; Nissim et al., 2006). Since SHH-dependent GLI and BMP-dependent SMAD4 signal transduction can both independently induce *Grem1* expression we need to model the positive contributions of Bmp (interaction 14) and Gli3a (interaction 17) in an additive manner. To obtain the posterior bias of *Grem1* expression we have to assume that Gli3r represses the contributions of both Bmp and Gli3a (interaction 18). Additionally, as discussed above, low Bmp levels induce Grem1 (interaction 14), while high Bmp levels (interaction 15) and Fgf (interaction 16) inhibit Grem1 production, i.e.

$$\begin{aligned} p_{\text{Grem1}} = & \rho_{\text{Grem1}} \cdot \bar{\sigma}(\text{Fgf}) \cdot \bar{\sigma}(\text{Gli3r}) \cdot \bar{\sigma}(\text{Bmp}) \\ & \cdot (r_{\text{BG}} \cdot \sigma(\text{Bmp}) + r_{\text{GG}} \cdot \sigma(\text{Gli3a})) \end{aligned}$$

where the constants r_{BG} and r_{GG} set the strength of the respective contributions. We successfully simulate the disruption of SMAD4 mediated canonical BMP signal by removing the activation of Grem1 by Bmp and the Shh deficiency by setting the production rate of Shh to zero (figure 3.7B).

Distal restriction of Grem1 production While the simulations reproduced the experimental manipulations and genetic results (figure 3.6, figure 3.7A,B), they failed to yield the distal restriction of Grem1 expression (Panman et al., 2006; figure 3.7C, compare ISH in panel I and simulated Grem1 expression in panel II). HOXD13 may play an important

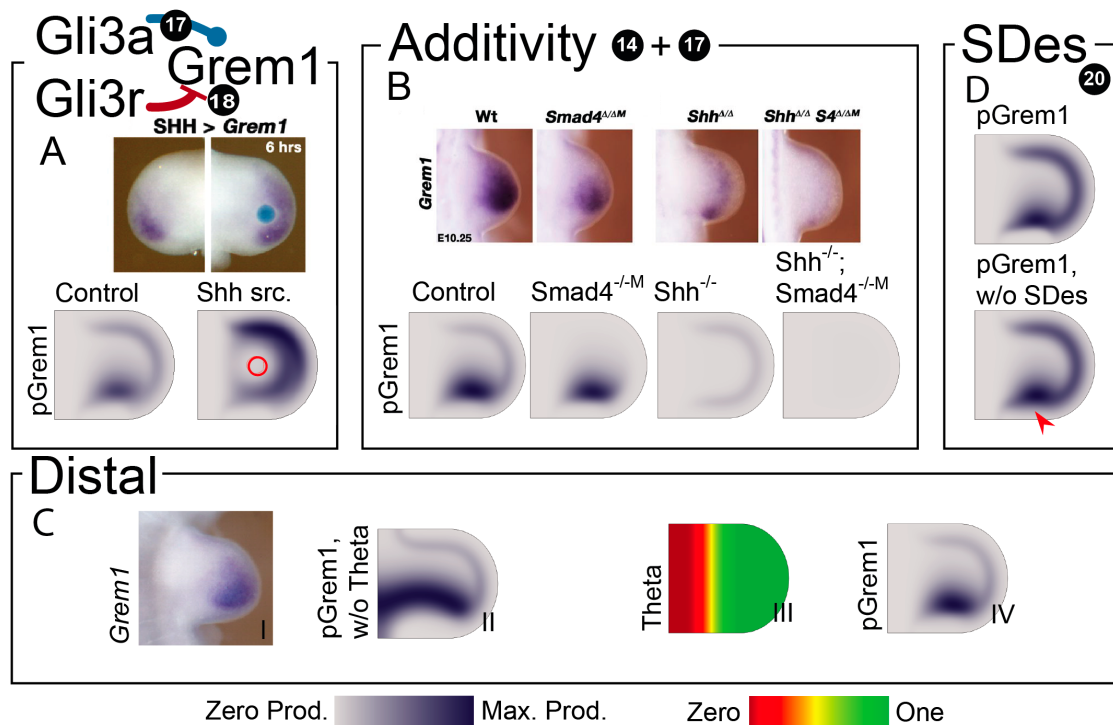


Figure 3.7.: In addition to Bmp signalin, also Shh signaling induces *Grem1*. (A) SHH beads induce *Grem1* in mouse (Bénazet et al., 2009; top), and in the simulations (bottom). (B) GLI3A and BMPs regulate *Grem1* in parallel. *Smad4* and *Shh* knockouts show *Grem1* expression, while *Smad4*;*Shh* double knockouts do not (top; Bénazet et al., 2012). In *Smad4* mutants termination of *Shh* and *Fgf* expression is delayed, but the *Shh* expression pattern does not drastically change at the depicted stage. Inactivation of canonical BMP signaling in *Smad4* mutants mesenchyme is therefore modelled by elevating only the threshold of Bmp on *Grem1* activation (but not the one on *Shh* and *Fgf* production) above the relevant Bmp concentration (bottom). (C) (i) *Grem1* expression is restricted to the distal part of the limb bud (Bénazet et al., 2009). (ii) The distal restriction does not emerge from the network interactions in figure 3.1C. (iii) We restrict *Grem1* production to the distal limb bud by a step function from 0 (red) to 1 (green) with smooth transition. (iv) The simulated *Grem1* pattern. (D) Sonic Descendants (SDes) do not express *Grem1* and thereby create a posterior region devoid of *Grem1* expression (Scherz et al., 2004). Predicted *Grem1* production pattern (top) with SDes, and (bottom) without SDes.

role in biasing *Grem1* expression distally (Chen et al., 2004; Sheth et al., 2013) and FGF signaling and GLI3R are thought to bias *Hoxd13* expression to the handplate (Haramis et al., 1995; Sheth et al., 2013; Verheyden et al., 2005; Zákány et al., 2004). As Gli3r already acts directly on *Grem1* production and we only consider a static AER we decided to impose the distal restriction of *Grem1* expression in our simulations by including a step function θ_{Distal} , which is zero in the proximal and one in the distal part of the limb bud ($x \geq 0.3$) with a smooth transition zone of width 0.4 (figure 3.1B; figure 3.7C, panel III). The regulatory interactions then result in the *Grem1* production rate

$$\begin{aligned} \text{pGrem1} &= \rho_{\text{Grem1}} \cdot \bar{\sigma}(\text{Fgf}) \cdot \bar{\sigma}(\text{Gli3r}) \cdot \bar{\sigma}(\text{Bmp}) \\ &\quad \cdot (r_{\text{BG}} \cdot \sigma(\text{Bmp}) + r_{\text{GG}} \cdot \sigma(\text{Gli3a})) \cdot \theta_{\text{Distal}}. \end{aligned}$$

Upon inclusion of the distal restriction, the simulations (figure 3.7C, panel IV) reproduce many aspects of the experimentally observed *Grem1* transcript distribution (figure 3.7C, panel I). We note that the distal restriction somewhat affected the dynamics in that less *Grem1* production results in less *Bmp* sequestration and less *Shh* production (as expected from experimental analysis).

The Gremlin Gap (interactions 19, 20) Cells expressing *Shh* and their descendants do not express *Grem1* (Scherz et al., 2004). This results in the so-called *Gremlin1*-gap separating the *Shh* and *Grem1* expression domains. We implement these descendants, SDes, as a slowly diffusing species. New SDes emerge by recruitment of cells into the SDes pool as they start to express *Shh*, and by expansion of the *Shh* descendants as a result of cell proliferation. This results in

$$\text{pSDes} = \rho_{\text{SDes}} \cdot (\text{pShh} + \text{SDes})$$

as source of ZPA-descendants. We also need to modify the *Grem1* production rate to take account of the lack of *Grem1* expression in *Shh*-descendants, i.e.

$$\begin{aligned} \text{pGrem1} &= \rho_{\text{Grem1}} \cdot \bar{\sigma}(\text{Fgf}) \cdot \bar{\sigma}(\text{Gli3r}) \cdot \bar{\sigma}(\text{Bmp}) \cdot \bar{\sigma}(\text{SDes}) \\ &\quad \cdot (r_{\text{BG}} \cdot \sigma(\text{Bmp}) + r_{\text{GG}} \cdot \sigma(\text{Gli3a})) \cdot \theta_{\text{Distal}}. \end{aligned}$$

Much as in the embryo, with the Sonic Descendants (SDes) included, we now observe the emergence of a posterior zone in the simulations that does not produce *Grem1* (figure 3.7D).

3.6. Mathematical Formulation

Regulatory Network

The regulatory network (figure 3.1A) is introduced in detail in the sections above. In brief, the signal essential for distal outgrowth of the limb bud are FGFs secreted from the apical ectodermal ridge (AER, cf. figure 3.1B). They induce BMPs in the mesenchyme, which in turn are needed for AER formation at low concentrations, while they inhibit

AER formation at high concentrations. Together FGFs and BMPs control the production of SHH secreted from the posterior margin of the limb bud termed zone of polarizing activity (ZPA, cf. figure 3.1B). SHH is the morphogen for anterior-posterior patterning of the limb bud. In our model SHH binds to its receptor PTCH1 and subsequently signals through the transcription factor GLI3 that is processed into its activator form GLI3A and its repressor form GLI3R. Finally GREM1 integrates the inputs from the FGF, BMP and SHH signaling pathways and antagonizes BMP by sequestering it into an inactive BMP-GREM1-complex.

We implement this regulatory network as reaction diffusion equations of the form

$$\dot{X} = D_X \Delta X + R_X$$

where R_X denotes the reaction terms for concentration X. Activation and inhibition are described by the Hill functions

$$\sigma(X) = \frac{X^2}{X^2 + K^2}$$

and

$$\bar{\sigma}(X) = 1 - \sigma(X) = \frac{K^2}{K^2 + X^2}.$$

The reaction rates that correspond to the network in figure 3.1A are given by

$$\begin{aligned} R_{\text{AER}} &= -\delta_{\text{AER}} \cdot \text{AER} + \text{pAER} \\ R_{\text{Fgf}} &= -\delta_{\text{Fgf}} \cdot \text{Fgf} \\ R_{\text{Bmp}} &= -\delta_{\text{Bmp}} \cdot \text{Bmp} - \kappa_{\text{BG}}^+ \cdot \text{Grem1} \cdot \text{Bmp} + \kappa_{\text{BG}}^- \cdot \text{BG} + \text{pBmp} \\ R_{\text{Grem1}} &= -\delta_{\text{Grem1}} \cdot \text{Grem1} - \kappa_{\text{BG}}^+ \cdot \text{Grem1} \cdot \text{Bmp} + \kappa_{\text{BG}}^- \cdot \text{BG} + \text{pGrem1} \\ R_{\text{BG}} &= -\delta_{\text{BG}} \cdot \text{BG} - \kappa_{\text{BG}}^- \cdot \text{BG} + \kappa_{\text{BG}}^+ \cdot \text{Grem1} \cdot \text{Bmp} \\ R_{\text{Shh}} &= -\delta_{\text{Shh}} \cdot \text{Shh} - \kappa_{\text{PPS}}^+ \cdot \text{Ptch1}^2 \cdot \text{Shh} + \kappa_{\text{PPS}}^- \cdot \text{PPS} + \text{pShh} \\ R_{\text{SDes}} &= -\delta_{\text{SDes}} \cdot \text{SDes} + \text{pSDes} \\ R_{\text{Ptch1}} &= -\delta_{\text{Ptch1}} \cdot \text{Ptch1} - 2\kappa_{\text{PPS}}^+ \cdot \text{Ptch1}^2 \cdot \text{Shh} + 2\kappa_{\text{PPS}}^- \cdot \text{PPS} \\ &\quad + 2\delta_{\text{PPSrec}} \cdot \text{PPS} + \text{pPtch1} \\ R_{\text{PPS}} &= -\delta_{\text{PPS}} \cdot \text{PPS} - \delta_{\text{PPSrec}} \cdot \text{PPS} - \kappa_{\text{PPS}}^- \cdot \text{PPS} + \kappa_{\text{PPS}}^+ \cdot \text{Ptch1}^2 \cdot \text{Shh} \\ R_{\text{Gli3}} &= -\delta_{\text{Gli3}} \cdot \text{Gli3} - k_{\text{Gli3a}} \cdot \text{Gli3} \cdot \bar{\sigma}(\text{Ptch1}) - k_{\text{Gli3r}} \cdot \text{Gli3} \cdot \sigma(\text{Ptch1}) + \text{pGli3} \\ R_{\text{Gli3a}} &= -\delta_{\text{Gli3a}} \cdot \text{Gli3a} + k_{\text{Gli3a}} \cdot \text{Gli3} \cdot \bar{\sigma}(\text{Ptch1}) \\ R_{\text{Gli3r}} &= -\delta_{\text{Gli3r}} \cdot \text{Gli3r} + k_{\text{Gli3r}} \cdot \text{Gli3} \cdot \sigma(\text{Ptch1}). \end{aligned}$$

We calculate the production rates in parallel to compare model predictions to ISH and qPCR data, i.e.

$$\begin{aligned} \text{pAER} &= \rho_{\text{AER}} \cdot \sigma(\text{Bmp}) \cdot \bar{\sigma}(\text{Bmp})|_{\text{AER}} \\ \text{pBmp} &= \rho_{\text{Bmp}} \cdot \sigma(\text{Fgf}) \cdot \bar{\sigma}(\text{Bmp}) + \text{Bmp}_0 \cdot \delta_{\text{Bmp}} \\ \text{pMsx2} &= \sigma(\text{Bmp}) \\ \text{pGrem1} &= \rho_{\text{Grem1}} \cdot \bar{\sigma}(\text{Fgf}) \cdot \bar{\sigma}(\text{Gli3r}) \cdot \bar{\sigma}(\text{Bmp}) \cdot \bar{\sigma}(\text{SDes}) \end{aligned}$$

$$\begin{aligned}
& \cdot (r_{GG} \cdot \sigma(\text{Gli3a}) + r_{BG} \cdot \sigma(\text{Bmp}))|_{\text{DISTAL}} \\
\text{pShh} &= \rho_{\text{Shh}} \cdot \sigma(\text{Fgf}) \cdot \bar{\sigma}(\text{Bmp})|_{\text{ZPA}} \\
\text{pSDes} &= \rho_{\text{SDes}} \cdot (\text{pShh} + \text{SDes}) \\
\text{pPtch1} &= \rho_{\text{Ptch1}} \cdot \bar{\sigma}(\text{Gli3r}) \cdot \sigma(\text{Gli3a}) \\
\text{pGli3} &= \rho_{\text{Gli3}} \cdot \sigma(\text{Ptch1}).
\end{aligned}$$

Here we assume the RNA concentration to be proportional to the expression rate of the corresponding protein. To compare the predicted production rates to quantitative data measured by qPCR we take the integral of the production rate over the domain.

The notation $|_R$ stands for restriction to part R of the geometry as described in the paragraph below and marked in figure 3.1B.

Geometry

The domain is based on a mouse limb bud at embryonic day (E) 10.5 as depicted in figure 3.1B. Sonic Hedgehog (Shh) is only produced in the very posterior region marked as ZPA, restricted by $x \leq 0.5\text{mm}$ and $y \leq 0.1\text{mm}$ with a smooth transition zone of 0.05mm. AER is only solved for on the distal boundary marked AER and restricted to $x \geq 0.2\text{mm}$ with a smooth transition zone of 0.05mm, while Fgf flows in from this boundary, see paragraph below on initial and boundary conditions. Grem1 is only produced in the distal part marked with DISTAL restricted to $x \geq 0.3\text{mm}$ with a smooth transition zone of 0.4mm.

Boundary & Initial Conditions

All fluxes at the boundaries are set to zero, except for Fgf. Fgf represents all FGFs secreted by the apical ectodermal ridge (AER), a specialized epithelium at the distal tip of the limb bud (figure 3.1B). As described above we implement a variable AER on the boundary only and then model the secretion of Fgf by the boundary condition

$$\partial_n \text{Fgf} = \rho_{\text{Fgf}} \cdot \text{AER}$$

where n denotes the normal vector to the boundary.

All initial conditions are zero, with the following exceptions. We initialize the receptor Ptch1 and its regulating transcription factors Gli3, Gli3a and Gli3r at their respective steady state values X_0 in the absence of Shh given in table 3.1. To induce AER formation we initialize Bmp at $\text{Bmp}_0 = K_{\text{AER}}^{\text{Bmp}}/5$.

Parameters

Identification To derive equations and fit their parameters to the data we started by setting up the Bmp-Fgf feedback loop in the absence of Shh signaling. Then we developed a Ptch1-Gli3-module that reproduces the protein quantification experiments when the activity of Shh signaling as measured in Ptch1 up-regulation reaches about half of the domain. Finally we closed the e-m feedback-loop between the AER and the ZPA by

Decay Rates [D^{-1}]		Production Rates		Hill Constants K			
δ_{AER}	$0.5^{+64\%}_{-29\%}$	ρ_{AER}	$24^{+15\%}_{-13\%}$	$K_{\text{Bmp}}^{\text{Fgf}}$	$0.0625^{+8.2\%}_{-8.4\%}$	$K_{\text{Msx2}}^{\text{Bmp}}$	$K_{\text{Grem1}}^{\text{Bmp}}$
δ_{Fgf}	$4^{+31\%}_{-36\%}$	ρ_{Fgf}	$0.1764^{+15\%}_{-13\%}$	$K_{\text{Shh}}^{\text{Fgf}}$	$5^{+3.5\%}_{-3.5\%}$	K^{Ptch1}	$0.001^{+5.3\%}_{-4.4\%}$
δ_{Grem1}	$0.2^{347\%}_{-100\%}$	ρ_{Grem1}	$0.042^{+5.7\%}_{-6.0\%}$	$\bar{K}_{\text{Grem1}}^{\text{Fgf}}$	$0.125^{+12\%}_{-11\%}$	\bar{K}^{Ptch1}	$0.00005^{+3.3\%}_{-3.7\%}$
δ_{Bmp}	$0.2^{+49\%}_{-63\%}$	ρ_{Bmp}	$0.0\bar{1}^{+2.7\%}_{-2.5\%}$	$K_{\text{Grem1}}^{\text{Bmp}}$	$0.01^{+60\%}_{-22\%}$	$K_{\text{Gli3a}}^{\text{Gli3a}}$	$1^{+64\%}_{-60\%}$
δ_{BG}	$0.2-100\%$	ρ_{Shh}	$8440^{+7.4\%}_{-6.7\%}$	$\bar{K}_{\text{Grem1}}^{\text{Bmp}}$	$0.1-99\%$	$\bar{K}_{\text{Ptch1}}^{\text{Gli3r}}$	$20^{+26\%}_{-17\%}$
δ_{Shh}	$8^{+48\%}_{-41\%}$	ρ_{SDes}	$3^{+33\%}_{-27\%}$	$K_{\text{AER}}^{\text{Bmp}}$	$0.0015^{+25\%}_{-20\%}$	$K_{\text{Grem1}}^{\text{Gli3a}}$	$10^{+4.1\%}_{-3.5\%}$
$\delta_{\text{SDes}}^{1)}$	0	ρ_{Ptch1}	$0.01^{+25\%}_{-26\%}$	$\bar{K}_{\text{AER}}^{\text{Bmp}}$	$0.001^{+9.0\%}_{-8.4\%}$	$\bar{K}_{\text{Grem1}}^{\text{Gli3r}}$	$20^{+30\%}_{-22\%}$
δ_{Ptch1}^*	$1.2^{+65\%}_{-74\%}$	ρ_{Gli3}	$2600^{+3.7\%}_{-4.1\%}$	$\bar{K}_{\text{Shh}}^{\text{Bmp}}$	$0.0003^{+4.1\%}_{-3.8\%}$	$\bar{K}_{\text{Grem1}}^{\text{SDes}}$	$0.0075^{+1250\%}_{-98\%}$
δ_{PPS}	$4-100\%$	k_{Gli3a}	$5000^{+6.6\%}_{-7.1\%}$	$\bar{K}_{\text{Bmp}}^{\text{Bmp}}$	$0.02-38\%$		
δ_{PPSrec}	$0.2^{+1550\%}_{-100\%}$	k_{Gli3r}	$6000^{+7.6\%}_{-6.2\%}$				
δ_{Gli3}	$4^{+681\%}_{-100\%}$	r_{BG}	$5^{+64\%}_{-60\%}$				
δ_{Gli3a}	$10^{+5.5\%}_{-4.5\%}$	r_{GG}	$2^{+6.3\%}_{-6.5\%}$				
δ_{Gli3r}	$20^{+169\%}_{-50\%}$	r_{Bmp0}	$0.0054^{+205\%}_{-100\%}$				
Complex Formation		Diffusion [mm^2/D]				Initial Conditions	
κ_{BG}^+	$10'000^{+56\%}_{-27\%}$	D_{Fgf}	$0.012^{+12\%}_{-10\%}$	D_{BG}	$0.005-100\%$	Ptch1 ₀	0.0008
$\kappa_{\text{BG}}^{-2)}$	0	D_{Grem1}	$0.04^{+73\%}_{-40\%}$	D_{Shh}	$0.12^{+125\%}_{-43\%}$	Gli3 ₀	0.4294
κ_{PPS}^+	$7'143'000^{+56\%}_{-20\%}$	D_{Bmp}	$0.005^{+28\%}_{-26\%}$	D_{SDes}	$0.0006-100\%$	Gli3a ₀	0.7861
κ_{PPS}^-	$1^{+328\%}_{-100\%}$					Gli3 ₀	52.152
						Bmp ₀	$K_{\text{AER}}^{\text{Bmp}}/5^{+19\%}_{-16\%}$

Table 3.1.: Kinetic Parameters, non-vanishing diffusion constants and non-zero initial conditions. Here K_X^A denotes the Hill constant of activation of X by an activator A and \bar{K}_X^I the Hill constant of inhibition of X by an inhibitor I. Units of time and length are days and millimeters respectively; concentrations are arbitrary. The upper bounds for the zero parameters are $1.36^{1)}$ and $1.28^{2)}$.

tuning our model to reproduce the quantitative effects on Shh and Fgf production in the Grem1 knockout. The dynamics of the other mutants and the bead experiments emerged naturally.

The parameters are summarized in table 3.1. Simulation time represents the time from embryonic day E9 to E12 and all lengths are given in mm; the units of the concentrations remain arbitrary as no concentration measurements are available. Thus we can only compare half-lives and diffusion rates to experimentally established values (Yu et al., 2009; Müller et al., 2013; Kicheva et al., 2007; Wen et al., 2010; Harfe et al., 2004), c.f.

Half-lives [h]			Diffusion rates [$\mu\text{m}^2/\text{s}$]		
τ_{AER}	33		D_{Fgf}	0.14	1.6 ... 53
τ_{Fgf}	4.2	~ 0.15	D_{Bmp}	0.06	0.1 ± 0.05
τ_{Bmp}	83	0.76 ± 0.39	D_{Grem1}	0.46	
τ_{Grem1}	83		D_{BG}	0.06	
τ_{BG}	83		D_{Shh}	1.4	
τ_{Shh}	2.1		D_{SDes}	$6.9 \cdot 10^{-3}$	
τ_{Ptch1}	14				
τ_{PPS}	4.2				
τ_{PPSrec}	83				
τ_{Gli3}	4.2	~ 2			
τ_{Gli3a}	1.7				
τ_{Gli3r}	0.83	~ 4			

Table 3.2.: Half-lives and diffusion constants in hours and $\mu\text{m}^2/\text{s}$ respectively and comparable values experimentally established in Yu et al. (2009); Müller et al. (2013); Kicheva et al. (2007); Wen et al. (2010); Harfe et al. (2004).

table 3.2.

Justification Some of the protein half-lives are longer than previously measured, possibly because we do not consider translation or transcription. Moreover many variables do not only represent the protein, but also the whole signaling pathway. The comparably small diffusion rates for Fgf and Bmp might be due to the missing sequestration by receptors. The GLI3 half lives have been measured for activation by SHH and for deactivation, the latter kinetics being substantially faster (Harfe et al., 2004).

Given that we state that low levels of Bmp induce and high levels of Bmp inhibit AER formation it might be confusing that the threshold for activation is actually greater than the threshold of inhibition, i.e. $K_{\text{AER}}^{\text{Bmp}} > \bar{K}_{\text{AER}}^{\text{Bmp}}$. However the product of the two Hill functions, $\sigma(\text{Bmp}) \cdot \bar{\sigma}(\text{Bmp})$, still encodes the activation by low levels and inhibition at high levels.

Sensitivity To assess the sensitivities of the different parameters, we developed the following criteria, which quantify the main criteria we attempted to match in the manual optimization of the model: the peak total production rate of Shh should occur between E9.5 and E10.5 (figure 3.8A, marked in black), the peak should not differ more than 10% from the standard model (figure 3.8A, red curve) as this ensures that Shh signaling activity reaches about half of the limb domain, and the final Shh production rate at E12

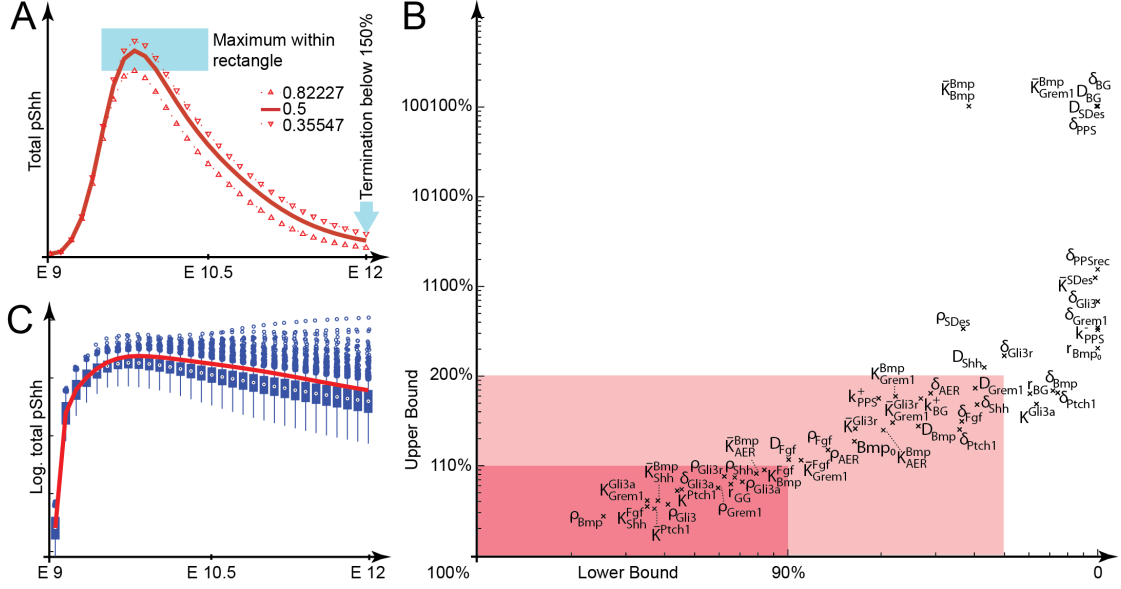


Figure 3.8.: Sensitivity analysis. (A) The total Shh production in the standard model and for the lower (marked by ∇) and the upper bound (marked by \triangle) for δ_{AER} . The criteria for these bounds are marked in blue. (B) The upper bounds versus the lower bounds of all parameter values plotted on a log-log-scale. 100% corresponds to the wild-type condition in table 3.1. (C) The median (central mark) and the 25th and 75th percentile (bold bar) of the total Shh production for thousand samples of either upper or lower bounds for every parameter on a log-lin-scale. Circles denote outliers and the wild-type simulation is overlaid in red.

should be at most maximal 50% higher than in the standard model (figure 3.8A, marked in black). Changes within these limits are barely visible to the eye. Then we searched for each parameters lower and upper bound, satisfying these criteria by binary search within the interval from zero to 1023 times the parameter value.

Interestingly, for the decay rate δ_{Gli3r} both bounds lead to a lowering of the total production, otherwise the two boundary cases are on opposite sides of the production in the standard model. As we expected, the most sensitive parameters were all closely related to the e-m feedback-loop. Thus, the most sensitive parameter is the production rate ρ_{Bmp} , which can be varied about 2.5% such that the solution still matches the criteria stated above, followed by the Hill constants $K_{\text{Shh}}^{\text{Fgf}}$ ($\sim 3.5\%$) and $K_{\text{Grem1}}^{\text{Gli3a}}$ ($\sim 3.5\%$). On the other side, parameters associated with the BG-complex are the least sensitive as we set its rate of unbinding k_{BG}^- to zero. All other bounds are given table 3.1 and plotted figure 3.8B. 74% and 131% are the medians for the lower and upper bound respectively. 15 out of the 50 parameter values can only be varied by 10% and 19 at least two-folds.

We analyzed the combined effects of parameter perturbations by drawing thousand samples of the lower and upper bounds identified above for each parameter with equal probability (figure 3.8C, boxplots). The trend towards lower Shh production probably

Experiment	ρ_{Source}	(x_0, y_0)	t_0	t_r
Bmp inhibits Bmp	$\rho_{Bmp} \cdot 5$	(0.4, 0.1)	9.75	9.875
Grem1 induces Bmp	ρ_{Grem1}	(0.4, 0.1)	9.75	9.875
Fgf induces Shh	ρ_{Fgf}	(0.25, 0.075)	9.75	10
Bmp inhibits Shh in the presence of Fgf (t_0 for delayed Bmp source)	ρ_{Fgf} ρ_{Bmp}	(0.3, 0.1) (0.4, 0.1)	9.75 9.875	10
Bmp induces Grem1 in the anterior	$\rho_{Bmp}/10$	(0.6, 0.55)	10.5	10.58
Low Bmp induces Grem1 in the post.	$\rho_{Bmp} \cdot 5$	(0.5, 0.1)	9.75	9.875
High Bmp induces Grem1 in the post.	$\rho_{Bmp} \cdot 50$	(0.5, 0.1)	9.75	9.875
Shh induces Grem1	$\rho_{Shh}/50000$	(0.4, 0.375)	10.5	10.75

Table 3.3.: Secretion rates ρ_{Source} , positions (x_0, y_0) in [mm], times of placement t_0 [E] and times of read out t_r [E] used to simulate bead experiments.

reflecting the 18 parameters where we only found the bound resulting in the lowest tolerated production within the range we screened, e.g. because setting the parameter to zero results only in slightly higher production or because the production rate did not fulfill the criterion at termination.

Simulating Beads and Mutations

To simulate a bead of species X at (x_0, y_0) we add a gaussian source, i.e.

$$R_{Source} = \rho_{Source} \cdot \theta(t - t_0) \cdot e^{-((x-x_0)^2+(y-y_0)^2)/r^2},$$

to the corresponding reaction term R_X . θ is a smooth transition function turning the source on at time t_0 and we use $r = 0.05\text{mm}$. Secretion rates ρ_{Source} and positions (x_0, y_0) used in the figures are summarized in table 3.3.

We simulate knockouts of the species X included in our simulation (i.e. $Grem1^{\Delta/\Delta}$, $Grem1^{\Delta/\Delta}; Bmp4^{\Delta/hf}$, $Fgf8^{\Delta/\Delta}$ and $Shh^{\Delta/\Delta}$) by reducing the corresponding production rate ρ_X to zero or the indicated value from the beginning of the simulation or in the case of the conditional knockout $Prx1-Cre;Ptch1$ after initialization of Ptch1, Gli3, Gli3a and Gli3r at steady state.

To simulate mutations in intermediate species involved in signaling cascades but not considered explicitly in the simulations we change the affected regulations. Thus we simulate $Shh-Cre;Fgfr1;r2$ mutants by extending activation by Fgf to

$$\sigma(\text{Fgf}, \text{SDes}) = \frac{(\text{Fgf}/K^{\text{Fgf}})^2}{(\text{Fgf}/K^{\text{Fgf}})^2 + (\text{SDes}/\bar{K}_{\text{Fgfr}}^{\text{SDes}})^2 + 1}$$

with $\bar{K}_{\text{Fgfr}}^{\text{SDes}} = \bar{K}_{\text{Grem1}}^{\text{SDes}}/500$ and using $1 - \sigma(\text{Fgf}, \text{SDes})$ for inhibition by Fgf. To simulate $Tcre;Fgfr1$ mutants we multiply the Hill constants $K_{\text{Bmp}}^{\text{Fgf}}$, $K_{\text{Shh}}^{\text{Fgf}}$ and $\bar{K}_{\text{Grem1}}^{\text{Fgf}}$ by 5.

Finally we simulate the $Smad4^{\Delta/\Delta M}$ mutant by elevating the Hill constant K_{Grem1}^{Bmp} above the relevant Bmp concentrations.

To produce a simulation without desensitization to Shh we add a small constitutive production term $p_{Gli3}^0 = 0.05$ to $pGli3$, scale the production rate as $\rho_{Gli3} \cdot Gli3_0 / (Gli3_0 + p_{Gli3}^0)$ to keep the same steady state level and divide ρ_{Grem1} by 2.55 to compensate for the higher Shh activity.

4. Self-regulated Dynamics Emerge from the Core Regulatory Network

This chapter is adapted from a draft submitted to *Development* as **Germann, P. and Iber, D.** A Data-based Computational Model for the Epithelial-Mesenchymal SHH/BMP/GREM1/FGF Feedback Loop in Limb Bud Development.

4.1. Spatio-temporal Dynamics of the Regulatory Interactions in the Developing Limb Bud

The model was constructed using static rather than dynamic data, as the experimental analysis is typically carried out at discrete time points in separate embryos; movies with temporal kinetics of gene expression patterns are not available. However, the validated model can now be used to explore the spatio-temporal evolution of key regulatory interactions in the limb bud.

We demonstrate this by example of the spatio-temporal regulation of *Grem1* production (figure 4.1A), which is controlled by *Bmp* (arrows 14,15), *Fgf* (arrow 16), and *Shh* signaling (arrows 17,18,20; figure 4.1B). In biological network cartoons, time-dependent differences are often depicted by adding or removing arrows in the network cartoon. In our network, arrows indicate that a regulatory interaction is possible, in principle. Whether this regulatory interaction is active and how strong it is depends on the local concentration of the regulatory component, and these concentrations evolve in time and space, while the general regulatory potential remains.

The simulations show how the spatio-temporal concentration patterns evolve over time. Thus, *Bmp* and *Fgf* assume their highest concentration (figure 4.1C, first two rows) and thus highest activity (figure 4.1D) close to the AER and this activity increases over time (figure 4.1D, compare left and right column). *Gli3a* is concentrated mainly in the posterior part of the limb bud, while *Gli3r* is concentrated mainly in the anterior part of the limb bud (figure 4.1C, 3rd and 4th rows). The concentration profile (and thus the activity) evolves over time in that *Gli3a* and *Gli3r* first move to the anterior and then move back towards the posterior side (figure 4.1D, compare left and right column). Finally *Sonic Descendants* develop over time and spread out from the ZPA (figure 4.1C,D, last row).

As previously discussed, the two positive effects on *Grem1* production, *Bmp* and *Gli3a*, impact independently. *Bmp* is present mainly close to the AER (figure 4.1B,C, 2nd row), while *Gli3a* is active mainly in the posterior part of the limb bud (figure 4.1B,C, 3rd row). In the model, the posterior production of *Grem1* is mainly induced by *Gli3a* (figure 4.1E)

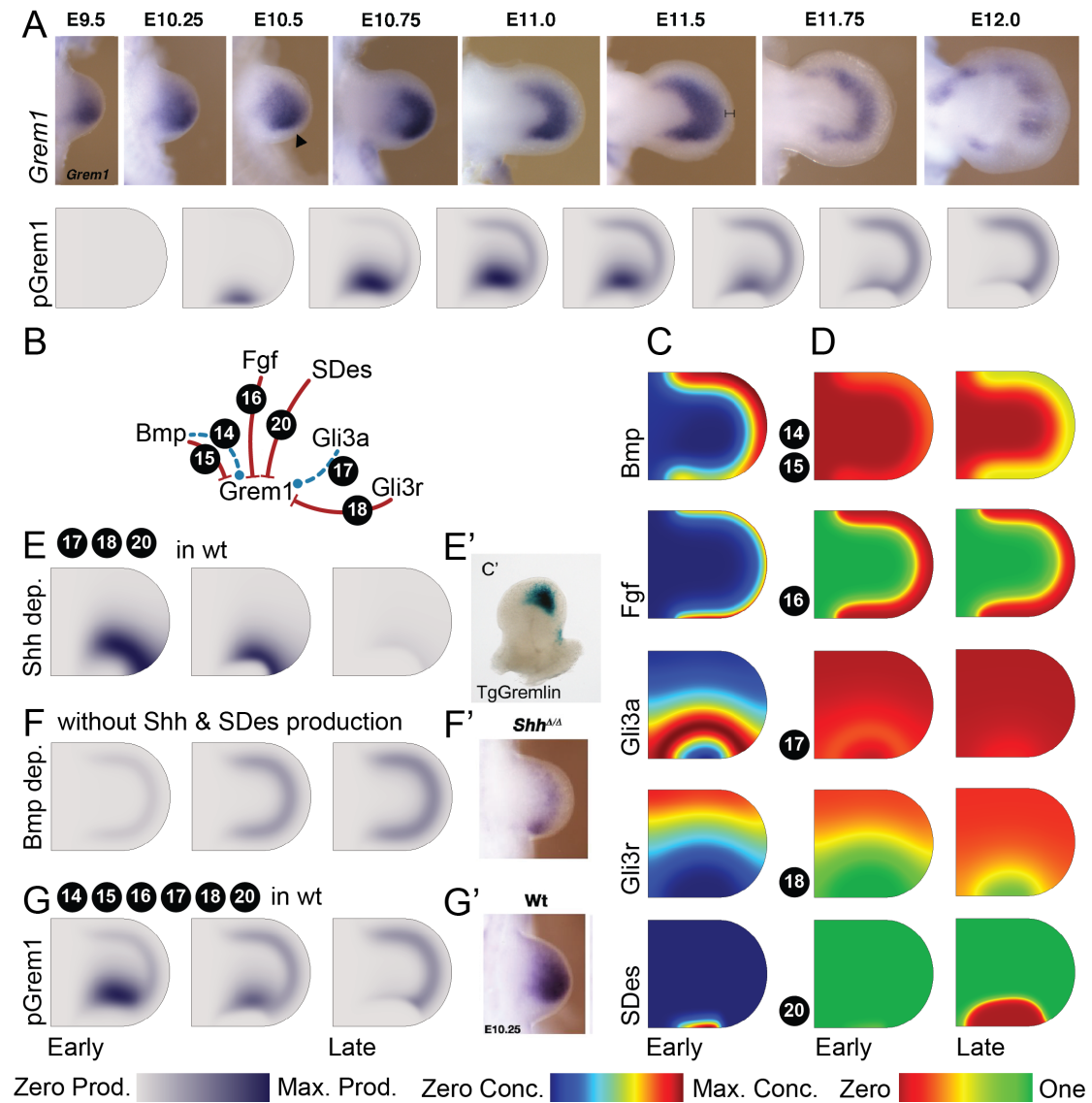


Figure 4.1.: Spatio-temporal Dynamics of the regulation of *Grem1* production. (A) ISH of *Grem1* during mouse limb bud development (Zúñiga et al., 2012; top), and simulated spatial distribution of *Grem1* production levels over time (bottom). (B) Sub-network that directly regulates *Grem1* production in the model. (C) Levels of the variables that regulate *Grem1* production at an early stage. (D) Spatio-temporal activities of the variables that regulate *Grem1* production at an early and late stage. (E-G) Time courses of (E) the Shh-dependent term, (F) the Bmp-dependent term in a model without Shh production, and (G) the total *Grem1* production in our model reveal the relative spatial contributions of the different regulatory inputs to the regulation of *Grem1* production. The experimental data for comparison on the right show (E') the transcript expression under control of the *Grem1* GLI-binding-region (Vokes et al., 2008), (F') an ISH image of *Grem1* expression in the *Shh* null mutant (Bénazet et al., 2009), and (G') *Grem1* expression in the wt (Vokes et al., 2008).

and the Gli3a-dependent Grem1 production pattern (figure 4.1E) is similar to the one observed with a GLI-binding region (GBR) from the *Grem1* enhancer (figure 4.1E'; Vokes et al., 2008; Zúñiga et al., 2012). The production of Grem1 close to the AER, on the other hand, is mainly induced by Bmp-dependent signaling (figure 4.1F), as also seen in *Shh* null embryos (Bénazet et al., 2012; figure 4.1F'). Both, in the simulations (figure 4.1C,D, 3rd and 4th row) and in the embryo (Zúñiga et al., 2012), the Gli3r/Gli3a concentration and activity profile shifts to the anterior side over time, and so does the total Grem1 production zone (figure 4.1A,G). The other regulatory factors all have negative impacts and further restrict the Grem1 production domain. Thus the lack of Grem1 production close to the ZPA is due to the emergence of Sonic Descendants, which do not produce Grem1 (figure 4.1C,D, last row, figure 4.1G), and the gap between the AER and the Grem1 production zone is due to the negative impact of Fgf on Grem1 production (figure 4.1G).

4.2. Dynamics of *Shh* Expression Emerge From the Network Interactions

Much as in the embryo, the regulatory interactions in our model first up-regulate and then down-regulate Shh production (pShh in figure 4.2A, red line). In the following, we will explore, how the different interactions contribute. To this end, we are plotting the rate of AER formation (pAER, blue line), the rate of Fgf production (pFgf, green line) and the Bmp concentration (Bmp, cyan line) at one point in the posterior part of the limb bud (figure 4.2B, cartoon) over developmental time (figure 4.2A). Since the domain of Shh production changes over time, we plot the total rate of Shh production in the entire limb bud (figure 4.2A, red line).

Initially, we start the simulations without AER or Fgf and start the simulation with a low level of Bmp to induce the formation of the AER (figure 3.1A, interaction 5). The AER then secretes Fgf (figure 3.1A, interaction 1), which induces both the production of Shh (figure 3.1B, interaction 7) in the posterior part of the limb bud and which engages in a positive feedback with Bmp by enhancing its production (figure 3.1B, interactions 2, 5 & 1). This process has been termed initiation phase (figure 4.2A, B, event 1).

As the concentration of Bmp increases, Bmp induces less AER formation (figure 3.1A, arrow 6; figure 4.2A, B, event 2). However the AER abundance and thus the Fgf production rate are still increasing. At the same time Shh supports the production of Grem1 in the posterior part of the limb bud via its impact on Gli3 processing (figure 3.1A, arrows 9-13). Grem1 binds Bmp and sequesters it in an inactive complex BG (figure 3.1A, arrow 4), thus slowing down the accumulation of free, active Bmp, in particular in the posterior part of the limb bud (figure 4.2A, B, event 3). The epithelial-mesenchymal feedback between the AER and the ZPA is now maximally active, a phase referred to as Propagation (figure 4.2B).

As Bmp interferes with the Fgf-dependent induction of Shh production (figure 3.1B, arrow 8) the rise of Bmp leads at a certain level to down-regulation of Shh production (figure 4.2A, B, event 4). This process further accelerates as the Bmp concentration

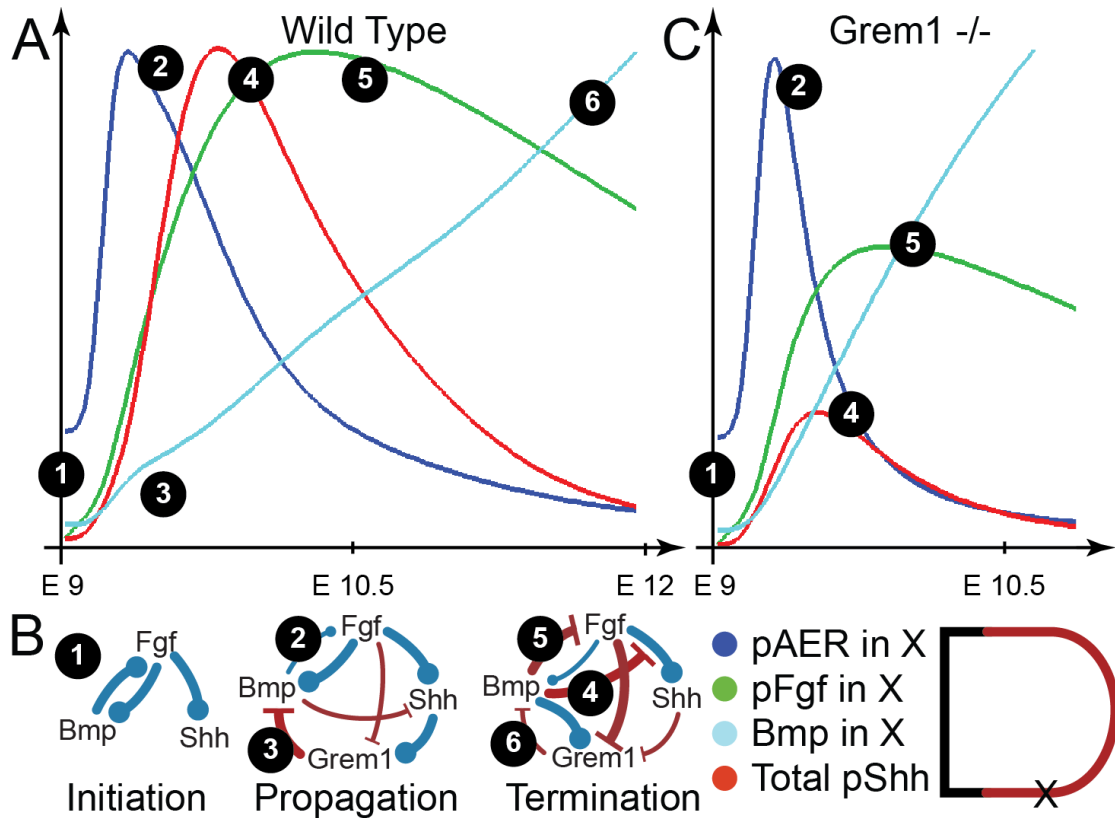


Figure 4.2.: The mechanistic Basis of Shh Termination. (A) The AER formation rate (blue curve), Fgf production rate (green curve) and the Bmp signaling levels (cyan curve) in the point X of the boundary near the ZPA and the total Shh production (red curve). (B) Cartoons of the stages of limb development as proposed in (Zeller et al., 2009) based on the events predicted by our model. Number link these events in the graph in A to the arrows in the cartoons in B. (C) The same plot as in A without Grem1 production.

reaches levels that result in a declining of AER abundance (figure 4.2A, B, event 5), of Fgf production and of Shh induction. With the appearance of the so-called Gremlin-gap between the domains of Shh production and Grem1 production, that is due to the inhibition by Fgf and the inability to express Grem1 by the Sonic descendants Bmp levels rise unhindered close to the AER and the ZPA, heralding the phase of termination (figure 4.2A, B, event 6).

Grem1 closes the feedback-loop between the AER (Fgf pathway) and the ZPA (Shh pathway) by integrating inputs of all three pathways (Bmp, Fgf and Shh) in our model. Its importance is best illustrated by studying a Grem1 mutant (figure 4.2C). Without Grem1 production, Bmp levels rise unhindered (figure 4.2C), thus shortening the propagation phase drastically (compare figures 4.2A and 4.2C). The rate of AER formation still reaches the same maximum (figure 4.2A,C blue curves), but in the Grem1 mutant the Bmp signaling levels increase faster, and thus quickly exceed the concentration range

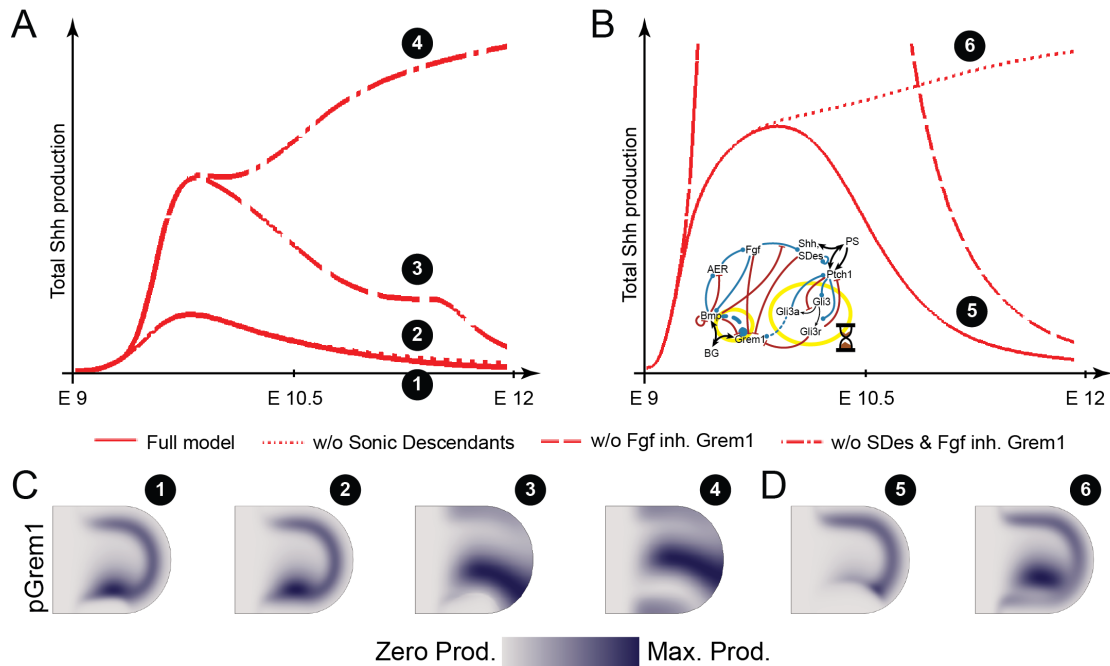


Figure 4.3.: The role of the FGF-Gremlin interaction in Shh termination and the Sonic Descendants & The Gremlin Gap. (A) Time course of the concentrations and the contributions of the Grem1 regulators. (C) The total production of Shh in a simulation with (solid line) and without (dotted line) Sonic descendants. (D) Making the Bmp contribution to Grem1 (seven times) stronger and slowing down the Gli3 module (by multiplying decay, production and processing rates by ten) changes the role of SDes drastically. In such a scenario termination is only due to SDes. The effects of SDes in patterning in both scenarios.

that promotes AER formation. As a consequence less AER and thus less Fgf are produced (figure 4.2A,C green curves). Low Fgf and high Bmp levels limit the Shh production, as also observed in *Grem1* null embryos (Bénazet et al., 2009).

4.3. The Gremlin Gap Terminates the Production of Shh

Expression of *Shh* ceases around E12 both in the model (figure 4.2A) and in the embryo. It has been suggested that termination is mainly controlled by AER-FGFs that down-regulate *Grem1* expression (Verheyden and Sun, 2008), and by Sonic descendants that do not express *Grem1* (Scherz et al., 2004). We can now use the model to explore the regulation of the Shh production kinetics and the relative impact of these proposed regulatory interactions (c.f section §4.1) on termination.

Whether or not Sonic descendants are important for termination depends on how we choose the parameter values. Thus in the standard model, termination of Shh expression

Parameter	Factor
r_{BG}	7
$\rho_{Gli3}, \rho_{Gli3a}, \rho_{Gli3r}, \delta_{Gli3}, \delta_{Gli3a}, \delta_{Gli3r}$	10
ρ_{Shh}	1.3 $\bar{3}$
ρ_{SDes}	0.6 $\bar{6}$

Table 4.1.: The changed parameters and the respective factors for the alternative parametrization with the slow Gli3-module and stronger activation of Grem1 by Bmp.

is observed also in the absence of Sonic descendants (figure 4.3A). However, if we re-adjust our parameter values such that the contribution of Bmp to the control of Grem1 production is stronger (relative to the impact of Shh/Gli3a) and the kinetics of the Gli3-module become slower (c.f. table 4.1), then Shh production no longer terminates without Sonic descendants (figure 4.3B). While the latter version of the model does not reproduce the data from the mouse forelimb as well as the standard model (figure 4.3C,D), we cannot exclude that there exists yet a different parameter set that does. Also, other species and the mouse hindlimb may correspond to a setting in which Sonic descendants are important. In the mouse hindlimb, the transcription factor TBX2 has recently been shown to prevent *Grem1* expression in Sonic descendants. Removal of the transcription factor extends the *Grem1* expression posteriorly and prolongs *Shh* expression (Farin et al., 2013).

5. Robustness to SHH Signaling

This chapter is adapted from a draft submitted to *Development* as **Germann, P. and Iber, D.** A Data-based Computational Model for the Epithelial-Mesenchymal SHH/BMP/GREM1/FGF Feedback Loop in Limb Bud Development.

5.1. Depletion of Full-length GLI3 Provides a Mechanism for Desensitization to SHH

Cells in the very posterior margin of the developing limb bud lose sensitivity to SHH at later stages. Our model suggests that this observed desensitization of the *Ptch1*/*Gli3* genes to SHH (figure 5.1A; Dessaud et al., 2007) is the result of rapid GLI3 turnover (cf. figure 5.1B for the relevant subnetwork). Briefly, in the very posterior margin of the domain that has been exposed to Shh signaling for the longest period of time, lack of free Ptch1 receptor results in less Gli3 production. Gli3 is highly unstable and because of rapid loss of Gli3 (figure 5.1C, green line), the activator form Gli3a can no longer be produced (figure 5.1C, blue line), leading to the desensitization, i.e. strongly reduced Ptch1 production (figure 5.1C, black line), even though the repressor form Gli3r is absent in the posterior part (figure 5.1C, red line).

To prove that desensitization results from depletion of Gli3 in our model we add a small constitutive Gli3 production rate of about 7% of the steady state production rate

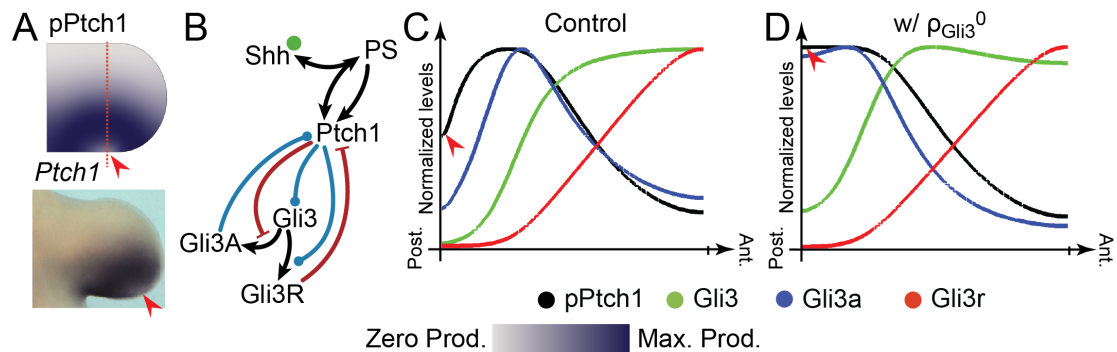


Figure 5.1.: Emergence of desensitization to SHH from the network context. (A) Desensitization to Shh at E10.25 on the two-dimensional domain and in an E10.5 limb bud (Li et al., 2006). (B) The relevant subnetwork. (C) The Ptch1 production term and the Gli3, Gli3a and Gli3r levels on the cut marked by the dotted red line in A. (D) A small constitutive production rate for Gli3 prevents desensitization.

Experiment	ρ_{Source}	(x_0, y_0)	t_0	t_r
Shh inhibits itself	$\rho_{Shh}/50000$	(0.4, 0.1)	9.75	10.75

Table 5.1.: Secretion rate ρ_{Source} , position (x_0, y_0) in [mm], time of placement t_0 [E] and time of read out t_r [E] used to simulate the SHH bead experiment. For details of the used equations see section §3.6.

in the absence of Shh, while keeping the total production the same. In such a model a small amount of Gli3 is produced at all times, preventing depletion, and in the absence of Ptch1 all Gli3 is processed into the activator form Gli3a, consecutively preventing desensitization (figure 5.1D). To leave the remaining model predictions intact, we further have to compensate for the missing desensitization by reducing the production rate of Grem1 to about 40% we avoid alterations of the downstream Shh kinetics. We will revisit this alternative parameterization when analyzing the effects of desensitization below.

5.2. The Auto-inhibition of *Shh* Results from Desensitization

In complex networks, regulatory behaviours can emerge without having been directly wired. Such mechanisms are difficult to recognize by verbal reasoning alone. The negative auto-regulation of SHH provides such an example. Thus SHH-loaded beads down-regulate Shh expression in chicken limb buds (Sanz-Ezquerro and Tickle, 2000). While we have not included a direct negative feedback of SHH on its own expression, the model reproduces the effect (figure 5.2A, c.f. table 5.1 for simulation parameters).

The model reveals that the negative auto-regulation is the result of desensitization to the Shh signal introduced above. Thus by 24h after implanting a bead in the posterior domain, the Shh from the Shh source has diffused much further than in the normal limb bud (figure 5.2C, 1st column) and little free Ptch1 is left in the posterior half (figure 5.2C, 2nd column). Free Ptch1 is required for Gli3 production (Butterfield et al., 2009; Galli et al., 2010; Hill et al., 2009; Marigo et al., 1996a), and given the short half-life of Gli3 (Harfe et al., 2004; Wen et al., 2010) the Gli3 forms quickly vanish (figure 5.2C, 3rd to 5th column). As a result, the Grem1 production becomes weaker in the posterior part and stronger in the anterior part of the limb bud (figure 5.2C, 6th column). Less Bmp sequestration in the posterior part of the limb bud by Grem1 leads to an increase in the concentration of free Bmp in the posterior part (figure 5.2C, last column) and increased inhibition of Shh production, thus resulting in the lower Shh production in response to a Shh source (figure 5.2A).

We tested the effect of an additional Shh source in the same alternative parameterization with constitutive Gli3 production as above. In such a model without desensitization more Ptch1 and Grem1 is produced due to the source (figure 5.2D), which drastically up-regulates production of Shh (figure 5.2E), demonstrating that Shh auto-inhibition consistent with experiments arises only from desensitization in our model.

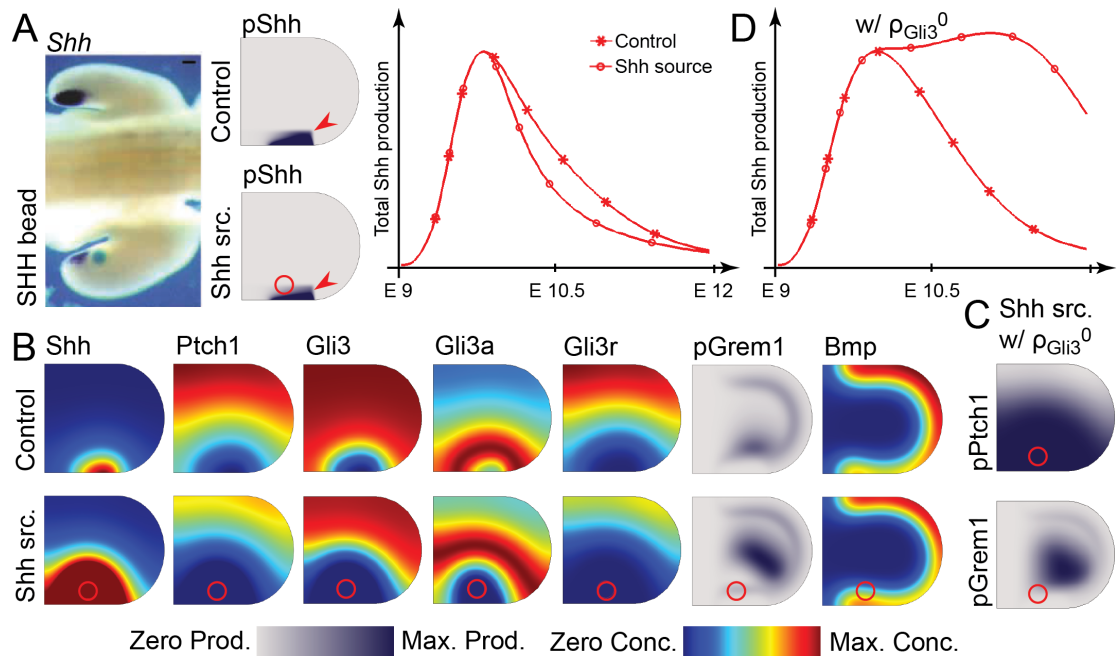


Figure 5.2.: Desensitization leads to SHH auto-regulation. (A) SHH beads limit *Shh* expression in chicken limb buds after 24 hours in culture (Sanz-Ezquerro and Tickle, 2000). An additional Shh source in the posterior part of the limb bud down-regulates Shh production in the simulation. The top row shows the control, the bottom row shows the response to the bead and the graph the total Shh production in the absence (*) and the presence (o) of the Shh source. (B) Predicted impact of the additional Shh source on the levels of key network components, i.e. *Shh*, *Ptch1*, *Gli3*, *Gli3a*, and *Gli3r* and the predicted impact of the Shh source on Gremlin production and on the concentration of free Bmp. For details see text. (C) The predicted production terms for *Ptch1* and *Grem1* in a model with a small constitutive *Gli3* production term and (D) the total Shh production in the presence and absence of a Shh bead in the same model.

5.3. Robustness to *Shh* Expression Levels

While *Shh* heterozygous mutants have 25% less *Shh* expression but no limb patterning phenotype (Bénazet et al., 2009; Chiang et al., 1996), more severe reductions in *Shh* expression as observed in the *Gremlin* mutant result in oligodactyly (Zúñiga et al., 2004). Mutants that express more *Shh* show rather mild phenotypes, e.g. the AER specific *Smo* knockout (Bouldin et al., 2010). We therefore tested the robustness of our model to changes in Shh production by varying the Shh production rate from 0 to 500%. When plotting the maximal total total *Ptch1* production versus the maximal total Shh production we find that the activity seems to plateau towards higher Shh production, also in the case of the additional constitutive *Gli3* production rate (figure 5.3A). In the latter case the activity is higher due to the lacking desensitization and total Sonic production

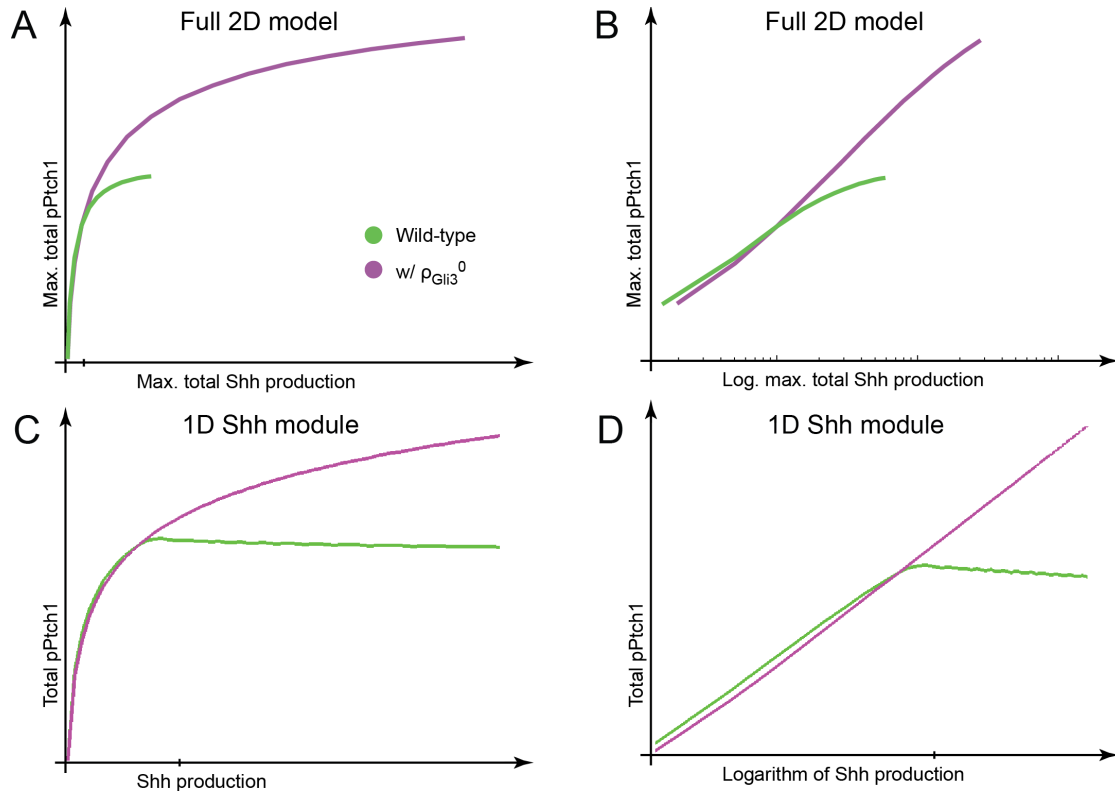


Figure 5.3.: Robustness to Shh production. (A) The Shh activity measured as maximal total Ptch1 production versus the maximal total Shh production for varying Shh production rates in the full wild-type model (green curve) and with a constitutive Gli3 production rate (purple curve) that disables desensitization. (B) Log-linear plot of the same simulation data. (C) The total Ptch1 production in a one-dimensional implementation of the Shh-Ptch1-Gli3-module. The tick indicates the Shh production corresponding to the gold-standard 2D model. (D) The same simulation data plotted on a log-x scale.

reached is higher due to the strong positive feedback. Plotting the Shh production on a logarithmic scale shows, that the activity seems to grow logarithmically (figure 5.3B).

To analyze this robustness in more depth and without geometry effects, we solved for the steady-state of the Shh-Ptch1-Gli3-module describing the SHH-pathway on a large enough one-dimensional domain for various levels of Shh influx. Then we calculated the maximal total Shh activity as measured by the integral over the inhibition by Gli3r. The green curve in figure 5.3 C shows that the regulatory network can buffer Shh signaling over space. Thus, as we increase Shh production 4-fold the activity of the Shh pathway (i.e. the expression levels of Ptch1) increases only by about one third. As we reduce Shh expression to half of the wild-type level we only lose 20% of the activity (figure 5.3C, green curve).

Within this framework we can also analyze the impact of the desensitization to Shh

signaling without having to deal with the drastic changes of the feedback-loop dynamics that the necessary perturbations introduce. Thus if we add a constitutive Gli3 production term as in the analysis of desensitization above, the activity levels are only slightly reduced due to the increased sequestration, but again the overall behavior stays the same (figure 5.3C, purple curve). However, due to the loss of basal activity in the desensitized region, the activity reaches a maximum at Shh levels that start to induce desensitization (figure 5.3C, green curve).

Plotted on a log-x scale (figure 5.3D) these curves are straight lines, indicating that the activity is proportional to the logarithm of the production. An exponential gradient read out at a certain threshold responds the same way to changes in the gradient (Lander et al., 2009). Part of the robustness is thus an intrinsic consequence of the localized source of a diffusing ligand and desensitization adds to the robustness of the Shh signaling pathway not only as a mechanism for Shh auto-inhibition but also by limiting its activity.

6. The Bovine Limb Buds Response to SHH

This chapter has been written along with the experimental study of bovine limb bud development published as **López-Ríos, J., Duchesne, A., Speziale, D., Andrey, G., Peterson, K. A., Germann, P., Erkan, Ü., Liu, J., Barbey, S., Gallard, Y., Floriot, S., Müller-Gerbl, M., Courtney, A. D., Klopp, C., Rodriguez, S., Ivanek, R., Beisel, C., Wicking, C., Iber, D., Robert, B., McMahon, A. P., Duboule, D. and Zeller, R.** (2014) Attenuated sensing of SHH by *Ptch1* underlies adaptive evolution of bovine limbs. *Nature* **511**, 46-51. ISSN 0028-0836. It arose from extensive discussions with our experimental collaborators, mainly Rolf Zeller and Javier López-Ríos. While we use the SHH pathway module derived and calibrated in chapter 3 this chapter is self-contained.

Abstract

Bovine limb development differs from the one in mouse in that the asymmetric expression patterns that are observed in AP direction in the mouse are detectable in the bovine only in the early phases of limb development. The lack of *Ptch1* up-regulation in response to SHH was observed as potential cause for these changes. By applying the SHH pathway module of our computational model for murine limb bud patterning (c.f. chapter 3) to the situation in bovine limb bud development we demonstrate that the missing up-regulation of *Ptch1* indeed leads to this loss of asymmetry, while the different length and time scale would not.

6.1. Bovine Limb Development

To uncover the distinct regulation leading to limbs with four symmetric digits (in contrast to mice, who have five asymmetric digits) our collaborators analyzed the expression of genes involved in patterning the limb bud in bovine embryos (López-Ríos and Duchesne et al., *submitted*). While the expression of AER-*Fgfs* and *Shh* seem to be conserved (figure 6.1A), the asymmetry in the expression of the down-stream genes *Gli1* (figure 6.1B), *Grem1* and *Hoxd13* observed in murine limb buds is progressively lost in bovine limb buds; leading to symmetric *Sox9*-expressing condensations without digit 1 (figure 6.1C). Interestingly the expression of the SHH-receptor *Ptch1* does not follow this trend; it is only up-regulated in the posterior ectoderm and not in the mesenchyme upon SHH signaling in bovine limb buds (figure 6.1D).

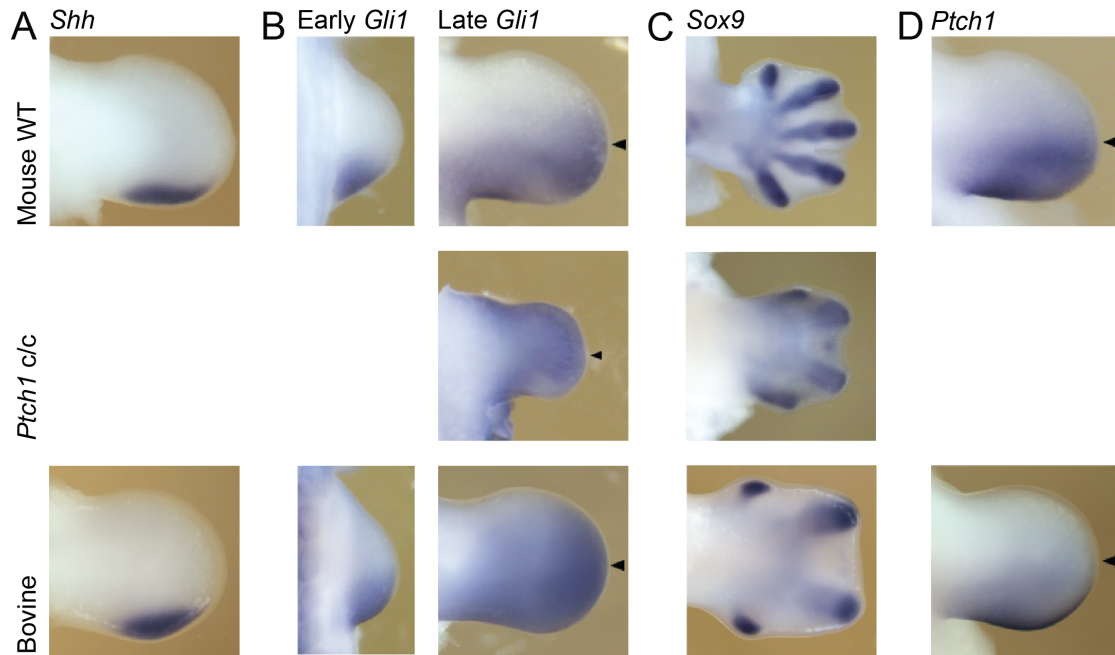


Figure 6.1.: Bovine limb bud gene expression patterns compared to the ones in wild-type and *Ptch1^{c/c}* mice. (A) *Shh* is expressed in a similar fashion in all three animals. (B) In the mutant and bovine limb buds asymmetry in SHH-target genes, like *Gli1*, asymmetry is consecutively lost, (C) resulting in *Sox9* expressing condensations that are symmetrically arranged. (D) The SHH-receptor *Ptch1* is not up-regulated in bovine limb buds. The early expression patterns are from E10 and D30, the late ones from E11.25-11.5 and D34. The condensations stained by *Sox9* are from E12.75 and D41. Data shown in this figure are provided by Javier López-Ríos, Amanadine Duchesne and Dario Speziale – for more details see López-Ríos et al. (2014).

To test whether the difference in *Ptch1* regulation can explain the progressive loss of asymmetry we apply the Shh-module of our model to the bovine situation in the remainder of this chapter. After introducing the model we explore how the gradient is built, how it is read out and how the alteration of *Ptch1* production in the bovine model changes the way cells respond to stimulation by Shh.

6.2. Modeling the Bovine SHH-Pathway

The Shh-Ptch1-Gli3-Module in 1D

We will focus on the smallest subnetwork capturing these observations; it comprises SHH, PTCH1, GLI3, GLI3A, and GLI3R and the expression of *Gli1* as a readout (figure 6.2A). Unbound PTCH1 enhances the expression of *Gli3* (Hill et al., 2009; Butterfield et al., 2009; Marigo et al., 1996b), as well as its enzymatic processing into GLI3R, while it

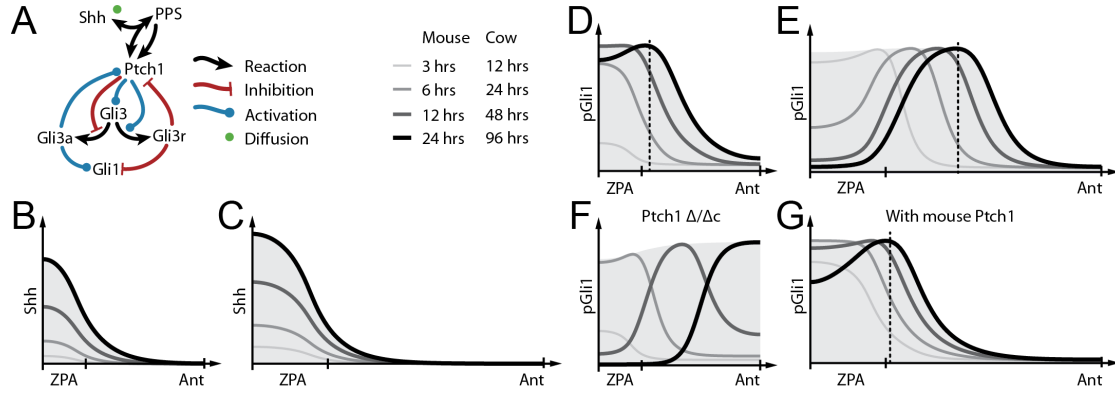


Figure 6.2.: A one-dimensional model for the Shh pathway response in the bovine limb bud. (A) The regulatory network we consider. (B, C) The calculated Shh gradient in the murine (B) and the bovine (C) simulation. (D, E) The predicted Gli1 production term pGli1 in the murine (D) and the bovine (E) simulation. (F, G) The Gli1 production term in a *Prx1-Cre;Ptch1* mutant (F) and in a simulation for mouse *Ptch1* regulation on a large domain (G).

inhibits its enzymatic processing into GLI3A (Wang et al., 2000). Binding of SHH to its receptor PTCH1 sequesters PTCH1, and thereby inhibits these effects. As SHH forms multimers (Goetz et al., 2006) we assume one such SHH multimer to bind two PTCH1 receptors at a time. PTCH1 in turn is a target of SHH signaling (Vokes et al., 2008) and thus controlled by the transcription factors GLI3A and GLI3R. Finally we use *Gli1* expression as readout for SHH signaling activity (Vokes et al., 2008) and given its lower activity in the posterior (citation needed) we set the threshold of inhibition by GLI3R to 50% of the one for the inhibition of PTCH1.

SHH is the only of the proteins that can diffuse within the domain. We therefore formulate the model by coupling a reaction-diffusion equation for SHH to a set of ordinary differential equations for the other components. For simplicity we do not consider mRNA explicitly and compare measurements of mRNA distributions to the predicted production terms. We use the convention Xyz for the computational variable representing protein XYZ corresponding to gene Xyz and denote the $PTCH1^2 \cdot SHH$ -complex by PPS. We then have

$$\begin{aligned}
\partial_t \text{Shh} &= D_{\text{Shh}} \Delta \text{Shh} + \rho_{\text{Shh}} \cdot \theta(x - \text{ZPA}) - \delta_{\text{Shh}} \cdot \text{Shh} \\
&\quad - k_{\text{PPS}}^+ \cdot \text{Shh} \cdot \text{Ptch1}^2 + k_{\text{PPS}}^- \cdot \text{PPS} \\
\partial_t \text{Ptch1} &= \rho_{\text{Ptch1}} \cdot \sigma(\text{Gli3a}) \cdot \bar{\sigma}(\text{Gli3r}) - \delta_{\text{Ptch1}} \cdot \text{Ptch1} \\
&\quad - 2 \cdot k_{\text{PPS}}^+ \cdot \text{Shh} \cdot \text{Ptch1}^2 + 2 \cdot k_{\text{PPS}}^- \cdot \text{PPS} + 2 \cdot \delta_{\text{Prec}} \cdot \text{PPS} \\
\partial_t \text{PPS} &= k_{\text{PPS}}^+ \cdot \text{Shh} \cdot \text{Ptch1}^2 - k_{\text{PPS}}^- \cdot \text{PPS} - \delta_{\text{Prec}} \cdot \text{PPS} \\
\partial_t \text{Gli3} &= \rho_{\text{Gli3}} \cdot \sigma(\text{Ptch1}) - \delta_{\text{Gli3}} \cdot \text{Gli3} \\
&\quad - k_{\text{Gli3a}} \cdot \bar{\sigma}(\text{Ptch1}) \cdot \text{Gli3} - k_{\text{Gli3r}} \cdot \sigma(\text{Ptch1}) \cdot \text{Gli3}
\end{aligned}$$

$$\begin{aligned}
\partial_t \text{Gli3a} &= k_{\text{Gli3a}} \cdot \bar{\sigma}(\text{Ptch1}) \cdot \text{Gli3} - \delta_{\text{Gli3a}} \cdot \text{Gli3a} \\
\partial_t \text{Gli3r} &= k_{\text{Gli3r}} \cdot \sigma(\text{Ptch1}) \cdot \text{Gli3} - \delta_{\text{Gli3r}} \cdot \text{Gli3r} \\
\text{pGli1} &= \sigma(\text{Gli3a}) \cdot \bar{\sigma}(\text{Gli3r})
\end{aligned}$$

where activation $\sigma(X, K) = X^2/(X^2 + K^2)$ and inhibition $\bar{\sigma}(X, K) = K^2/(X^2 + K^2)$ is modeled as second order Hill kinetics and where we omit the threshold K in the arguments. As we are interested in this readout downstream of SHH we impose the regulation of SHH for the sake of simplicity.

We solve these equations on a 1D domain of size L_0 , representing the anterior-posterior axis of the developing limb bud. We initialize the ODEs at steady state and impose the production of Shh in the posterior margin marked ZPA. We use COMSOL Multiphysics finite elements package to solve the equations numerically (c.f. chapter 2). The kinetic parameters of this model summarized in table 6.1 have been calibrated based on extensive comparison to wild-type and mutant data in a 2D model that contained modules for BMP and AER-FGF signaling in addition to this module for SHH signaling (c.f. chapter 3). We use millimeters (mm) as unit of length and days (d) as unit of time. As the concentrations have not been established experimentally, their units remain arbitrary.

To assess the sensitivities of the parameters in this particular setting we identified a tolerable range for each parameter, within which the predicted wild-type steady state Gli1 production (cf. A one-dimensional model for the Shh pathway response in the bovine limb bud. (A) The regulatory network we consider. (B, C) The calculated Shh gradient in the murine (B) and the bovine (C) simulation. (D, E) The predicted Gli1 production term pGli1 in the murine (D) and the bovine (E) simulation. (F, G) The Gli1 production term in a *Prx1-Cre;Ptch1* mutant (F) and in a simulation for mouse Ptch1 regulation on a large domain (G)D, strongest curves) remains between the curves parallel in a distance of 0.025 to the solution for the proposed parameter values. Please note that as the perturbations can add up, not all parameters can be independently chosen within the tolerable range at the same time.

Simulating the SHH Gradient

From measurements we know that the length of the anterior-posterior axis in mice at E10.5 is about $L_0 = 0.75mm$. The ZPA covers about 20% of the AP axis and we assume the SHH pathway to be up-regulated between E9.75 and E10.75 in mice. Thus we linearly raise the production rate of Shh within from zero to over a period of 18 hours, allowing the system to almost reach steady state within one day. The resulting Shh gradient reproduces the measured extracellular SHH protein distribution in the murine mesenchyme (figure 6.2B).

Bovine limb buds at a comparable stage are about 1.8 times larger and develop four times slower. Thus we scale by a factor 1.8 and raise the Shh production over three days to simulate development in cows. To analyze the impact of the missing *Ptch1* up-regulation we remove the impact of Gli3A and Gli3R on Ptch1 production, which we keep at the constant steady state level. The resulting Shh gradient (figure 6.2C) also reproduces the measured extracellular SHH protein distribution in the proximal bovine

Parameter	Proposed Value	Tolerable Range	Physiological Range
D_{Shh}	$0.12 \text{ mm}^2/d = 1.4 \text{ } \mu\text{m}^2/s$	0.1 ... 0.14	0.1 ... $50 \text{ } \mu\text{m}^2/s$
ρ_{Shh}	1	0.91 ... 1.08	
ρ_{Ptch1}	10^{-2}	0.93 ... $1.1 \cdot 10^{-2}$	
ρ_{Gli3}	2600	2427 ... 2820	
K_{Ptch1}^{Gli3a}	1	0.92 ... 1.07	
\bar{K}_{Ptch1}^{Gli3r}	20	15.06 ... 26.01	
K^{Ptch1}	10^{-3}	0.96 ... $1.04 \cdot 10^{-3}$	
\bar{K}^{Ptch1}	$5 \cdot 10^{-5}$	3.8 ... $7.2 \cdot 10^{-5}$	
δ_{Shh}	8 d^{-1} , half-life: 2.1 h	7.14 ... 9.08	0.1 ... 1 h
δ_{Ptch1}	1.2 d^{-1}	0.036 ... 2.756	
δ_{PPS}	4 d^{-1}	2.54 ... 6.07	
δ_{Prec}	0.2 d^{-1}	0 ... 0.713	
δ_{Gli3}	4 d^{-1} , half-life: 4.2 h	0 ... 80.5	$\sim 2 \text{ h}$
δ_{Gli3a}	10 d^{-1}	9.30 ... 10.63	
δ_{Gli3r}	20 d^{-1} , half-life: 0.83 h	15.10 ... 25.98	$\sim 4 \text{ h}$
k_{PPS}^+	$7.143 \cdot 10^6$	6.5 ... $7.7 \cdot 10^6$	
k_{PPS}^-	1	0.62 ... 1.52	
k_{Gli3a}	5000	2922 ... 9844	
k_{Gli3r}	6000	3057 ... 10286	

Table 6.1.: Parameters of the Shh signalling module. Here K_X^A denotes the Hill constant of activation of X by an activator A and \bar{K}_X^I the Hill constant of inhibition of X by an inhibitor I. The physiological ranges have been established in Yu et al., 2009; Müller et al., 2013; Kicheva et al., 2007; Wen et al., 2010; Harfe et al., 2004. The Hill constant for activation of the readout pGli1 is K_{Ptch1}^{Gli3a} and the threshold of inhibition is $\bar{K}_{Ptch1}^{Gli3r}/2$.

mesenchyme, while the measured SHH gradient reaches further anterior in the distal portion of the bovine limb bud. We attribute this discrepancy to the large gap between the bovine mesenchyme and ectoderm, where diffusion of SHH seems to be augmented.

Another interpretation of the experimental results would be that the SHH gradient reaches further in bovine limb buds due to less sequestration by PTCH1. There is actually evidence from the (much smaller) wing disc and neural tube that sequestration of SHH by PATCHED shapes the SHH gradient (Chen and Struhl, 1996; Briscoe et al., 2001). However in these experiments the expression boundaries of SHH target genes are

only shifted by a few cells, which corresponds well to the negligible expansion of the simulated gradient in the absence of *Ptch1* (data not shown).

Reading the Gradient

We use the predicted production of Gli1 (pGli1) as a readout for the Shh gradient, and compare it to the measured *Gli1* mRNA distributions. Thus the predicted production terms reproduce the up-regulation of *Gli1* in the posterior of murine limb buds (figure 6.2D) and the similar Gli1 expression in early bovine limb buds, which becomes subsequently more symmetric (figure 6.2E).

As additional verification of our model we simulate the *Prx1-Cre;Ptch1* conditional mutant (Butterfield et al., 2009) by stopping production of *Ptch1* after initialization. This leads to strong desensitization in the posterior and Gli1 production throughout the anterior (figure 6.2F) consistent with measured *Gli1* mRNA distributions in the *Prx1-Cre;Ptch1* mutant (figure 6.1B; Bruce et al. 2010).

Finally we simulate our model for wild-type mice on the larger bovine domain. For this artificial situation our model predicts the Gli1 production to be strongly biased to the posterior (figure 6.2 G), demonstrating that the different length and time scales are not enough and the missing up-regulation of *Ptch1* is needed for the loss of asymmetry in bovine limb buds.

Given that lacking sequestration is not the main reason for the expansion of Gli1 production within our model (see section §6.2), we explore the responses of the murine and bovine Shh-*Ptch1*-Gli3-module in an implementation of the model as a set of ordinary differential equations (corresponding to observing a single cell or equivalently a “well-stirred” population of cells without spatial inhomogeneities). In figure 6.3 we plot the predicted Gli1 production rate for imposed varying Shh production rates. Thus figure 6.3A shows that the bovine Shh module responds to lower Shh concentrations, while the plot on logarithmic scale in figure 6.3B shows that the orders of magnitude that are translate into a graded response are similar in our implementation.

Taken together our simulations suggest that the altered regulation of *Ptch1* is indeed needed and sufficient to explain the loss of asymmetry in the bovine mesenchyme.

6.3. Discussion

This *in silico* analysis is part of a large study on bovine limb bud patterning (López-Ríos and Duchesne et al., *submitted*). In the course of this study, first the loss of asymmetry in gene expression was discovered by *in situ* hybridization. Thorough analysis of genes involved in the SHH signaling pathway pointed to the missing up-regulation of the SHH receptor *Ptch1* in the bovine limb bud mesenchyme as potential cause. The limb-specific conditional *Ptch1* mutant also agreed well with this hypothesis, as its four symmetric digital condensations are remarkably similar to the condensations in cow limb buds. By mathematical modelling we then demonstrated that the observed lack of *Ptch1* up-regulation in the bovine mesenchyme is indeed sufficient to explain the loss of asymmetry in SHH target genes. On the molecular level, by comparing anterior and posterior halves

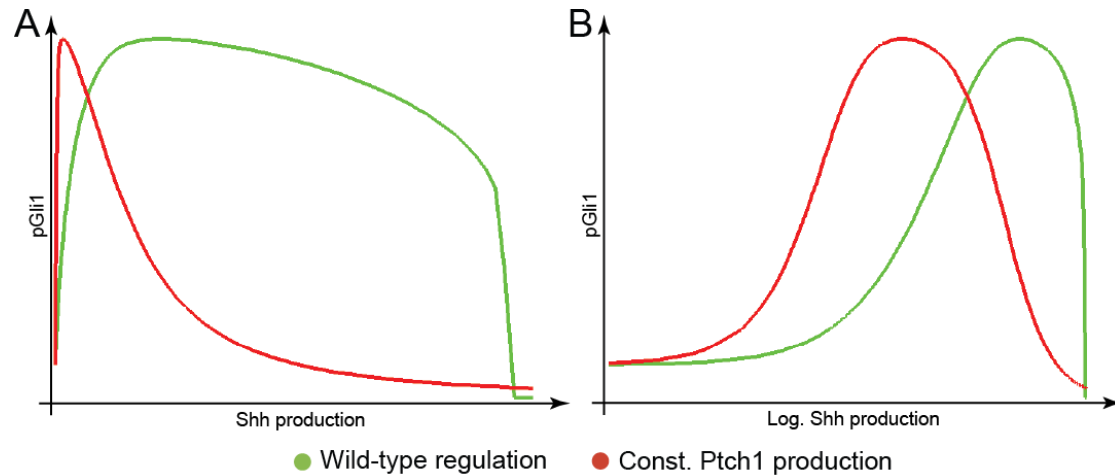


Figure 6.3.: The predicted Gli1 production in an ODE implementation of the wild-type (green) and bovine (red) Shh module for varying Shh production on normal (A) and logarithmic scale (B).

of limb buds to telecephalon tissue using chromosome conformation capture combined with high-throughput sequencing (4C-seq; van de Werken et al. 2012), a limb specific *cis*-regulatory module (LRM) was identified, that loops to the *Ptch1* promoter. Within this region three evolutionary conserved GLI-binding sites were identified by chromatin immunoprecipitation in combination with deep sequencing (ChIP-Seq), containing two artiodactyl-specific insertions. Finally the bovine LRM was then shown to drive less *LacZ* expression in the mesenchyme of transgenic mice. Together these pieces strongly suggest that the loss of *Ptch1* up-regulation in the limb bud mesenchyme was an important step in the evolution of artiodactyls.

The observation that morphological evolution is driven by mutations in regulatory rather than in protein-coding DNA has been made before (Peter and Davidson, 2011). For instance *Prx1* expression under the control of the bat enhancer results in elongated limbs in mice, while deletion of the wild-type enhancer does not lead to any phenotype in mice, suggesting redundancy in the regulation of *Prx1* (Cretekos et al., 2008). Given the multiple GLI-binding sites that have been associated with *Ptch1* (Vokes et al., 2007) also the regulation of *Ptch1* might be redundant, facilitating evolution on the level of regulation. Additionally, *Ptch1* is essential for mice (Goodrich et al., 1997), potentially impeding evolution of the protein-coding sequence.

Part IV.
Discussion

7. Conclusions

Essentially, all models are wrong,
but some are useful.

(Box and Draper, 1987)

The limb bud served for decades as a model system for development. Our understanding of the involved processes is becoming increasingly too complex for verbal reasoning alone. In this thesis we thus presented a data-based, spatio-temporal model of the feedback loop between the limb organizers, i.e. the AER and the ZPA, that pattern the anterior-posterior limb bud axis (Zeller et al., 2009). Previous mathematical models of this process did not incorporate space (Bénazet et al., 2009) and little genetic detail (Dillon and Othmer, 1999; Dillon et al., 2003) in comparison to the vast literature available. Thus, we strove to incorporate this knowledge into a computational framework. First, we constructed a regulatory network free of missing players or contradictions to experimental data. We then employed perturbations to gain insight into behaviours that emerge in the simulations of that network. This approach has been termed *in silico* genetics (Iber and Zeller, 2012). Finally, we applied a sub-model within a large study, that also contained multiple experimental techniques, to uncover the molecular basis of a morphogenetic adaption, namely the loss of asymmetry in bovine limbs (López-Ríos and Duchesne et al., *submitted*). Recently, such combination of experimental approaches with *in silico* analysis is becoming increasingly common in the field of limb bud development (Bénazet et al., 2009; Probst et al., 2011; Sheth et al., 2012), underlining the need for broadly applicable systems biology models of organogenesis.

7.1. Achievements and Predictions

In the following we summarize what we learned from construction and analysis of our model and how that knowledge could be experimentally tested:

Simulating Organogenesis Organogenesis is a tightly regulated process and can thus be addressed with mechanistic models, that allow simulations of comparably large networks in space and time. To simulate more genetic detail we first had to find an efficient and flexible framework. The finite element package COMSOL Multiphysics is suitable for our purpose and we developed strategies to optimize their implementation that substantially reduce computational times, making our model possible in the first place (c.f. chapter 2). Our group keeps exploring the possibilities of COMSOL Multiphysics (Menshykau and Iber, 2012; Menshykau et al., 2013) and employs this framework to study processes of organogenesis, e.g. branching morphogenesis (Cellière et al., 2012; Menshykau and Iber,

2013), long bone formation (Tanaka and Iber, 2013) and follicle development (Bächler et al., 2014).

Consistent Regulatory Network of Limb Bud Patterning Rather than addressing a specific question, we sought to integrate the vast body of experimental work on anterior-posterior limb bud patterning (Zeller et al., 2009) into this computational framework, as a next step towards the *in silico* limb (Iber and Zeller, 2012). The process of construction itself already lead to insights; counter-intuitive experimental observations, like the *Grem1* expression in the *Shh-Cre;Fgfr1/2* mutant (Verheyden and Sun, 2008), made sense and gaps in the understanding became evident (see section §7.2 below).

By proposing that accumulating BMP signaling is the clock that times this epithelial-mesenchymal feedback-loop – first initiating AER formation and finally terminating *Shh* expression – we found a regulatory network that is free of unknown players and qualitatively consistent with all data available (c.f. chapter 3). Like any other prediction, this role of BMP has to be experimentally verified. By collecting time course data of *Shh* expression in *Grem1* mutant limb buds one could falsify our prediction that *Grem1* not only controls the amount, but also the timing of *Shh* expression (c.f. section §4.2). Given the redundancy on all levels (Miyazono et al., 2010) the BMP pathway might be most promisingly targeted by over-expression of the antagonist *Grem1*. Our model predicts *Shh* expression not to terminate above a certain level of *Grem1* over-expression (c.f. section §4.3).

Dynamics of Limb Bud Patterning While our model was constructed mainly from static spatial gene expression data, it allows for visualization not only of the temporal evolution of the production terms that are comparable to data, but also predicts the dynamics of the concentrations and the regulatory interaction strengths. To illustrate their contributions to the emerging dynamics we can target each interaction on its own, which is tedious in conventional genetics. Following this approach we found the need for a negative regulation of *Grem1* production – either by FGF signaling (Verheyden and Sun, 2008) or the lacking *Grem1* expression in Sonic descendants (Scherz et al., 2004) – in our model, but further experiments are necessary to conclusively determine the roles of these two inhibitory interactions (c.f. section §4.3).

Auto-regulation of *Shh* and Desensitization to SHH However our model goes beyond a “computational review” by exhibiting emerging properties that would be difficult to find by verbal reasoning. *In silico* genetics (Iber and Zeller, 2012) then allowed us to probe the mechanisms underlying these behaviors by introducing perturbations. Thus, we found *Shh* auto-inhibition upon adding a *Shh* source – which is also observed experimentally (Sanz-Ezquerro and Tickle, 2000) – despite the positive effect of *Shh* on itself via the feedback-loop (c.f. figure 3.1). In our model, the auto-inhibition of *Shh* is due to ectopic desensitization, which in turn is a consequence of full-length *Gli3* depletion (c.f. section §5.1). To probe this mechanism we added a small constitutive production constant to the *Gli3* production rate that is usually down-regulated upon *Shh* signaling

(Marigo et al., 1996b). In such simulations desensitization is lost and Shh is auto-activating (c.f. section §5.2). Again these prediction can and should be experimentally verified; by analyzing *Ptch1* and *Grem1* expression in the presence of a SHH bead one could test whether SHH indeed induces ectopic desensitization and by constitutively expressing small amounts of *Gli3* throughout the limb bud the proposed mechanism for desensitization could be probed.

Intrinsic Robustness to SHH Signaling Furthermore we can explore the consequences of these emerging behaviours within our model. Thus, by varying the Shh production, we show that the way the mesenchyme interprets the secreted SHH is intrinsically robust, i.e. the Shh-activity grows slower towards high Shh production. To isolate the underlying principles we separated the SHH-pathway-module from the feedback-loop and analyzed it in lower-dimensional calculations to avoid geometry effects. Our holistic approach adds credibility to the recovered sub-models, as they have to stand tests that would otherwise be out of the scope of such toy models. The observed robustness is intrinsic to such systems as a readout of an exponential gradient is to be expected to move logarithmically with the strength of the source (Lander et al., 2009).

This analysis agrees with observations in mutants with different *Shh* expression levels. Thus, mice lacking one *Shh* copy express 25% less *Shh*, but appear normal (Bénazet et al., 2009; Chiang et al., 1996), *Grem1* mutants express 50% *Shh* resulting in only three digits (Bénazet et al., 2009; Zúñiga et al., 2004) and AER-specific *Smo* knockouts express more *Shh* but show a mild phenotype (Bouldin et al., 2010).

Desensitization to SHH adds another layer of robustness by keeping the area of Shh activity constant above a certain amount of secreted Shh (c.f. section §5.3). The role of the desensitization depends crucially on the mechanism behind. For instance, if only cells that expressed *Shh* are desensitized – analogous to the way they do not express *Grem1* (Farin et al., 2013) – the contribution to robustness might be less if the same cells express more *Shh* and their number does not change. Whether more SHH induces more desensitization could be assessed by bead experiments.

Bovine Limb Bud Patterning Finally, as we intentionally built a modular model, it can be easily extended, adapted or simplified for the analysis of specific experimental observations. We exploited this modularity in chapter 6 where we only use the Shh-Ptch1-Gli3-module to analyze the down-stream consequences of the lacking up-regulation of *Ptch1* in the bovine limb bud mesenchyme. Our model suggests that the difference in regulation is sufficient to explain the observed loss of asymmetry in other SHH target genes, mainly because of the module responding to lower Shh concentrations and not due to less sequestration of SHH. The role of SHH sequestration in controlling the reach of SHH activity could be elucidated by measuring the SHH gradient in *Prx1-Cre;Ptch1* mutant limb buds.

7.2. Open Questions and Outlook

Our model is no exception and does have its limitations. Recapitulating these shortcomings demonstrates how the *in silico* genetics approach highlights gaps in our knowledge and allows a glimpse at possible future studies based on the presented work:

Technical Constraints While Finite Element Methods allow for flexible models that are solved fast (c.f. chapter 2), they only provide mean field solutions. Thus, we can only provide a global sensitivity analysis of the mean parameters. While such an analysis certainly provides a measure for the importance and evolvability of specific processes, its value with respect to spatial biological noise (e.g. cell-to-cell variation) is questionable at most. Preliminary calculations suggest that certain globally sensitive parameters are very robust to local noise (e.g. the production rate of the secreted Bmp – probably due to diffusion evening out the noise), but the possibilities of FEM are very limited in this regard. Thus, a stochastic implementation of our model would be needed to assess the parameters sensitivities towards noise and see whether spatial mechanisms affect these local sensitivities in comparison to the global sensitivities we assessed. Such an analysis would be particularly interesting in combination with an experimental study, as the emerging single-cell transcriptomics (Tang et al., 2011) and fluorescent *in situ* hybridization (Amano et al., 2009) could provide clues on noise control at the level of transcription in nature that could be compared to the *in silico* analysis.

Simplifications Simplification of the biological processes is certainly a technical necessity, but also keep the regulatory network manageable. However they also lead to unrealistic parameter values and limit the processes that can be understood within our model. Even in the module for the SHH pathway that we implemented in more detail we are not able to capture the different kinetics of activation and deactivation that have been experimentally observed (Harfe et al., 2004; Wen et al., 2010). Studying this module in more in depth would be particularly exciting as SHH is also central in the patterning of the neural tube where quantitative data is collected (Dessaud et al., 2007; Balaskas et al., 2012). In addition such a model might help to solve the conundrum around the role of the redundancy on the level of the GLI1-3 transcription factors that we neglected (c.f. 3.4).

Recent study suggest that SHH is not diffusing freely in the limb mesenchyme, but is actually transported along cilia and the signal is then transduced upon contact of cilia from different cells (Wen et al., 2010; Sanders et al., 2013). Cytonemes are implied in BMP and FGF signalling as well (Kornberg and Roy, 2014), thus use of Fick’s law of diffusion for morphogen transport might be an inappropriate simplification.

Spatial Restrictions Another obvious caveat of our model is the spatial restrictions we have to impose on Grem1 production, the ZPA and the AER. While certain transcription factors have been associated with these restrictions, the signals that orchestrate their expression remain controversial or largely unknown. For our model, this is particularly dissatisfying in the case of the ZPA, which additionally reaches not as far into the

mesenchyme as has been experimentally described. Growth and additional details in the FGF signaling module might improve the shape of the ZPA.

Parallelism of the Feedback Loop Quantitative assays of *Shh* and *Fgf8* expression in *Grem1* and *Grem1;Bmp4* mutant limb buds suggest that the ZPA and the AER are down-regulated in parallel by higher BMP levels (Bénazet et al., 2009). While our model captures the down-regulation of Shh and Fgf qualitatively, we were not able to fit the parallelism of the quantitative measurements due to the additive inhibitory effects of higher Bmp levels directly on Shh and on the activating Fgf.

Growth Control Besides mediating polarity, SHH is known as a proliferation signal and FGFs are thought to control cellular behavior as well (Damon et al., 2008; ten Berge et al., 2008; Gros et al., 2010). Thus growth control could provide the additional feedback that parallelizes *Shh* and *Fgf8* expression and does improve the size of the ZPA in our model. In that light it would be of great interest to couple our model for patterning to morphogenetic models to investigate how these patterning events control morphogenesis and how shape feeds back into the patterning events. As recent experimental results highlight the importance of directional cellular behaviour (Hopyan et al., 2011), the morphogenetic model would ideally be of cellular resolution.

Furthermore it would be interesting to address issues of scaling in such a framework, as more species become experimentally accessible; but it might also be particularly challenging, given that none of the gradients in our model scales and that measuring protein distributions (quantitatively) is still difficult in vertebrate limb buds, as compared to e.g. drosophila wing discs where quantitative gradients have been measured (Wartlick et al., 2011).

Dorsal-Ventral Patterning Dorsal-ventral patterning is also coupled to the feedback loop (Parr and McMahon, 1995; Yang and Niswander, 1995) and might provide another mechanism for parallelization of ZPA and AER. Additionally dorsal-ventral patterning signals are also involved in the regulation of cell polarity (Gros et al., 2010), movement (Wyngaarden et al., 2010) and proliferation (ten Berge et al., 2008). The non-AER dorsal-ventral boundary is of particular interest, as it is needed for cell survival and correct *Shh* expression (Nissim et al., 2007; Fernandez-Teran et al., 2013). It might also be involved in the regulation of *Bmps* as they remain expressed along the dorsal-ventral boundary in species where the AER only covers the most distal part of the subectodermal *Bmp* expression, e.g. in jerboa (Clifford Tabin, personal communication).

Mediation of Polarity Obviously, only computational models that combine SHH signaling with digit formation will be able to contribute new insights to the questions about how the polarizing SHH-gradient controls number of digits and is actually transduced into polarity, i.e. digit identity.

7.3. Perspective: towards *in silico* genetics

While we presented the most detailed computational model on limb bud development to date it is still a long way to *in silico* genetics, that will allow simulation of more complicated perturbations. Addressing the points above could be the first steps on this road. In the long run much more data has to be integrated to address more complex questions, e.g. crosstalk between different signalling pathways. However, this will pose several challenges.

On the level of the regulatory network large gaps need to be addressed experimentally as our knowledge is only on certain accessible aspects highly detailed. For instance we know several transcription factors that control the shape of the *Shh* expression domain, however what signals control these transcription factors is largely unknown (c.f. 3.4).

To overcome such uncertainties and incorporate more data into simulations the computational community is adopting image-based modelling. By the same token growth models can be avoided as not only expression patterns, but also the overall shape can be measured and imposed on simulations (Marcon et al., 2011; Sheth et al., 2012).

Integrating more details can lead to more realistic parameter values (c.f. 3.6) that might eventually even be measured experimentally; however in general larger models have more parameters, that need to be identified by optimization. In the context of this thesis we used optimization to explore alternative parameterizations of the Gli-Ptc-module and we experimented with recovering altered parameter values. As criteria for optimization need to be defined and the power of the COMSOL Multiphysics optimizer is limited to few parameters in comparison to the number of parameters in the model this was neither economical nor fruitful. However optimization is used in a productive way for the exploration of smaller Turing-type models that have many local optima over the parameter space (Menshykau et al., 2013).

Hopefully more capable optimizers and enough data for spatial problems will be available in the future. Meanwhile equations and corresponding parameter values of comparable models have to be tuned by hand to fit the data. For this task fast and flexible visualization possibilities and short computing times are critical. Reduced basis models might provide solutions for different parameter values in almost real-time. In this computational approach a basis is constructed from “snapshots” at different parameter values by proper orthogonal decomposition in a so-called off-line calculation. The solution for arbitrary parameter values is then approximated as linear combination of this basis in a much faster on-line calculation (Zimmermann and Görtz, 2012; Manzoni et al., 2012b). While such techniques have been successfully used for parameter estimation (Manzoni et al., 2012a; Lieberman and Willcox, 2012), it remains to be seen whether they suit models of our size and degree of non-linearity.

The much more advanced world of ordinary differential equations (ODEs) could provide a source of inspiration for the further away future of spatial simulations, as its techniques can be largely extended for partial differential equations (PDEs). For instance the systems biology markup language (SBML) provides a way to describe ODE models in an exchangeable format (Hucka et al., 2003). This description can include data and plots, making work easily reproducible using off-the-shelve software packages (Hoops

et al., 2006; Funahashi et al., 2008). These ODE models can then be made available in large repositories (Li et al., 2010) and (parts thereof) further used. As spatial models involve geometrical entities with boundary conditions and potentially sophisticated growth models, there is no markup language widely accepted. Also the use of these languages is limited compared to SBML, as most spatial problems still require dedicated solvers.

7.4. Conclusion

While most models to date have been developed to address a specific question (c.f. chapter 1), we had the vision of the *in silico* limb (Iber and Zeller, 2012) in mind, and created an organogenesis model at a level of genetic detail (c.f. chapter 3), that has not been reached before. In the process of development we came across gaps in our current knowledge, while other counter-intuitive findings suddenly made sense. In the spirit of *in silico* genetics, we then employed loss-of-function and gain-of-function perturbations to explore the emerging dynamics (c.f. chapter 4) and the underlying mechanisms (c.f. chapter 5) of the signaling network and in the tradition of mathematical biology we recovered sub-models of signaling pathways that still profit from the credibility of the full model, but can be analyzed in more depth (c.f. 5.3). Thus, a holistic approach to computational organogenesis is not only feasible, but also leads to novel insights.

Despite the caveats reviewed in section §7.2 we certainly hope that our model is a useful contribution. Its predictions hopefully inspire experiments that will in turn help to improve future computational models. We specifically built the model in a modular fashion and illustrate how it can be extended and adapted (c.f. chapter 6). While computer clusters certainly help in developing such models, the final simulation runs within minutes on an ordinary laptop and the presented results can be reproduced with very little mathematical knowledge. Taken together, we hope that the experimental community accepts our approach and our model becomes a valuable resource to the field.

Acknowledgments

First I thank my mentor Dagmar Iber for giving me the opportunity to get to know and enjoy biology, a subject that I had not even thought of when I was applying for my studies. The preliminary modeling she did together with Conradin Krämer gave me a good head start and her generous support in writing was very helpful for the finish. We acknowledge funding from the SNF Sinergia grant "Developmental engineering of endochondral ossification from mesenchymal stem cells".

Then I thank colleagues and collaborators: Denis Menshykau and Simon Tanaka, who fought many COMSOL battles by my side; Rolf Zeller and Erkan Ünal for valuable comments on the manuscript for chapter 1; Rolf Zeller and Javier López-Ríos for their extensive review of the construction of the core-network (they nicknamed the monster), which turned into chapter 3, and the continuing discussion of bovine limb development presented in chapter 6; the whole Zeller group for their patience and help with my essentially non-existing biological education; and Brian Lang and Jannik Vollmer for their help with language issues.

Of course I also thank the rest of the members of the computational biology groups – in particular Pejman and Thomas, who started at the same time as me – for turning my time at the D-BSSE into a much more pleasant experience than it is supposed to be and the occasional scientific discussion.

Last, but not least, I thank my family and friends for all their understanding and patience with me moving further down, into the lowlands, while spending most spare time further up, into the mountains. In particular I thank Stefanie; she received most of my occasional grumpiness and spent many hours commuting to do so.

Bibliography

- Ahn, K., Mishina, Y., Hanks, M. C., Behringer, R. R. and Crenshaw, E. B.** (2001). BMPR-IA signaling is required for the formation of the apical ectodermal ridge and dorsal-ventral patterning of the limb. *Development (Cambridge, England)* **128**, 4449–61. ISSN 0950-1991.
- Akam, M.** (1989). Drosophila development: making stripes inelegantly. *Nature* **341**, 282–3. ISSN 0028-0836.
- Amano, T., Sagai, T., Tanabe, H., Mizushina, Y., Nakazawa, H. and Shiroishi, T.** (2009). Chromosomal dynamics at the Shh locus: limb bud-specific differential regulation of competence and active transcription. *Developmental Cell* **16**, 47–57. ISSN 1878-1551.
- Aoki, H., Fujii, M., Imamura, T., Yagi, K., Takehara, K., Kato, M. and Miyazono, K.** (2001). Synergistic effects of different bone morphogenetic protein type I receptors on alkaline phosphatase induction. *Journal of cell science* **114**, 1483–9. ISSN 0021-9533.
- Aoto, K., Nishimura, T., Eto, K. and Motoyama, J.** (2002). Mouse GLI3 Regulates Fgf8 Expression and Apoptosis in the Developing Neural Tube, Face, and Limb Bud. *Developmental Biology* **251**, 320–332. ISSN 00121606.
- Bächler, M., Menshykau, D., De Geyter, C. and Iber, D.** (2014). Species-specific differences in follicular antral sizes result from diffusion-based limitations on the thickness of the granulosa cell layer. *Molecular human reproduction* **20**, 208–21. ISSN 1460-2407.
- Badugu, A., Kraemer, C., Germann, P., Menshykau, D. and Iber, D.** (2012). Digit patterning during limb development as a result of the BMP-receptor interaction. *Scientific reports* **2**, 991. ISSN 2045-2322.
- Balaskas, N., Ribeiro, A., Panovska, J., Dessaud, E., Sasai, N., Page, K., Briscoe, J. and Ribes, V.** (2012). Gene Regulatory Logic for Reading the Sonic Hedgehog Signaling Gradient in the Vertebrate Neural Tube. *Cell* **148**, 273–284. ISSN 00928674.
- Bandyopadhyay, A., Tsuji, K., Cox, K., Harfe, B. D., Rosen, V. and Tabin, C. J.** (2006). Genetic analysis of the roles of BMP2, BMP4, and BMP7 in limb patterning and skeletogenesis. *PLoS genetics* **2**, e216. ISSN 1553-7404.

- Barrow, J. R., Thomas, K. R., Boussadia-Zahui, O., Moore, R., Kemler, R., Capecchi, M. R. and McMahon, A. P.** (2003). Ectodermal Wnt3/beta-catenin signaling is required for the establishment and maintenance of the apical ectodermal ridge. *Genes & Development* **17**, 394–409. ISSN 0890-9369.
- Bastida, M. F., Sheth, R. and Ros, M. A.** (2009). A BMP-Shh negative-feedback loop restricts Shh expression during limb development. *Development (Cambridge, England)* **136**, 3779–89. ISSN 1477-9129.
- Ben-Zvi, D., Pyrowolakis, G., Barkai, N. and Shilo, B.-Z.** (2011). Expansion-repression mechanism for scaling the Dpp activation gradient in Drosophila wing imaginal discs. *Current biology : CB* **21**, 1391–6. ISSN 1879-0445.
- Ben-Zvi, D., Shilo, B.-Z., Fainsod, A. and Barkai, N.** (2008). Scaling of the BMP activation gradient in Xenopus embryos. *Nature* **453**, 1205–11. ISSN 1476-4687.
- Bénazet, J.-D., Bischofberger, M., Tiecke, E., Gonçalves, A., Martin, J. F., Zúñiga, A., Naef, F. and Zeller, R.** (2009). A self-regulatory system of interlinked signaling feedback loops controls mouse limb patterning. *Science (New York, N.Y.)* **323**, 1050–3. ISSN 1095-9203.
- Bénazet, J.-D., Pignatti, E., Nugent, A., Unal, E., Laurent, F. and Zeller, R.** (2012). Smad4 is required to induce digit ray primordia and to initiate the aggregation and differentiation of chondrogenic progenitors in mouse limb buds. *Development (Cambridge, England)* **139**, 4250–60. ISSN 1477-9129.
- Bénazet, J.-D. and Zeller, R.** (2009). Vertebrate limb development: moving from classical morphogen gradients to an integrated 4-dimensional patterning system. *Cold Spring Harbor Perspectives in Biology* **1**, a001339. ISSN 1943-0264.
- Bitgood, M. J. and McMahon, A. P.** (1995). Hedgehog and Bmp genes are coexpressed at many diverse sites of cell-cell interaction in the mouse embryo. *Developmental biology* **172**, 126–38. ISSN 0012-1606.
- Boehm, B., Westerberg, H., Lesnicar-Pucko, G., Raja, S., Rautschka, M., Cotterell, J., Swoger, J. and Sharpe, J.** (2010). The role of spatially controlled cell proliferation in limb bud morphogenesis. *PLoS biology* **8**, e1000420. ISSN 1545-7885.
- Bollenbach, T., Pantazis, P., Kicheva, A., Bökel, C., González-Gaitán, M. and Jülicher, F.** (2008). Precision of the Dpp gradient. *Development (Cambridge, England)* **135**, 1137–46. ISSN 0950-1991.
- Bougherara, H., Klika, V., Marsík, F., Marík, I. A. and Yahia, L.** (2010). New predictive model for monitoring bone remodeling. *Journal of biomedical materials research. Part A* **95**, 9–24. ISSN 1552-4965.

- Bouldin, C. M., Gritli-Linde, A., Ahn, S. and Harfe, B. D.** (2010). Shh pathway activation is present and required within the vertebrate limb bud apical ectodermal ridge for normal autopod patterning. *Proceedings of the National Academy of Sciences of the United States of America* **107**, 5489–94. ISSN 1091-6490.
- Box, G. E. P. and Draper, N. R.** (1987). *Empirical model-building and response surfaces*. John Wiley & Sons. ISBN 0471810339.
- Briscoe, J., Chen, Y., Jessell, T. M. and Struhl, G.** (2001). A hedgehog-insensitive form of patched provides evidence for direct long-range morphogen activity of sonic hedgehog in the neural tube. *Molecular cell* **7**, 1279–91. ISSN 1097-2765.
- Brouwers, J. E. M., van Donkelaar, C. C., Sengers, B. G. and Huiskes, R.** (2006). Can the growth factors PTHrP, Ihh and VEGF, together regulate the development of a long bone? *Journal of biomechanics* **39**, 2774–82. ISSN 0021-9290.
- Bruce, S. J., Butterfield, N. C., Metzis, V., Town, L., McGlinn, E. and Wicking, C.** (2010). Inactivation of Patched1 in the mouse limb has novel inhibitory effects on the chondrogenic program. *The Journal of biological chemistry* **285**, 27967–81. ISSN 1083-351X.
- Brunet, L. J., McMahon, J. A., McMahon, A. P. and Harland, R. M.** (1998). Noggin, Cartilage Morphogenesis, and Joint Formation in the Mammalian Skeleton. *Science* **280**, 1455–1457. ISSN 00368075.
- Buescher, D. and Ruether, U.** (1998). Expression Profile of Gli Family Members and Shh in Normal and Mutant Mouse Limb Development. *Developmental Dynamics* **211**, 88–96.
- Butterfield, N. C., Metzis, V., McGlinn, E., Bruce, S. J., Wainwright, B. J. and Wicking, C.** (2009). Patched 1 is a crucial determinant of asymmetry and digit number in the vertebrate limb. *Development (Cambridge, England)* **136**, 3515–24. ISSN 1477-9129.
- Cao, T., Wang, C., Yang, M., Wu, C. and Wang, B.** (2013). Mouse limbs expressing only the Gli3 repressor resemble those of Sonic hedgehog mutants. *Developmental Biology* **379**, 221–8. ISSN 1095-564X.
- Capdevila, J., Tsukui, T., Rodríguez Esteban, C., Zappavigna, V. and Izpisua Belmonte, J. C.** (1999). Control of vertebrate limb outgrowth by the proximal factor Meis2 and distal antagonism of BMPs by Gremlin. *Molecular cell* **4**, 839–49. ISSN 1097-2765.
- Capellini, T. D., Di Giacomo, G., Salsi, V., Brendolan, A., Ferretti, E., Srivastava, D., Zappavigna, V. and Selleri, L.** (2006). Pbx1/Pbx2 requirement for distal limb patterning is mediated by the hierarchical control of Hox gene spatial distribution and Shh expression. *Development (Cambridge, England)* **133**, 2263–73. ISSN 0950-1991.

- Cellière, G., Menshykau, D. and Iber, D.** (2012). Simulations demonstrate a simple network to be sufficient to control branch point selection, smooth muscle and vasculature formation during lung branching morphogenesis. *Biology open* **1**, 775–88. ISSN 2046-6390.
- Charité, J., McFadden, D. G. and Olson, E. N.** (2000). The bHLH transcription factor dHAND controls Sonic hedgehog expression and establishment of the zone of polarizing activity during limb development. *Development (Cambridge, England)* **127**, 2461–70. ISSN 0950-1991.
- Chen, Y., Knezevic, V., Ervin, V., Hutson, R., Ward, Y. and Mackem, S.** (2004). Direct interaction with Hoxd proteins reverses Gli3-repressor function to promote digit formation downstream of Shh. *Development (Cambridge, England)* **131**, 2339–47. ISSN 0950-1991.
- Chen, Y. and Struhl, G.** (1996). Dual roles for patched in sequestering and transducing Hedgehog. *Cell* **87**, 553–63. ISSN 0092-8674.
- Chiang, C., Litingtung, Y., Lee, E. and Young, K.** (1996). Cyclopia and defective axial patterning in mice lacking Sonic hedgehog gene function .
- Choi, K.-S., Lee, C., Maatouk, D. M. and Harfe, B. D.** (2012). Bmp2, Bmp4 and Bmp7 are co-required in the mouse AER for normal digit patterning but not limb outgrowth. *PloS one* **7**, e37826. ISSN 1932-6203.
- Cooper, K. L., Hu, J. K.-H., ten Berge, D., Fernandez-Teran, M. A., Ros, M. A. and Tabin, C. J.** (2011). Initiation of proximal-distal patterning in the vertebrate limb by signals and growth. *Science (New York, N.Y.)* **332**, 1083–6. ISSN 1095-9203.
- Cooper, K. L., Oh, S., Sung, Y., Dasari, R. R., Kirschner, M. W. and Tabin, C. J.** (2013). Multiple phases of chondrocyte enlargement underlie differences in skeletal proportions. *Nature* **495**, 375–8. ISSN 1476-4687.
- Cretekos, C. J., Wang, Y., Green, E. D., Martin, J. F., Rasweiler, J. J. and Behringer, R. R.** (2008). Regulatory divergence modifies limb length between mammals. *Genes & development* **22**, 141–51. ISSN 0890-9369.
- Crick, A. P., Babbs, C., Brown, J. M. and Morriss-Kay, G. M.** (2003). Developmental mechanisms underlying polydactyly in the mouse mutant, Doublefoot. *Journal of anatomy* **201**, 21–6. ISSN 0021-8782.
- Crossley, P. H., Minowada, G., MacArthur, C. a. and Martin, G. R.** (1996). Roles for FGF8 in the induction, initiation, and maintenance of chick limb development. *Cell* **84**, 127–36. ISSN 0092-8674.
- Cunningham, T. J., Chatzi, C., Sandell, L. L., Trainor, P. A. and Duester, G.** (2011). Rdh10 mutants deficient in limb field retinoic acid signaling exhibit normal limb

- patterning but display interdigital webbing. *Developmental Dynamics* **240**, 1142–50. ISSN 1097-0177.
- Cunningham, T. J., Zhao, X., Sandell, L. L., Evans, S. M., Trainor, P. A. and Duester, G.** (2013). Antagonism between Retinoic Acid and Fibroblast Growth Factor Signaling during Limb Development. *Cell reports* , 1–10ISSN 2211-1247.
- Dahn, R. D., Davis, M. C., Pappano, W. N. and Shubin, N. H.** (2007). Sonic hedgehog function in chondrichthyan fins and the evolution of appendage patterning. *Nature* **445**, 311–4. ISSN 1476-4687.
- Dai, P., Akimaru, H., Tanaka, Y., Maekawa, T., Nakafuku, M. and Ishii, S.** (1999). Sonic Hedgehog-induced activation of the Gli1 promoter is mediated by GLI3. *The Journal of biological chemistry* **274**, 8143–52. ISSN 0021-9258.
- Damon, B. J., Mezentseva, N. V., Kumaratilake, J. S., Forgacs, G. and Newman, S. A.** (2008). Limb bud and flank mesoderm have distinct "physical phenotypes" that may contribute to limb budding. *Developmental Biology* **321**, 319–30. ISSN 1095-564X.
- Danopoulos, S., Parsa, S., Al Alam, D., Tabatabai, R., Baptista, S., Tiozzo, C., Carraro, G., Wheeler, M., Barreto, G., Braun, T., Li, X., Hajihosseini, M. K. and Bellusci, S.** (2013). Transient Inhibition of FGFR2b-Ligands Signaling Leads to Irreversible Loss of Cellular β -Catenin Organization and Signaling in AER during Mouse Limb Development. *PloS one* **8**, e76248. ISSN 1932-6203.
- Dedner, A., Klöfkor, R., Nolte, M. and Ohlberger, M.** (2010). A generic interface for parallel and adaptive discretization schemes: abstraction principles and the Dune-Fem module. *Computing* **90**, 165–196. ISSN 0010-485X.
- Dessaud, E., Yang, L. L., Hill, K., Cox, B., Ulloa, F., Ribeiro, A., Mynett, A., Novitsch, B. G. and Briscoe, J.** (2007). Interpretation of the sonic hedgehog morphogen gradient by a temporal adaptation mechanism. *Nature* **450**, 717–20. ISSN 1476-4687.
- Dillon, R., Gadgil, C. and Othmer, H. G.** (2003). Short- and long-range effects of Sonic hedgehog in limb development. *PNAS* **100**.
- Dillon, R. and Othmer, H.** (1999). A mathematical model for outgrowth and spatial patterning of the vertebrate limb bud. *Journal of theoretical biology* **197**, 295–330.
- Duprez, D. M., Kostakopoulou, K., Francis-West, P. H., Tickle, C. and Brickell, P. M.** (1996). Activation of Fgf-4 and HoxD gene expression by BMP-2 expressing cells in the developing chick limb. *Development (Cambridge, England)* **122**, 1821–8. ISSN 0950-1991.
- Echelard, Y., Epstein, D. J., St-Jacques, B., Shen, L., Mohler, J., McMahon, J. A. and McMahon, A. P.** (1993). Sonic hedgehog, a member of a family of

- putative signaling molecules, is implicated in the regulation of CNS polarity. *Cell* **75**, 1417–30. ISSN 0092-8674.
- Ede, D. and Law, J.** (1969). Computer Simulation of Vertebrate Limb Morphogenesis. *Nature* **221**, 244–248.
- Farin, H. F., Lüdtke, T. H.-W., Schmidt, M. K., Placzko, S., Schuster-Gossler, K., Petry, M., Christoffels, V. M. and Kispert, A.** (2013). Tbx2 Terminates Shh/Fgf Signaling in the Developing Mouse Limb Bud by Direct Repression of Grem1. *PLoS Genetics* **9**, e1003467. ISSN 1553-7404.
- Fernandez-Teran, M., Ros, M. A. and Mariani, F. V.** (2013). Evidence that the limb bud ectoderm is required for survival of the underlying mesoderm. *Developmental Biology* , 1–12ISSN 00121606.
- Funahashi, A., Matsuoka, Y., Jouraku, A., Morohashi, M., Kikuchi, N. and Kitano, H.** (2008). CellDesigner 3.5: A Versatile Modeling Tool for Biochemical Networks. *Proceedings of the IEEE* **96**, 1254–1265.
- Galli, A., Robay, D., Osterwalder, M., Bao, X., Bénazet, J.-D., Tariq, M., Paro, R., Mackem, S. and Zeller, R.** (2010). Distinct roles of Hand2 in initiating polarity and posterior Shh expression during the onset of mouse limb bud development. *PLoS genetics* **6**, e1000901. ISSN 1553-7404.
- Garzon-Alvarado, D. A., García-Aznar, J. M. and Doblaré, M.** (2009). A reaction-diffusion model for long bones growth. *Biomechanics and modeling in mechanobiology* **8**, 381–95. ISSN 1617-7940.
- Garzon-Alvarado, D. A., Peinado Cortes, L. M. and Cardenas Sandoval, R. P.** (2010). A mathematical model of epiphyseal development: hypothesis on the cartilage canals growth. *Computer methods in biomechanics and biomedical engineering* **13**, 765–72. ISSN 1476-8259.
- Germann, P., Menshykau, D., Tanaka, S. and Iber, D.** (2011). Simulating Organogenesis in COMSOL. *Excerpt from the Proceedings of the COMSOL Conference 2011 in Stuttgart* , 1–5.
- Gierer, A. and Meinhardt, H.** (1972). A Theory of Biological Pattern Formation. *Kybernetik* .
- Goetz, J. A., Singh, S., Suber, L. M., Kull, F. J. and Robbins, D. J.** (2006). A highly conserved amino-terminal region of sonic hedgehog is required for the formation of its freely diffusible multimeric form. *The Journal of biological chemistry* **281**, 4087–93. ISSN 0021-9258.
- Goodrich, L. V., Milenkovic, L., Higgins, K. M. and Scott, M. P.** (1997). Altered Neural Cell Fates and Medulloblastoma in Mouse patched Mutants. *Science* **277**, 1109–1113. ISSN 00368075.

- Gregor, T., Tank, D. W., Wieschaus, E. F. and Bialek, W.** (2007). Probing the limits to positional information. *Cell* **130**, 153–64. ISSN 0092-8674.
- Gros, J., Hu, J. K.-H., Vinegoni, C., Feruglio, P. F., Weissleder, R. and Tabin, C. J.** (2010). WNT5A/JNK and FGF/MAPK Pathways Regulate the Cellular Events Shaping the Vertebrate Limb Bud. *Current Biology* **20**, 1993–2002. ISSN 1879-0445.
- Guimond, J.-C., Lévesque, M., Michaud, P.-L., Berdugo, J., Finnson, K., Philip, A. and Roy, S.** (2010). BMP-2 functions independently of SHH signaling and triggers cell condensation and apoptosis in regenerating axolotl limbs. *BMC developmental biology* **10**, 15. ISSN 1471-213X.
- Haramis, A.-P. G., Brown, J. M. and Zeller, R.** (1995). The limb deformity mutation disrupts the SHH/FGF-4 feedback loop and regulation of 5' HoxD genes during limb pattern formation. *Development (Cambridge, England)* **121**, 4237–45. ISSN 0950-1991.
- Harfe, B. D., Scherz, P. J., Nissim, S., Tian, H., McMahon, A. P. and Tabin, C. J.** (2004). Evidence for an expansion-based temporal Shh gradient in specifying vertebrate digit identities. *Cell* **118**, 517–28. ISSN 0092-8674.
- Hentschel, H. G. E., Glimm, T., Glazier, J. a. and Newman, S. a.** (2004). Dynamical mechanisms for skeletal pattern formation in the vertebrate limb. *Proceedings. Biological sciences / The Royal Society* **271**, 1713–22. ISSN 0962-8452.
- Hill, P., Götz, K. and Rüther, U.** (2009). A SHH-independent regulation of Gli3 is a significant determinant of anteroposterior patterning of the limb bud. *Developmental Biology* **328**, 506–16. ISSN 1095-564X.
- Hilton, M. J., Tu, X., Cook, J., Hu, H. and Long, F.** (2005). Ihh controls cartilage development by antagonizing Gli3, but requires additional effectors to regulate osteoblast and vascular development. *Development (Cambridge, England)* **132**, 4339–51. ISSN 0950-1991.
- Hockman, D., Cretekos, C. J., Mason, M. K., Behringer, R. R., Jacobs, D. S. and Illing, N.** (2008). A second wave of Sonic hedgehog expression during the development of the bat limb. *Proceedings of the National Academy of Sciences of the United States of America* **105**, 16982–7. ISSN 1091-6490.
- Hofer, T. and Maini, P.** (1996). Turing patterns in fish skin? *Nature* **380**, 678.
- Hogan, B. L.** (1996). Bone morphogenetic proteins: multifunctional regulators of vertebrate development. *Genes & Development* **10**, 1580–1594. ISSN 0890-9369.
- Hoops, S., Sahle, S., Gauges, R., Lee, C., Pahle, J., Simus, N., Singhal, M., Xu, L., Mendes, P. and Kummer, U.** (2006). COPASI – a COMplex PATHWAY Simulator. *Bioinformatics (Oxford, England)* **22**, 3067–74. ISSN 1367-4811.

- Hopyan, S., Sharpe, J. and Yang, Y.** (2011). Budding behaviors: Growth of the limb as a model of morphogenesis. *Developmental Dynamics* **240**, 1054–62. ISSN 1097-0177.
- Horton, W. A. and Degrin, C. R.** (2009). FGFs in endochondral skeletal development. *Trends in endocrinology and metabolism: TEM* **20**, 341–8. ISSN 1879-3061.
- Hsu, D. R., Economides, A. N., Wang, X. and Eimon, P.** (1998). The *Xenopus* dorsalizing factor Gremlin identifies a novel family of secreted proteins that antagonize BMP activities. *Molecular cell* **1**, 673–683.
- Hucka, M., Finney, a., Sauro, H. M., Bolouri, H., Doyle, J. C., Kitano, H., Arkin, a. P., Bornstein, B. J., Bray, D., Cornish-Bowden, a., Cuellar, a. a., Dronov, S., Gilles, E. D., Ginkel, M., Gor, V., Goryanin, I. I., Hedley, W. J., Hodgman, T. C., Hofmeyr, J.-H., Hunter, P. J., Juty, N. S., Kasberger, J. L., Kremling, a., Kummer, U., Le Novere, N., Loew, L. M., Lucio, D., Mendes, P., Minch, E., Mjolsness, E. D., Nakayama, Y., Nelson, M. R., Nielsen, P. F., Sakurada, T., Schaff, J. C., Shapiro, B. E., Shimizu, T. S., Spence, H. D., Stelling, J., Takahashi, K., Tomita, M., Wagner, J. and Wang, J.** (2003). The systems biology markup language (SBML): a medium for representation and exchange of biochemical network models. *Bioinformatics* **19**, 524–531. ISSN 1367-4803.
- Hui, C.-C. and Angers, S.** (2011). Gli proteins in development and disease. *Annual review of cell and developmental biology* **27**, 513–37. ISSN 1530-8995.
- Iber, D. and Germann, P.** (2014). How do digits emerge? - mathematical models of limb development. *Birth defects research. Part C, Embryo today : reviews* **102**, 1–12. ISSN 1542-9768.
- Iber, D., Tanaka, S., Fried, P., Germann, P. and Menshykau, D.** (2013). Simulating Tissue Morphogenesis and Signaling. In C. M. Nelson, ed., *Tissue Morphogenesis (Methods in Molecular Biology series)*, number 1. New York: Springer.
- Iber, D. and Zeller, R.** (2012). Making sense-data-based simulations of vertebrate limb development. *Current Opinion in Genetics & Development* **22**, 570–7. ISSN 1879-0380.
- Isaksson, H., van Donkelaar, C. C., Huiskes, R. and Ito, K.** (2008). A mechano-regulatory bone-healing model incorporating cell-phenotype specific activity. *Journal of theoretical biology* **252**, 230–46. ISSN 1095-8541.
- Jiang, J. and Hui, C.-C.** (2008). Hedgehog signaling in development and cancer. *Developmental Cell* **15**, 801–12. ISSN 1878-1551.
- Karaplis, A. C., Luz, A., Glowacki, J., Bronson, R. T., Tybulewicz, V. L., Kronenberg, H. M. and Mulligan, R. C.** (1994). Lethal skeletal dysplasia from

- targeted disruption of the parathyroid hormone-related peptide gene. *Genes & Development* **8**, 277–289. ISSN 0890-9369.
- Karp, S. J., Schipani, E., St-Jacques, B., Hunzelman, J., Kronenberg, H. and McMahon, a. P.** (2000). Indian hedgehog coordinates endochondral bone growth and morphogenesis via parathyroid hormone related-protein-dependent and -independent pathways. *Development (Cambridge, England)* **127**, 543–8. ISSN 0950-1991.
- Karsenty, G., Kronenberg, H. M. and Settembre, C.** (2009). Genetic control of bone formation. *Annual review of cell and developmental biology* **25**, 629–48. ISSN 1530-8995.
- Kawakami, Y., Capdevila, J., Büscher, D., Itoh, T., Rodríguez Esteban, C. and Izpisúa Belmonte, J. C.** (2001). WNT signals control FGF-dependent limb initiation and AER induction in the chick embryo. *Cell* **104**, 891–900. ISSN 0092-8674.
- Kawakami, Y., Tsuda, M., Takahashi, S., Taniguchi, N., Esteban, C. R., Zemmyo, M., Furumatsu, T., Lotz, M., Izpisúa Belmonte, J. C. and Asahara, H.** (2005). Transcriptional coactivator PGC-1 α regulates chondrogenesis via association with Sox9. *Proceedings of the National Academy of Sciences of the United States of America* **102**, 2414–9. ISSN 0027-8424.
- Kawane, T., Mimura, J., Yanagawa, T., Fujii-Kuriyama and Horiuchi, N.** (2003). Parathyroid hormone (PTH) down-regulates PTH / PTH-related protein receptor gene expression in UMR-106 osteoblast-like cells via a 3'.5'-cyclic adenosine monophosphate-dependent, protein kinase A-independent pathway. *Journal of Endocrinology* **178**, 247–256.
- Khokha, M., Hsu, D. R., Brunet, L. and Dionne, M.** (2003). Gremlin is the BMP antagonist required for maintenance of Shh and Fgf signals during limb patterning. *Nature genetics* **34**, 303–307.
- Kicheva, A., Pantazis, P., Bollenbach, T., Kalaidzidis, Y., Bittig, T., Jülicher, F. and González-Gaitán, M.** (2007). Kinetics of morphogen gradient formation. *Science (New York, N.Y.)* **315**, 521–5. ISSN 1095-9203.
- Kmita, M., Tarchini, B., Zâkâny, J., Logan, M., Tabin, C. J. and Duboule, D.** (2005). Early developmental arrest of mammalian limbs lacking HoxA/HoxD gene function. *Nature* **435**, 1113–6. ISSN 1476-4687.
- Knezevic, V., De Santo, R., Schughart, K., Huffstadt, U., Chiang, C., Mahon, K. a. and Mackem, S.** (1997). Hoxd-12 differentially affects preaxial and postaxial chondrogenic branches in the limb and regulates Sonic hedgehog in a positive feedback loop. *Development (Cambridge, England)* **124**, 4523–36. ISSN 0950-1991.
- Kobayashi, T., Soegiarto, D. W., Zang, Y., Lanske, B., Schipani, E., McMahon, A. P. and Kronenberg, H. M.** (2005). Indian hedgehog stimulates periarter-

- ticular chondrocyte differentiation to regulate growth plate length independently of PTHrP. *Journal of Clinical Investigation* **115**, 1734–42.
- Kondo, S. and Asai, R.** (1995). A reaction-diffusion wave on the skin of the marine angelfish *Pomacanthus*. *Nature* **376**, 765–68.
- Kondo, S. and Miura, T.** (2011). Reaction-Diffusion Model as a Framework for Understanding Biological Pattern Formation. *Science* **329**, 1616–1620. ISSN 1432-1416.
- Kornberg, T. B. and Roy, S.** (2014). Cytonemes as specialized signaling filopodia. *Development* **141**, 729–736. ISSN 0950-1991.
- Kozhemyakina, E., Ionescu, A. and Lassar, A. B.** (2014). GATA6 Is a Crucial Regulator of Shh in the Limb Bud. *PLoS genetics* **10**, e1004072. ISSN 1553-7404.
- Kraus, P., Fraidenraich, D. and Loomis, C. A.** (2001). Some distal limb structures develop in mice lacking Sonic hedgehog signaling. *Mechanisms of development* **100**, 45–58. ISSN 0925-4773.
- Kronenberg, H. M.** (2003). Developmental regulation of the growth plate. *Nature* **423**, 332–6. ISSN 0028-0836.
- Lander, A. D., Lo, W.-C., Nie, Q. and Wan, F. Y. M.** (2009). The measure of success: constraints, objectives, and tradeoffs in morphogen-mediated patterning. *Cold Spring Harbor perspectives in biology* **1**, a002022. ISSN 1943-0264.
- Lanske, B., Karaplis, A. C., Lee, K., Luz, A., Vortkamp, A., Pirro, A., Karperien, M., Defize, L. H. K., Ho, C., Mulligan, R. C., Abou-Samra, A.-B., Jüppner, H., Segre, G. V. and Kronenberg, H. M.** (1996). PTH/PTHrP Receptor in Early Development and Indian Hedgehog-Regulated Bone Growth. *Science* **273**, 663–666.
- Laufer, E., Nelson, C., Johnson, R., Morgan, B. and Tabin, C. J.** (1994). Sonic hedgehog and Fgf-4 Act through a Signaling Cascade and Feedback Loop To Integrate Growth and Patterning of the Developing Limb Bud. *Cell* **79**, 993–1003.
- Lauschke, V. M., Tsiarris, C. D., François, P. and Aulehla, A.** (2013). Scaling of embryonic patterning based on phase-gradient encoding. *Nature* **493**, 101–5. ISSN 1476-4687.
- Lettice, L. A., Williamson, I., Wiltshire, J. H., Peluso, S., Devenney, P. S., Hill, A. E., Essafi, A., Hagman, J., Mort, R., Grimes, G., DeAngelis, C. L. and Hill, R. E.** (2012). Opposing functions of the ETS factor family define Shh spatial expression in limb buds and underlie polydactyly. *Developmental Cell* **22**, 459–67. ISSN 1878-1551.
- Lewandoski, M., Sun, X. and Martin, G. R.** (2000). Fgf8 signalling from the AER is essential for normal limb development. *Nature genetics* **26**, 460–3. ISSN 1061-4036.

- Li, C., Donizelli, M., Rodriguez, N., Dharuri, H., Endler, L., Chelliah, V., Li, L., He, E., Henry, A., Stefan, M. I., Snoep, J. L., Hucka, M., Le Novère, N. and Laibe, C.** (2010). BioModels Database: An enhanced, curated and annotated resource for published quantitative kinetic models. *BMC systems biology* **4**, 92. ISSN 1752-0509.
- Li, Y., Zhang, H., Litingtung, Y. and Chiang, C.** (2006). Cholesterol modification restricts the spread of Shh gradient in the limb bud. *Proceedings of the National Academy of Sciences of the United States of America* **103**, 6548–53. ISSN 0027-8424.
- Lieberman, C. and Willcox, K.** (2012). Goal-Oriented Inference: Approach, Linear Theory, and Application to Advection Diffusion. *SIAM Journal on Scientific Computing* **34**, 1880–1904.
- Litingtung, Y., Dahn, R. D., Li, Y. and Fallon, J. F.** (2002). Shh and Gli3 are dispensable for limb skeleton formation but regulate digit number and identity. *Nature* **418**, 979–983.
- Longobardi, L., Li, T., Myers, T. J., O’Rear, L., Ozkan, H., Li, Y., Contaldo, C. and Spagnoli, A.** (2012). TGF- β type II receptor/MCP-5 axis: at the crossroad between joint and growth plate development. *Developmental cell* **23**, 71–81. ISSN 1878-1551.
- López-Ríos, J., Duchesne, A., Speziale, D., Andrey, G., Peterson, K. A., Germann, P., Unal, E., Liu, J., Floriot, S., Barbey, S., Gallard, Y., Müller-Gerbl, M., Courtney, A. D., Klopp, C., Rodriguez, S., Ivanek, R., Beisel, C., Wicking, C., Iber, D., Robert, B., McMahon, A. P., Duboule, D. and Zeller, R.** (2014). Attenuated sensing of SHH by Ptch1 underlies evolution of bovine limbs. *Nature* **511**, 46–51. ISSN 1476-4687.
- López-Ríos, J., Speziale, D., Robay, D., Scotti, M., Osterwalder, M., Nusspaumer, G., Galli, A., Holländer, G. A., Kmita, M. and Zeller, R.** (2012). GLI3 constrains digit number by controlling both progenitor proliferation and BMP-dependent exit to chondrogenesis. *Developmental Cell* **22**, 837–48. ISSN 1878-1551.
- Lu, P., Minowada, G. and Martin, G. R.** (2006). Increasing Fgf4 expression in the mouse limb bud causes polysyndactyly and rescues the skeletal defects that result from loss of Fgf8 function. *Development (Cambridge, England)* **133**, 33–42. ISSN 0950-1991.
- Maatouk, D. M., Choi, K.-S., Bouldin, C. M. and Harfe, B. D.** (2009). In the limb AER Bmp2 and Bmp4 are required for dorsal-ventral patterning and interdigital cell death but not limb outgrowth. *Developmental Biology* **327**, 516–23. ISSN 1095-564X.
- MacCabe, J. A., Errick, J. and Saunders, J. W.** (1974). Ectodermal control of the dorsoventral axis in the leg bud of the chick embryo. *Developmental biology* **39**, 69–82. ISSN 0012-1606.

- Maini, P. K. and Solursh, M.** (1991). Cellular mechanisms of pattern formation in the developing limb. *International review of cytology* **129**, 91–133. ISSN 0074-7696.
- Mak, K. K., Kronenberg, H. M., Chuang, P.-T., Mackem, S. and Yang, Y.** (2008). Indian hedgehog signals independently of PTHrP to promote chondrocyte hypertrophy. *Development (Cambridge, England)* **135**, 1947–56. ISSN 0950-1991.
- Manzoni, A., Lassila, T., Quarteroni, A. and Rozza, G.** (2012a). A reduced-order strategy for solving inverse Bayesian shape identification problems in physiological flows .
- Manzoni, A., Quarteroni, A. and Rozza, G.** (2012b). Computational reduction for parametrized PDEs: strategies and applications .
- Mao, J., McGlenn, E., Huang, P., Tabin, C. J. and McMahon, A. P.** (2009). Fgf-Dependent Etv4/5 Activity Is Required for Posterior Restriction of Sonic hedgehog and Promoting Outgrowth of the Vertebrate Limb. *Developmental Cell* **16**, 600–606. ISSN 15345807.
- Marcon, L., Arqués, C. G., Torres, M. S. and Sharpe, J.** (2011). A Computational Clonal Analysis of the Developing Mouse Limb Bud. *PLoS Computational Biology* **7**, e1001071. ISSN 1553-7358.
- Mariani, F. V., Ahn, C. P. and Martin, G. R.** (2008). Genetic evidence that FGFs have an instructive role in limb proximal-distal patterning. *Nature* **453**, 401–5. ISSN 1476-4687.
- Marigo, V., Davey, R. A., Zuo, Y., Cunningham, J. M. and Tabin, C. J.** (1996a). Biochemical evidence that Patched is the Hedgehog receptor. *Nature* **384**, 1796–9.
- Marigo, V., Johnson, R. L., Vortkamp, a. and Tabin, C. J.** (1996b). Sonic hedgehog differentially regulates expression of GLI and GLI3 during limb development. *Developmental Biology* **180**, 273–83. ISSN 0012-1606.
- Menshykau, D., Adivarahan, S., Germann, P., Lermuzeaux, L. and Iber, D.** (2013). Simulating Organogenesis in COMSOL: Parameter Optimization for PDE-based models. *Excerpt from the Proceedings of the 2013 COMSOL Conference in Rotterdam* , 1–6.
- Menshykau, D. and Iber, D.** (2012). Simulation Organogenesis in COMSOL: Deforming and Interacting Domains. *Excerpt from the Proceedings of the 2012 COMSOL Conference in Milan* , 1–6.
- Menshykau, D. and Iber, D.** (2013). Kidney branching morphogenesis under the control of a ligand-receptor-based Turing mechanism. *Physical biology* **10**, 046003. ISSN 1478-3975.

- Menshykau, D., Kraemer, C. and Iber, D.** (2012). Branch Mode Selection during Early Lung Development. *PLoS Computational Biology* **8**, e1002377. ISSN 1553-7358.
- Mercader, N., Fischer, S., Development, C. J. N. and Neumann, C. J.** (2006). Prdm1 acts downstream of a sequential RA, Wnt and Fgf signaling cascade during zebrafish forelimb induction. *Development* **133**, 3949–3949. ISSN 0950-1991.
- Mercader, N., Leonardo, E., Piedra, M., Martinez-A, C., Ros, M. A. and Torres, M. S.** (2000). Opposing RA and FGF signals control proximodistal vertebrate limb development through regulation of Meis genes. *Development (Cambridge, England)* , 3961–3970.
- Metzger, R. J., Klein, O. D., Martin, G. R. and Krasnow, M. A.** (2008). The branching programme of mouse lung development. *Nature* **453**, 745–50. ISSN 1476-4687.
- Minina, E., Schneider, S., Rosowski, M., Lauster, R. and Vortkamp, A.** (2005). Expression of Fgf and Tgfbeta signaling related genes during embryonic endochondral ossification. *Gene expression patterns : GEP* **6**, 102–9. ISSN 1567-133X.
- Miura, T.** (2013). Turing and Wolpert work together during limb development. *Science signaling* **6**, pe14. ISSN 1937-9145.
- Miura, T., Shiota, K., Morriss-Kay, G. and Maini, P. K.** (2006). Mixed-mode pattern in Doublefoot mutant mouse limb—Turing reaction-diffusion model on a growing domain during limb development. *Journal of theoretical biology* **240**, 562–73. ISSN 0022-5193.
- Miyazono, K., Kamiya, Y. and Morikawa, M.** (2010). Bone morphogenetic protein receptors and signal transduction. *Journal of biochemistry* **147**, 35–51. ISSN 1756-2651.
- Morishita, Y. and Iwasa, Y.** (2008a). Growth based morphogenesis of vertebrate limb bud. *Bulletin of mathematical biology* **70**, 1957–78. ISSN 1522-9602.
- Morishita, Y. and Iwasa, Y.** (2008b). Optimal placement of multiple morphogen sources. *Physical Review E* **77**, 1–9. ISSN 1539-3755.
- Morishita, Y. and Iwasa, Y.** (2009). Estimating the spatiotemporal pattern of volumetric growth rate from fate maps in chick limb development. *Developmental Dynamics* **238**, 415–22. ISSN 1058-8388.
- Muller, P., Rogers, K., Jordan, B., Lee, J. S., Robson, D., Ramanathan, S. and Schier, A. F.** (2012). Differential Diffusivity of Nodal and Lefty underlies a reaction-diffusion Patterning System. *Science* **336**, 721–724.
- Müller, P., Rogers, K. W., Yu, S. R., Brand, M. and Schier, A. F.** (2013). Morphogen transport. *Development (Cambridge, England)* **140**, 1621–38. ISSN 1477-9129.

- Murone, M., Rosenthal, A. and de Sauvage, F. J.** (1999). Sonic hedgehog signaling by the patched-smoothed receptor complex. *Current Biology* **9**, 76–84. ISSN 0960-9822.
- Murray, J. D.** (2003). *Mathematical Biology II: Spatial Models and Biomedical Applications*. Springer-Verlag, New York.
- Nachtrab, G., Kikuchi, K., Tornini, V. a. and Poss, K. D.** (2013). Transcriptional components of anteroposterior positional information during zebrafish fin regeneration. *Development (Cambridge, England)* **140**, 3754–64. ISSN 1477-9129.
- Nahmad, M. and Stathopoulos, A.** (2009). Dynamic Interpretation of Hedgehog Signaling in the Drosophila Wing Disc. *PLoS biology* **4**, 273–7. ISSN 1933-6942.
- Newman, S. a. and Bhat, R.** (2007). Activator-inhibitor dynamics of vertebrate limb pattern formation. *Birth defects research. Part C, Embryo today : reviews* **81**, 305–19. ISSN 1542-9768.
- Newman, S. a. and Frisch, H. L.** (1979). Dynamics of skeletal pattern formation in developing chick limb. *Science (New York, N.Y.)* **205**, 662–8. ISSN 0036-8075.
- Nissim, S., Allard, P., Bandyopadhyay, A., Harfe, B. D. and Tabin, C. J.** (2007). Characterization of a novel ectodermal signaling center regulating Tbx2 and Shh in the vertebrate limb. *Developmental Biology* **304**, 9–21. ISSN 0012-1606.
- Nissim, S., Hasso, S. M., Fallon, J. F. and Tabin, C. J.** (2006). Regulation of Gremlin expression in the posterior limb bud. *Developmental Biology* **299**, 12–21. ISSN 0012-1606.
- Niswander, L., Tickle, C., Vogel, a., Booth, I. and Martin, G. R.** (1993). FGF-4 replaces the apical ectodermal ridge and directs outgrowth and patterning of the limb. *Cell* **75**, 579–87. ISSN 0092-8674.
- Noji, S., Nohno, T., Koyama, E., Muto, K., Ohyama, K., Aoki, Y., Tamura, K., Ohsugi, K., Ide, H., Taniguchi, S. and Saito, T.** (1991). Retinoic acid induces polarizing activity but is unlikely to be a morphogen in the chick limb bud. *Nature* **350**, 83–6.
- Ohuchi, H., Nakagawa, T., Yamamoto, a., Araga, a., Ohata, T., Ishimaru, Y., Yoshioka, H., Kuwana, T., Nohno, T., Yamasaki, M., Itoh, N. and Noji, S.** (1997). The mesenchymal factor, FGF10, initiates and maintains the outgrowth of the chick limb bud through interaction with FGF8, an apical ectodermal factor. *Development (Cambridge, England)* **124**, 2235–44. ISSN 0950-1991.
- Oster, G., Murray, J. and Maini, P. K.** (1985). A model for chondrogenic condensations in the developing limb: the role of extracellular matrix and cell tractions. *Journal of embryology and ...* **112**, 93–112.

- Oster, G. F., Murray, J. D. and Harris, a. K.** (1983). Mechanical aspects of mesenchymal morphogenesis. *Journal of embryology and experimental morphology* **78**, 83–125. ISSN 0022-0752.
- Pajni-Underwood, S., Wilson, C. P., Elder, C., Mishina, Y. and Lewandoski, M.** (2007). BMP signals control limb bud interdigital programmed cell death by regulating FGF signaling. *Development (Cambridge, England)* **134**, 2359–68. ISSN 0950-1991.
- Panman, L., Galli, A., Lagarde, N., Michos, O., Soete, G., Zúñiga, A. and Zeller, R.** (2006). Differential regulation of gene expression in the digit forming area of the mouse limb bud by SHH and gremlin 1/FGF-mediated epithelial-mesenchymal signalling. *Development (Cambridge, England)* **133**, 3419–28. ISSN 0950-1991.
- Park, H. L., Bai, C., Platt, K. A., Matisse, M. P., Beeghly, A., Hui, C.-C., Nakashima, M. and Joyner, A. L.** (2000). Mouse Gli1 mutants are viable but have defects in SHH signaling in combination with a Gli2 mutation. *Development (Cambridge, England)* **127**, 1593–605. ISSN 0950-1991.
- Parr, B. A. and McMahon, A. P.** (1995). Dorsalizing signal Wnt-7a required for normal polarity of DV and AP axes of mouse limb. *Nature* **374**.
- Pateder, D. B., Ferguson, C. M., Ionescu, A. M., Schwarz, E. M., Rosier, R. N., Puzas, J. E. and O’Keefe, R. J.** (2001). PTHrP expression in chick sternal chondrocytes is regulated by TGF-beta through Smad-mediated signaling. *Journal of cellular physiology* **188**, 343–51. ISSN 0021-9541.
- Pateder, D. B., Rosier, R. N., Schwarz, E. M., Reynolds, P. R., Puzas, J. E., D’Souza, M. and O’Keefe, R. J.** (2000). PTHrP expression in chondrocytes, regulation by TGF-beta, and interactions between epiphyseal and growth plate chondrocytes. *Experimental cell research* **256**, 555–62. ISSN 0014-4827.
- Peter, I. S. and Davidson, E. H.** (2011). Evolution of gene regulatory networks controlling body plan development. *Cell* **144**, 970–85. ISSN 1097-4172.
- Pizette, S. and Niswander, L.** (1999). BMPs negatively regulate structure and function of the limb apical ectodermal ridge. *Development (Cambridge, England)* **126**, 883–94. ISSN 0950-1991.
- Popławski, N. J., Swat, M., Gens, J. S. and Glazier, J. A.** (2007). Adhesion between cells, diffusion of growth factors, and elasticity of the AER produce the paddle shape of the chick limb. *Physica A* **373**, 521–532. ISSN 0378-4371.
- Probst, S., Kraemer, C., Demougin, P., Sheth, R., Martin, G. R., Shiratori, H., Hamada, H., Iber, D., Zeller, R. and Zúñiga, A.** (2011). SHH propagates distal limb bud development by enhancing CYP26B1-mediated retinoic acid clearance via AER-FGF signalling. *Development (Cambridge, England)* **138**, 1913–23. ISSN 1477-9129.

- Provot, S. and Schipani, E.** (2005). Molecular mechanisms of endochondral bone development. *Biochemical and biophysical research communications* **328**, 658–65. ISSN 0006-291X.
- Revest, J. M., Spencer-Dene, B., Kerr, K., De Moerlooze, L., Rosewell, I. and Dickson, C.** (2001). Fibroblast growth factor receptor 2-IIIb acts upstream of Shh and Fgf4 and is required for limb bud maintenance but not for the induction of Fgf8, Fgf10, Msx1, or Bmp4. *Developmental Biology* **231**, 47–62. ISSN 0012-1606.
- Riddle, R. D., Johnson, R. L., Laufer, E. and Tabin, C. J.** (1993). Sonic hedgehog mediates the polarizing activity of the ZPA. *Cell* **75**, 1401–16. ISSN 0092-8674.
- Roselló-Díez, A., Ros, M. A. and Torres, M.** (2011). Diffusible signals, not autonomous mechanisms, determine the main proximodistal limb subdivision. *Science (New York, N.Y.)* **332**, 1086–8. ISSN 1095-9203.
- Sanders, T. a., Llagostera, E. and Barna, M.** (2013). Specialized filopodia direct long-range transport of SHH during vertebrate tissue patterning. *Nature* , 0–6ISSN 1476-4687.
- Sanz-Ezquerro, J. J. and Tickle, C.** (2000). Autoregulation of Shh expression and Shh induction of cell death suggest a mechanism for modulating polarising activity during chick limb development. *Development (Cambridge, England)* **127**, 4811–23. ISSN 0950-1991.
- Sasaki, H., Nishizaki, Y., Hui, C.-C., Nakafuku, M. and Kondoh, H.** (1999). Regulation of Gli2 and Gli3 activities by an amino-terminal repression domain: implication of Gli2 and Gli3 as primary mediators of Shh signaling. *Development (Cambridge, England)* **126**, 3915–24. ISSN 0950-1991.
- Satoh, A. and Makanae, A.** (2014). Conservation of position-specific gene expression in axolotl limb skin. *Zoological science* **31**, 6–13. ISSN 0289-0003.
- Saunders, J. W.** (1948). The proximo-distal sequence of origin of the parts of the chick wing and the role of the ectoderm. *The Journal of experimental zoology* **282**, 628–68. ISSN 0022-104X.
- Saunders, J. W. and Gasseling, M. T.** (1968). Ectoderm-mesenchymal interactions in the origin of wing symmetry. In R. Fleischmajer and R. E. Billingham, eds., *Epithelial-mesenchymal interactions*. Williams and Wilkins, Baltimore, pages 78–97.
- Scherz, P. J., Harfe, B. D., McMahon, A. P. and Tabin, C. J.** (2004). The limb bud Shh-Fgf feedback loop is terminated by expansion of former ZPA cells. *Science (New York, N.Y.)* **305**, 396–9. ISSN 1095-9203.
- Schnakenberg, J.** (1979). Simple chemical reaction systems with limit cycle behaviour. *Journal of theoretical biology* **81**, 389–400. ISSN 0022-5193.

- Sekine, K., Ohuchi, H., Fujiwara, M., Yamasaki, M., Yoshizawa, T., Sato, T., Yagishita, N., Matsui, D., Koga, Y., Itoh, N. and Kato, S.** (1999). Fgf10 is essential for limb and lung formation. *Nature genetics* **21**, 138–41. ISSN 1061-4036.
- Selever, J., Liu, W., Lu, M.-F., Behringer, R. R. and Martin, J. F.** (2004). Bmp4 in limb bud mesoderm regulates digit pattern by controlling AER development. *Developmental Biology* **276**, 268–79. ISSN 0012-1606.
- Sheth, R., Gregoire, D., Dumouchel, A., Scotti, M., Pham, J. M. T., Nemeč, S., Bastida, M. F., Ros, M. A. and Kmita, M.** (2013). Decoupling the function of Hox and Shh in developing limb reveals multiple inputs of Hox genes on limb growth. *Development (Cambridge, England)* **140**, 2130–2138. ISSN 0950-1991.
- Sheth, R., Marcon, L., Bastida, M. F., Junco, M., Quintana, L., Dahn, R., Kmita, M., Sharpe, J. and Ros, M. A.** (2012). Hox Genes Regulate Digit Patterning by Controlling the Wavelength of a Turing-Type Mechanism. *Science* **338**, 1476–1480. ISSN 0036-8075.
- Sick, S., Reinker, S., Timmer, J. and Schlake, T.** (2006). WNT and DKK determine hair follicle spacing through a reaction-diffusion mechanism. *Science (New York, N.Y.)* **314**, 1447–50. ISSN 1095-9203.
- Spagnoli, A., O’Rear, L., Chandler, R. L., Granero-Molto, F., Mortlock, D. P., Gorska, A. E., Weis, J. a., Longobardi, L., Chytil, A., Shimer, K. and Moses, H. L.** (2007). TGF-beta signaling is essential for joint morphogenesis. *The Journal of cell biology* **177**, 1105–17. ISSN 0021-9525.
- St-Jacques, B., Hammerschmidt, M. and McMahon, A. P.** (1999). Indian hedgehog signaling regulates proliferation and differentiation of chondrocytes and is essential for bone formation. *Genes & development* **13**, 2072–86. ISSN 0890-9369.
- Summerbell, D.** (1983). The effect of local application of retinoic acid to the anterior margin of the developing chick limb. *Journal of embryology and experimental morphology* **78**, 269–89. ISSN 0022-0752.
- Tabin, C. J.** (1991). Retinoids, homeoboxes, and growth factors: toward molecular models for limb development. *Cell* **66**, 199–217.
- Tanaka, S. and Iber, D.** (2013). Inter-dependent tissue growth and Turing patterning in a model for long bone development. *Physical biology* **10**, 056009. ISSN 1478-3975.
- Tang, F., Lao, K. and Surani, M. A.** (2011). Development and applications of single-cell transcriptome analysis. *Nature methods* **8**, S6–11. ISSN 1548-7105.
- Tarchini, B., Duboule, D. and Kmita, M.** (2006). Regulatory constraints in the evolution of the tetrapod limb anterior-posterior polarity. *Nature* **443**, 985–8. ISSN 1476-4687.

- te Welscher, P., Fernandez-Teran, M., Ros, M. A. and Zeller, R.** (2002a). Mutual genetic antagonism involving GLI3 and dHAND prepatterns the vertebrate limb bud mesenchyme prior to SHH signaling. *Genes & Development* **16**, 421–6. ISSN 0890-9369.
- te Welscher, P., Zúñiga, A., Kuijper, S., Drenth, T., Goedemans, H. J., Meijlink, F. and Zeller, R.** (2002b). Progression of Vertebrate Limb Development Through SHH-Mediated Counteraction of GLI3. *Science* **298**, 827–830. ISSN 00368075.
- ten Berge, D., Brugmann, S. A., Helms, J. A. and Nusse, R.** (2008). Wnt and FGF signals interact to coordinate growth with cell fate specification during limb development. *Development (Cambridge, England)* **135**, 3247–57. ISSN 0950-1991.
- Thümmler, V. and Weddemann, A.** (2007). Computation of Space-Time Patterns via ALE Methods. *Excerpt from the Proceedings of the COMSOL Conference 2007 in Grenoble*, 1–7.
- Tickle, C.** (1981). The number of polarizing region cells required to specify additional digits in the developing chick wing. *Nature* **289**, 295–298.
- Tickle, C., Alberts, B., Wolpert, L. and Lee, J.** (1982). Local application of retinoic acid to the limb bud mimics the action of the polarizing region. *Nature* **296**, 564–6.
- Tickle, C., Shellswell, G., Crawley, A. and Wolpert, L.** (1976). Positional signalling by mouse limb polarising region in the chick wing bud. *Nature* **259**, 396–7.
- Todt, W. L. and Fallon, J. F.** (1987). Posterior apical ectodermal ridge removal in the chick wing bud triggers a series of events resulting in defective anterior pattern formation. *Development (Cambridge, England)* **101**, 501–15. ISSN 0950-1991.
- Towers, M. and Tickle, C.** (2009). Growing models of vertebrate limb development. *Development (Cambridge, England)* **136**, 179–90. ISSN 0950-1991.
- Turing, A. M.** (1952). The Chemical Basis of Morphogenesis. *Philosophical Transactions of the Royal Society B: Biological Sciences* **237**, 37–72. ISSN 0962-8436.
- Turner, N. and Grose, R.** (2010). Fibroblast growth factor signalling: from development to cancer. *Nature reviews. Cancer* **10**, 116–29. ISSN 1474-1768.
- Umulis, D. M., Shimmi, O., O’Connor, M. B. and Othmer, H. G.** (2010). Organism-scale modeling of early Drosophila patterning via bone morphogenetic proteins. *Developmental cell* **18**, 260–74. ISSN 1878-1551.
- van de Werken, H., Landan, G., Holwerda, S. J. B., Hoichman, M., Klous, P., Chachik, R., Splinter, E., Valdes-Quezada, C., Öz, Y., Bouwman, B. A. M., Verstegen, M. J. A. M., de Wit, E., Tanay, A. and de Laat, W.**

- (2012). Robust 4C-seq data analysis to screen for regulatory DNA interactions. *Nature methods* **9**, 969–72.
- van Donkelaar, C. C. and Huiskes, R.** (2007). The PTHrP-Ihh feedback loop in the embryonic growth plate allows PTHrP to control hypertrophy and Ihh to regulate proliferation. *Biomechanics and modeling in mechanobiology* **6**, 55–62. ISSN 1617-7959.
- Verheyden, J. M., Lewandoski, M., Deng, C., Harfe, B. D. and Sun, X.** (2005). Conditional inactivation of *Fgfr1* in mouse defines its role in limb bud establishment, outgrowth and digit patterning. *Development (Cambridge, England)* **132**, 4235–45. ISSN 0950-1991.
- Verheyden, J. M. and Sun, X.** (2008). An Fgf/Gremlin inhibitory feedback loop triggers termination of limb bud outgrowth. *Nature* **454**, 638–41. ISSN 1476-4687.
- Vokes, S. a., Ji, H., McCuine, S., Tenzen, T., Giles, S., Zhong, S., Longabaugh, W. J. R., Davidson, E. H., Wong, W. H. and McMahon, A. P.** (2007). Genomic characterization of Gli-activator targets in sonic hedgehog-mediated neural patterning. *Development (Cambridge, England)* **134**, 1977–89. ISSN 0950-1991.
- Vokes, S. a., Ji, H., Wong, W. H. and McMahon, A. P.** (2008). A genome-scale analysis of the cis-regulatory circuitry underlying sonic hedgehog-mediated patterning of the mammalian limb. *Genes & Development* **22**, 2651–63. ISSN 0890-9369.
- Vortkamp, A., Lee, K., Lanske, B., Segre, G. V., Kronenberg, H. M. and Tabin, C. J.** (1996). Regulation of Rate of Cartilage Differentiation by Indian Hedgehog and PTH-Related Protein. *Science* **273**, 613–622.
- Wakefield, L. M. and Hill, C. S.** (2013). Beyond TGF β : roles of other TGF β superfamily members in cancer. *Nature reviews. Cancer* **13**, 328–41. ISSN 1474-1768.
- Wang, B., Fallon, J. F. and Beachy, P. A.** (2000). Hedgehog-regulated processing of Gli3 produces an anterior/posterior repressor gradient in the developing vertebrate limb. *Cell* **100**, 423–434.
- Wang, C.-K. L., Omi, M., Ferrari, D., Cheng, H.-C., Lizarraga, G., Chin, H.-J., Upholt, W. B., Dealy, C. N. and Kosher, R. A.** (2004). Function of BMPs in the apical ectoderm of the developing mouse limb. *Developmental Biology* **269**, 109–22. ISSN 0012-1606.
- Wartlick, O., Mumcu, P., Kicheva, A., Bittig, T., Seum, C., Julicher, F. and González-Gaitán, M.** (2011). Dynamics of Dpp Signaling and Proliferation Control. *Science* **331**, 1154–1159. ISSN 0036-8075.

- Weir, E. C., Philbrick, W. M., Amling, M., Neff, L. A., Baron, R. and Broadus, A. E.** (1996). Targeted overexpression of parathyroid hormone-related peptide in chondrocytes causes chondrodysplasia and delayed endochondral bone formation. *Proceedings of the National Academy of Sciences of the United States of America* **93**, 10240–5. ISSN 0027-8424.
- Wen, X., Lai, C. K., Evangelista, M., Hongo, J.-A., de Sauvage, F. J. and Scales, S. J.** (2010). Kinetics of hedgehog-dependent full-length Gli3 accumulation in primary cilia and subsequent degradation. *Molecular and cellular biology* **30**, 1910–22. ISSN 1098-5549.
- Wolpert, L.** (1969). Positional information and the spatial pattern of cellular differentiation. *Journal of theoretical biology* **25**, 1–47. ISSN 0022-5193.
- Woltering, J., Noordermeer, D., Leleu, M. and Duboule, D.** (2014). Conservation and Divergence of Regulatory Strategies at Hox Loci and the Origin of Tetrapod Digits. *PLoS Biology* **12**, e1001773. ISSN 1545-7885.
- Wuelling, M. and Vortkamp, A.** (2010). Transcriptional networks controlling chondrocyte proliferation and differentiation during endochondral ossification. *Pediatric nephrology (Berlin, Germany)* **25**, 625–31. ISSN 1432-198X.
- Wuelling, M. and Vortkamp, A.** (2011). Chondrocyte Proliferation and Differentiation. In C. Camacho-Hübner, O. Nilsson and L. Sävendahl, eds., *Cartilage and Bone Development and Its Disorders*. Endocr Dev. Basel, pages 1–11.
- Wyngaarden, L. A., Vogeli, K. M., Ciruna, B. G., Wells, M., Hadjantonakis, A.-K. and Hopyan, S.** (2010). Oriented cell motility and division underlie early limb bud morphogenesis. *Development (Cambridge, England)* **137**, 2551–8. ISSN 1477-9129.
- Yang, Y., Drossopoulou, G., Chuang, P. T., Duprez, D. M., Marti, E., Bumcrot, D., Vargesson, N., Clarke, J., Niswander, L., McMahon, A. P. and Tickle, C.** (1997). Relationship between dose, distance and time in Sonic Hedgehog-mediated regulation of anteroposterior polarity in the chick limb. *Development (Cambridge, England)* **124**, 4393–404. ISSN 0950-1991.
- Yang, Y. and Niswander, L.** (1995). Interaction between the signaling molecules WNT7a and SHH during vertebrate limb development: dorsal signals regulate anteroposterior patterning. *Cell* **80**, 939–47. ISSN 0092-8674.
- Yu, S. R., Burkhardt, M., Nowak, M., Ries, J., Petrásek, Z., Scholpp, S., Schwille, P. and Brand, M.** (2009). Fgf8 morphogen gradient forms by a source-sink mechanism with freely diffusing molecules. *Nature* **461**, 533–6. ISSN 1476-4687.
- Zákány, J., Kmita, M. and Duboule, D.** (2004). A dual role for Hox genes in limb anterior-posterior asymmetry. *Science (New York, N.Y.)* **304**, 1669–72. ISSN 1095-9203.

- Zeller, R., López-Ríos, J. and Zúñiga, A.** (2009). Vertebrate limb bud development: moving towards integrative analysis of organogenesis. *Nature reviews. Genetics* **10**, 845–58. ISSN 1471-0064.
- Zhang, D., Schwarz, E., Rosier, R. N., Zuscik, M. J., Puzas, J. E. and O’Keefe, R. J.** (2003). ALK2 Functions as a BMP Type I Receptor and Induces Indian Hedgehog in Chondrocytes During Skeletal Development. *Journal of Bone and Mineral Research* **18**, 1593–1604.
- Zhang, Y.-t., Alber, M. S. and Newman, S. A.** (2013). Mathematical modeling of vertebrate limb development. *MATHEMATICAL BIOSCIENCES* ISSN 0025-5564.
- Zhang, Z., Sui, P., Dong, A., Hassell, J., Cserjesi, P., Chen, Y.-T., Behringer, R. R. and Sun, X.** (2010). Preaxial polydactyly: interactions among ETV, TWIST1 and HAND2 control anterior-posterior patterning of the limb. *Development (Cambridge, England)* **137**, 3417–26. ISSN 1477-9129.
- Zhang, Z., Verheyden, J. M., Hassell, J. A. and Sun, X.** (2009). FGF-Regulated Etv Genes Are Essential for Repressing Shh Expression in Mouse Limb Buds. *Developmental Cell* **16**, 607–613. ISSN 15345807.
- Zhao, X., Sirbu, I. O., Mic, F. a., Molotkova, N., Molotkov, A., Kumar, S. and Duester, G.** (2009). Retinoic acid promotes limb induction through effects on body axis extension but is unnecessary for limb patterning. *Current Biology* **19**, 1050–7. ISSN 1879-0445.
- Zhu, J., Nakamura, E., Nguyen, M.-T., Bao, X., Akiyama, H. and Mackem, S.** (2008). Uncoupling Sonic hedgehog control of pattern and expansion of the developing limb bud. *Developmental Cell* **14**, 624–32. ISSN 1878-1551.
- Zhu, J., Zhang, Y.-T., Alber, M. S. and Newman, S. A.** (2010). Bare bones pattern formation: a core regulatory network in varying geometries reproduces major features of vertebrate limb development and evolution. *PloS one* **5**, e10892. ISSN 1932-6203.
- Zimmerman, L. B., De Jesús-Escobar, J. M. and Harland, R. M.** (1996). The Spemann organizer signal noggin binds and inactivates bone morphogenetic protein 4. *Cell* **86**, 599–606. ISSN 0092-8674.
- Zimmermann, R. and Görtz, S.** (2012). Improved Extrapolation of Steady Turbulent Aerodynamics using a Non-Linear POD-Based Reduced Order Model ISSN 1545-8636.
- Zou, H., Wieser, R., Massague, J. and Niswander, L.** (1997). Distinct roles of type I bone morphogenetic protein receptors in the formation and differentiation of cartilage. *Genes & Development* **11**, 2191–2203. ISSN 0890-9369.
- Zúñiga, A., Haramis, A.-P. G., McMahon, A. P. and Zeller, R.** (1999). Signal relay by BMP antagonism controls the SHH/FGF4 feedback loop in vertebrate limb buds. *Nature* **401**, 598–602.

Zúñiga, A., Laurent, F., López-Ríos, J., Klasen, C., Matt, N. and Zeller, R. (2012). Conserved cis-regulatory regions in a large genomic landscape control SHH and BMP-regulated Gremlin1 expression in mouse limb buds. *BMC developmental biology* **12**, 23. ISSN 1471-213X.

Zúñiga, A., Michos, O., Spitz, F., Haramis, A.-P. G., Panman, L., Galli, A., Vintersten, K., Klasen, C., Mansfield, W., Kuc, S., Duboule, D., Dono, R. and Zeller, R. (2004). Mouse limb deformity mutations disrupt a global control region within the large regulatory landscape required for Gremlin expression. *Genes & Development* **18**, 1553–64. ISSN 0890-9369.

Curriculum Vitae

Personal Information

Name Philipp Daniel Germann
Contact philipp.germann@gmail.com

Education

since 2010 PhD Candidate supervised by Dagmar Iber, Department of Biosystems Science and Engineering, ETH Zurich.
2008 - 2010 M. Sc. Physics, University of Bern. With special qualification in theoretical physics. Thesis on *The Unruh Effect* supervised by Matthias Blau.
2005 - 2009 B. Sc. Physics, University of Bern. With special qualification in Astronomy, minor in Mathematics. Thesis on *Universality in Ising Models* supervised by Peter Hasenfratz.

Publications

Articles **Germann, P. and Iber, D.** A Data-based Computational Model for the Epithelial-Mesenchymal SHH/BMP/GREM1/FGF Feedback Loop in Limb Bud Development. *Submitted*.

López-Ríos, J., Duchesne, A., Speziale, D., Andrey, G., Peterson, K. A., Germann, P., Erkan, Ü., Liu, J., Barbey, S., Gallard, Y., Floriot, S., Müller-Gerbl, M., Courtney, A. D., Klopp, C., Rodriguez, S., Ivanek, R., Beisel, C., Wicking, C., Iber, D., Robert, B., McMahon, A. P., Duboule, D. and Zeller, R. (2014). Attenuated sensing of SHH by Ptch1 underlies adaptive evolution of bovine limbs. *Nature* **511**, 46-51. ISSN 0028-0836.

Badugu, A., Kraemer, C., Germann, P., Menshykau, D. and Iber, D. (2012). Digit patterning during limb development as a result of the BMP-receptor interaction. *Scientific reports* **2**, 991. ISSN 2045-2322.

Review **Iber, D. and Germann, P.** (2014). How do digits emerge? – Mathematical Models of Limb Development. *Birth Defects Research. Part C, Embryo Today: Reviews* **102**, 1-12. ISSN 1542-9768.

- Book chapter **Iber, D., Tanaka, S., Fried, P., Germann, P. and Menshykau, D.** (2013). Simulating Tissue Morphogenesis and Signaling. *In C. M. Nelson, ed., Tissue Morphogenesis (Methods in Molecular Biology series), number 1. New York: Springer.*
- Proceedings **Menshykau, D., Adivarahan, S., Germann, P., Lermuzeaux, L. and Iber, D.** (2013). Simulating Organogenesis in COMSOL: Parameter Optimization for PDE-based models. *Excerpt from the Proceedings of the 2013 COMSOL Conference in Rotterdam*, 1-6.
- Germann, P., Menshykau, D., Tanaka, S. and Iber, D.** (2011). Simulating Organogenesis in COMSOL. *Excerpt from the Proceedings of the COMSOL Conference 2011 in Stuttgart*, 1-5.